SEMICONDUCTOR-SENSITIZED MESOSCOPIC SOLAR CELLS: FROM TiO_2 to SnO_2

MD. ANOWER HOSSAIN

(*B.Sc.*, *BUET*)

A THESIS SUBMITTED

FOR THE DEGREE OF DOCTOR OF PHILOSOPHY

DEPARTMENT OF MATERIALS SCIENCE & ENGINEERING

NATIONAL UNIVERSITY OF SINGAPORE

2012

Declaration

I hereby declare that the thesis is my original work and it has been written by me in its entirety. I have duly acknowledged all the sources of information, which have been used in the thesis.

This thesis has not been submitted for any degree in any university previously.

_____

Md. Anower Hossain

10 August 2012

Acknowledgements

I would like to take this opportunity to express my sincere appreciation to the people in National University of Singapore. First and foremost, I would like to express my deepest gratitude and respect to my supervisor, Asst. Prof. Wang Qing, for his continued encouragements, insightful remarks and supports throughout my candidature which have been invaluable. In particular, I would like to thank him for providing me an opportunity to work in his group under his guidance.

I also wish to thank all the group members of Asst. Prof. Wang Qing, for their help, support, and cheerful face! My especial thank goes to Dr. James Robert Jennings and Dr. Yang Guangwu for their valuable suggestions and scientific discussions. I sincerely thank the rest of the group members, Dr. Sun Lidong, Dr. Pan Jia Hong, Dr. Wang Xingzhu, Ms. Zhen Yu Koh, Ms. Liu Yeru, Mr. Li Feng, Mr. Huang Qizhao, Mr Shen Chao and Ms. Fatemeh Safari-Alamuti for being supportive in past years.

I would like to acknowledge the financial support from National University of Singapore for the research scholarship and state of the art research facilities. I am also grateful to all the technical staffs of the Department of Materials Science and Engineering for theirs helping hands when I was in need.

I am totally indebted to my parents, Md. Ashraf Ali and Hasina Khatun, for their unconditional love and endless support throughout my studies. Finally, I would like to extend my gratitude to my beloved wife, Urmi, for her prayer and inspiration.

Table of Contents

Summary

Semiconductor-sensitized wide band gap metal oxides (*i.e.* TiO_2, SnO_2) solar cells employing CdSe as light absorber demonstrate superior photovoltaic performance to the best-performed cascaded CdS/CdSe cells with practically identical optical density. In this thesis, an investigation on band alignment of CdS/CdSe-sensitized electrodes unambiguously reveals that the CdS significantly promotes the growth of CdSe and hence increases light harvesting, but this impedes the injection of electrons from CdSe to metal oxides and accelerates charge recombination at the metal oxide/sensitizer interface. As a result, unprecedented power conversion efficiency was achieved with CdSe-sensitized solar cells when light absorption is identical to that of CdS/CdSe cells, making the CdS buffer layer redundant.

The optical band gap of semiconductor sensitizer and the alignment of its bands with the underlying metal oxide are critical for efficient light harvesting and charge separation in SSCs. In practice, these two requirements are however not always fulfilled concomitantly in SSCs as utilization of quantum sized CdSe causes great losses in the harvesting of long wavelength photons. Therefore, CdS_xSe_{1-x}-sensitized electrodes, which have tunable band gap energies between those of CdSe and CdS without reducing the dimension, were synthesized and explored in SSCs. The findings provide an alternative and viable approach for optimizing the energetics of semiconductor sensitizers for efficient charge separation, while also maintaining good light harvesting.

Metal oxide semiconductors with lower lying conduction band minimum and superior carrier mobility are beneficial for efficient charge separation and collection in SSCs. Therefore, mesoscopic SnO_2 was investigated as an alternative photoanode

to the commonly used TiO_2 and examined comprehensively in CdSe, and CdS/CdSe-sensitized solar cells, and was found to be superior, exhibiting an unprecedented short-circuits photocurrent density and nearly unity incident photon-to-current conversion efficiency because of long electron diffusion lengths and superior charge separation yield with much reduced charge recombination kinetics compared with TiO_2-based SSCs.

Mesoscopic SnO_2 was investigated comprehensively for narrow band gap PbS-sensitized liquid junction solar cells. To exploit the capability of PbS in an optimized structure, cascaded and alternate PbS/CdS layers deposited by SILAR method were systematically scrutinized. It was observed that the surface of SnO_2 has greater affinity for the growth of PbS compared with TiO_2, giving rise to much enhanced light absorption. Under an optimized condition, a panchromatic sensitizer, cascaded PbS/CdS-sensitized SnO_2 cells exhibited an unprecedented photocurrent density with pronounced infrared light harvesting extending beyond 1100 nm because of viability of the usage of larger PbS quantum dots; thus higher power conversion efficiency was observed than that of TiO_2-based cells.

Tin oxide ($Sn_6O_4(OH)_4$, SnO, SnO_2) nanostructures with tunable shape and size were synthesized by a post-treatment of $Sn_6O_4(OH)_4$ nanoparticles obtained from electrochemical anodization of tin foil. By controlling the water content in anodizing electrolyte during anodization of tin foil and the concentration of as-prepared primary $Sn_6O_4(OH)_4$ nanoparticles in the post-treatment step, solid/hollow spheres, and hollow cubes were assembled by Ostwald ripening and oriented attachment, respectively. Using hydrophobic ethylene glycol in the post-treatment step, octahedrons and polyhedrons were also synthesized. After annealing the as-prepared solid spheres, the mesoporous SnO_2 nanoparticles was then used as photoanode material in SSCs.

List of Tables

List of Figures

List of Symbols and Abbreviations

SSCs	Semiconductor-sensitized solar cells
DSCs	Dye-sensitized solar cells
TCO	Transparent conducting oxide
FTO	Fluorine doped tin oxide
QDs	Quantum dots
CBD	Chemical bath deposition
SILAR	Successive ionic layer adsorption and reaction
SEM	Scanning electron microscopy
TEM	Transmission electron microscopy
HRTEM	High-resolution transmission electron microscopy
XRD	X-ray diffraction
EDS	Energy-dispersive X-ray spectroscopy
FTIR	Fourier transforms infrared spectroscopy
PL	Photoluminescence
IPCE	Incident photon-to-current conversion efficiency
$\eta_{\mathrm{lh}}(\lambda)$	Light harvesting efficiency
$\eta_{\mathrm{inj}}(\lambda)$	Carrier injection efficiency
$\eta_{\mathrm{sep}}(\lambda)$	Charge separation efficiency
$\eta_{\mathrm{col}}(\lambda)$	Charge collection efficiency
$\eta_{\mathrm{reg}}(\lambda)$	Sensitizer regeneration efficiency
E_g	Band gap energy of semiconductor
CB	Conduction band
VB	Valence band

E_{Fn}	Electron quasi-Fermi level
I_0	Incident light intensity
I	Transmitted light intensity
$\alpha\ (\lambda)$	Light absorption coefficient
λ	Wavelength of light
l	Film thickness
ν	Frequency of light
h	Planks constant
k_B	Boltzman constant
j_{sc}	Short circuit photocurrent density
J_0	Diode saturation current density
V_{oc}	Open circuit photo-voltage
MEG	Multiple exciton generation
$b_s(\lambda)$	Solar photon flux
P_{in}	Incident irradiance, power input
P_{out}	Power output
P_{max}	Maximum power point
j_m	Current density corresponding to maximum power point
V_m	Voltage corresponding to maximum power point
ff	Fill factor
IS	Impedance spectroscopy
R_s	Series resistance
R_{sh}	Shunt resistance
m	Diode ideality factor
C_{sub}	Substrate capacitance

R_{t}	Charge transport resistance
r_{t}	Distributed electron transport resistance
R_{ct}	Charge transfer resistance
r_{ct}	Distributed charge transfer resistance
C_{μ}	Chemical capacitance of oxide layer
c_{μ}	Distributed capacitance of oxide layer
Z_{d}	Warburg impedance
R_{Pt}	Resistance of platinized cathode
C_{Pt}	Capacitance of cathode
L_{n}	Effective electron diffusion length

List of Publications

1. ***Md. Anower Hossain****; Guangwu Yang; Manoj Parameswaran; James Robert Jennings; Qing Wang*, Mesoporous SnO_2 spheres synthesized by electrochemical anodization and their application in CdSe-sensitized solar cells. *J. Phys. Chem. C* **2010,** *114*, 21878-21884. (Top 20 most read articles in JPCC in December, 2010).

2. ***Md. Anower Hossain****; James Robert Jennings; Zhen Yu Koh; Qing Wang*, Carrier generation and collection in CdS/CdSe-sensitized SnO_2 solar cells exhibiting unprecedented photocurrent densities. *ACS Nano* **2011,** *5*, 3172-3181.

3. ***Md. Anower Hossain****; James Robert Jennings; Nripan Mathews; Qing Wang*, Band engineered ternary solid solution CdS_xSe_{1-x}-sensitized mesoscopic TiO_2 solar cells. *Phys. Chem. Chem. Phys.*, **2012,** *14*, 7154-7161**.**

4. ***Md. Anower Hossain****; Zhen Yu Koh; Qing Wang*, PbS/CdS-sensitized mesoscopic SnO_2 solar cells for enhanced infrared light harnessing. *Phys. Chem. Chem. Phys.*, **2012,** *14*, 7367-7374**.**

5. ***Md. Anower Hossain****; James Robert Jennings; Chao Shen; Jia Hong Pan; Zhen Yu Koh; Nripan Mathews; Qing Wang*, CdSe-sensitized mesoscopic TiO_2 solar cells exhibiting > 5% efficiency: redundancy of CdS buffer layer. *J. Mater. Chem.* **2012,** *22*, 16235-16242 (Hot article, Inside front cover).

6. *Xuan-Hao Chan; James Robert Jennings;* ***Md. Anower Hossain****; Zhen Yu Koh; Qing Wang*, Characteristics of p-NiO thin films prepared by spray pyrolysis and their application in CdS-sensitized photocathodes. *J. Electrochem. Soc.* **2011,** *158*, H733-H740.

7. *Lidong Sun; Yao Huang;* ***Md. Anower Hossain****; Kangle Li; Stefan Adams; Qing Wang,* Fabrication of TiO_2/CuSCN bulk heterojunctions by profile-controlled electrodeposition for solid-state dye-sensitized solar cells. *J. Electrochem. Soc.* **2012,** *159*, D323-D327**.**

8. *Fatemeh Safari-Alamuti; James Robert Jennings;* ***Md. Anower Hossain****; Lanry Yung Lin Yue; Qing Wang*, Conformal growth of nanocrystalline CdX (X = S, Se) on mesoscopic NiO and their photoelectrochemical properties (*Phys. Chem. Chem. Phys.*, **2013**).

9. ***Md. Anower Hossain****; Jia Hong Pan; Qing Wang,* Tailoring the Morphology of hollow tin oxide nanostructures by an electrochemical anodization and a facile post-treatment method. (Article in preparation, 2012)

List of Conferences

1. ***Md. Anower Hossain****; Qing Wang*, Synthesis of SnO_2 nanostructures by electrochemical anodization. ICAM workshop at Institute of Physics, Chinese Academy of Sciences, Beijing, China. May 31-June 3, 2010 (Poster).

2. ***Md. Anower Hossain****; Qing Wang*, Preparation of nanostructured SnO_2 by electrochemical anodization and its application in lithium ion batteries and quantum dot solar cells. 5th Asian Conference on Electrochemical Power Sources (ACEPS-5), National University of Singapore, 7 engineering drive 1, Singapore 117574, 17-20 September, 2010 (Oral).

3. ***Md. Anower Hossain****; James Robert Jennings; Qing Wang*, CdS/CdSe-sensitized SnO_2 solar cells with superior incident photon to collected electron conversion efficiency. Materials Research Society, Spring meeting 2011, San Francisco, California, April 25 -29, 2011 (Poster).

4. ***Md. Anower Hossain****; James Robert Jennings; Qing Wang*, Carrier generation and collection in quantum dot-sensitized solar cells employing different oxides. International Conference on Materials for Advanced Technologies (ICMAT 2011), June 26 to July 1 2011 (Poster).

5. ***Md. Anower Hossain****; Qing Wang*, CdSSe and CdPbS solid solutions made by SILAR deposition and their application in semiconductor-sensitized solar cells. 3rd Hybrid and Organic Photovoltaics Conference (HOPV 2011), 15 – 18 May, 2011, Valencia, Spain (Poster).

1 Introduction

1.1 Why renewable energy?

Energy consumption is increasing exponentially due to population explosion and fast-growing economy in the developing countries. In 2005 the total power consumption of the world was estimated to be 15 terawatt (TW), which would be doubled in 2050 and tripled at the end of the century (> 45 TW).[1] To meet this increasing demand of energy, the current fossil fuel-based power plant is inadequate, as the reserves of fossil fuels (coal, oil, gas *etc.*) are depleting rapidly with time. In addition, their continued use produces greenhouse gases (~34 billion tons of CO_2 per year) causing irreversible changes to the earth's climate, which may ultimately have a catastrophic impact on life on earth. Although fossil fuels seem relatively inexpensive, they bring environmental issues like the (BP) gulf of Mexico oil spill in 2010 in the USA, which cost billions of dollars and severe impact to the environment. Another controversial power source, the nuclear power plant, was also criticized more than ever after partial melt down of the nuclear power plants at Fukushima in Japan in 2011.

The recent energy outlook 2030 by British Petroleum (BP) suggests that the energy shares of oil is going to be down from 39% to 27%, and the energy shares of renewable energy sources is going to be up from ~2% to ~7% by 2030.[2] Therefore, a new source of energy has become indispensable for the economic balance in the world while the usage of fossil fuels is reduced. Fortunately, the sun provides approximately 120,000 TW of irradiation on earth, which is orders of magnitude

higher than our current energy consumption. Therefore, it is the most abundant and the cleanest energy one can ever find. As a result, a lot of effort is being invested in harvesting energy from the sun as a complement to depleting fossil fuels and to mitigate the rising environmental issues.

Among various means of solar energy harvesting and conversion, photovoltaic cells directly convert sunlight into electricity and require almost no maintenance over a long period of time due to the absence of moving parts. With silicon-based *p-n* junction solar cells as an example, the sub-module efficiency has attained ~25% when crystalline silicon wafer is used as the light harvesting material.[3] However, the expensive technology used to process crystalline silicon is an inherent problem despite the fact that the manufacturing cost has been dramatically reduced in recent years. Moreover, the theoretical limit of single junction solar cells was calculated to be ~33% under AM 1.5 1 Sun illumination using an optimum band gap of 1.4 eV, known as the Shockley–Queisser limit.[4,5] Today, the most efficient solar cells are based on crystalline GaAs in a multi-junction tandem structure with concentrator systems which is economically viable only for space applications.[6] Therefore, a cheaper technology is desired for its widespread application.

To reduce the production cost, thin film technology has emerged by utilizing materials with superior light absorption, for instance the direct band gap semiconductors cadmium telluride (CdTe) or copper indium (gallium) diselenide ($CuIn_x(Ga)_{1-x}Se_2$, CIS or CIGS) are used for light harvesting. These materials are known to have very high extinction coefficients than that of crystalline silicon, implying that only a few microns (~2 μm) thick light absorber layers are needed to harvest the same amount of light that is harvested by a ~200 μm thick silicon layer in

silicon solar cells. The CdTe cell has shown an efficiency of 16.7 ± 0.5% in lab devices and a commercialized module efficiency of 14.4%, which is believed to be the cheapest solar cells so far because of a one-year payback period. However, the recycling of toxic cadmium initiated by the manufacturer, limited supply of tellurium and recent increasing demand for use in solar cells may affect the long term sustainability of the CdTe-based solar industry.[7] In addition, despite the prominent efficiency of 19.6 ± 0.6% of CIGS-based solar cell, the limited supply of gallium and indium appears as an obstruction to the ultimate manufacturing cost of CIGS thin film.[3]

Hence, new types of solar cells based on cheaper materials and technology than those used in the thin film technology have become crucial for widespread use. Excitonic solar cells such as organic solar cells, sensitized mesoscopic solar cells, *etc.*, which emerged in the last decade and have received much attention in these days, provide great promise to address the above issues. In addition, several concepts such as multi-junction tandem solar cells, intermediate band gap cells, hot carrier cells and spectrum up-/down-conversion have been proposed and actively developed.[8,9] Among these, the dye-sensitized solar cell (DSC) is one of the most promising photovoltaic technologies which has recently received much attention because of their ease of low cost fabrication compared with silicon and other thin film technologies.[10] With the continuous research efforts, the current power conversion efficiency of DSC has reached 12.3% after the pioneering work of Michael Grätzel and Brian O'Regan in 1991.[10,11]

While the DSC has attracted considerable interest, an alternative approach to further enhance light harvesting and device stability is the semiconductor-sensitized

solar cell (SSC), in which a semiconductor light absorber is used in the place of the molecular sensitizing dye. Because of the superior optical properties of semiconductor sensitizers over their molecular counterpart and the facile fabrication method compared to the dye-sensitized electrodes, the power conversion efficiency of SSCs has grown rapidly in the past few years and recently >5% efficiency has been attained.[12-14] In addition, with the demonstration of multiple exciton generation in PbS-sensitized TiO_2 solar cells,[15,16] sensitized mesoscopic solar cells using narrow band gap quantum dots (QDs) provide another new opportunity for achieving highly efficient solar energy conversion, which leads to the third generation photovoltaic devices. In this study, several semiconductor light absorbers such as CdS, CdSe, PbS *etc.* were employed to sensitize SnO_2 — an intriguing wide band gap nanocrystalline photoanode and comparisons were made with that of the widely used TiO_2.

1.2 Semiconductor-sensitized solar cells

The working principle of semiconductor-sensitized solar cells (SSCs) is analogous to DSCs with the generation of charge carriers being fundamentally different from that in *p*-*n* junction solar cells. The charge carriers in SSCs are bound electron-hole pairs called excitons, rather than free charge carriers in *p*-*n* junction solar cells which are generated immediately upon light absorption as the exciton binding energy is much less than the thermal energy at room temperature. These excitons need to be dissociated before the free electrons and holes are separated and collected at the contact. In a typical SSC one of the key components is the sensitized photoanode, consisting of a wide band gap *n*-type semiconducting nanocrystalline metal oxide layers such as TiO_2, SnO_2 with large area (hundreds of folds larger than their geometric area) deposited on transparent conducting oxide (TCO). Layers of

semiconductor sensitizers, such as CdS, CdSe, CdS_xSe_{1-x}, and PbS QDs are deposited on the large surface area mesoporous metal oxide, allowing sufficient loading of sensitizer to ensure efficient harvesting of light. The TCO allows light to enter into the cells and also makes a contact to the nanocrystalline metal oxide, which collects charge carriers to the external circuit (Fig. 1.1).

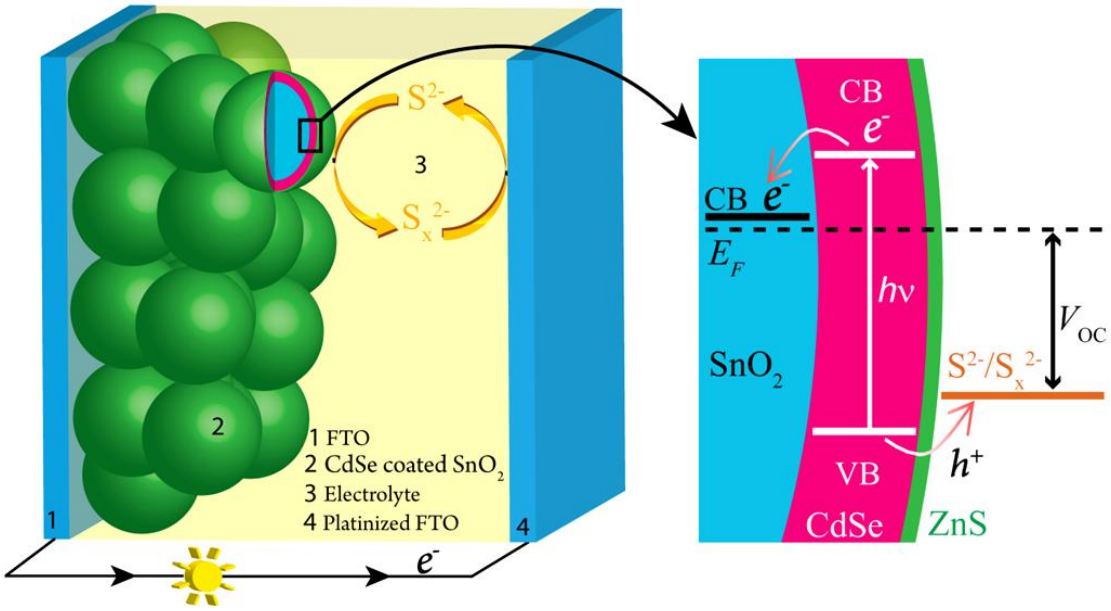

Figure 1. 1 A schematic diagram presenting the working principle of a CdSe-sensitized mesoscopic SnO_2 solar cell.

In order to fabricate a solar cell, the photoanode is sandwiched with a counter electrode (*i.e.* Pt, Cu_2S cathodes, *etc.*) by a polymer spacer, which is then filled with redox electrolyte (*i.e.* aqueous solution of polysulfide) before the cell is sealed. Upon illumination, the sensitizer gets excited and generates excitons at the sensitizer/SnO_2 interface with electron residing in the conduction band (CB) and holes in the valence band (VB) of sensitizers. Following excitation, electrons injection takes place subsequently from the excited states of semiconductor sensitizers into the vacant electronic states in the CB of metal oxide due to its relatively lower energy levels as

shown in Figure 1.1.[17] The injected electrons then transport through the metal oxide nanoparticles network to the collecting electrode by a diffusion process. The oxidized semiconductor is reduced back to the original state by the electron donor species (*e.g.* S^{2-}) in the electrolyte, which in turn are oxidized (*e.g.* polysulfide S_x^{2-}). If both electrodes are connected externally, the S_x^{2-} species are then reduced to S^{2-} by accepting electrons from the counter electrode. Thus it completes the circuit and as a whole, it operates as a regenerative photovoltaic energy conversion device.

So far, several wide band gap metal oxides such as TiO_2, ZnO, with different nanostructures have been extensively investigated as photoanode for SSCs. In this study, the band alignment of CdSe and CdS/CdSe–sensitized TiO_2 was systematically investigated. Lee and co-workers reported that a type-II band alignment exists in cascaded CdS/CdSe sensitizer on TiO_2.[18,19] However, a recent study on inverted type-I CdS/CdSe sensitizer by Pan *et al.*, suggests that a type-II band alignment in CdS/CdSe is quite unlikely.[12] Moreover, in a very recent study they have shown one of the highest efficiency of 5.42% using MPA-caped CdSe QDs with TiO_2 electrode.[14] In this study, we carefully investigated the energetics of semiconductor-sensitized TiO_2 to understand the role of the CdS buffer layer. In addition, in order to tune the band gap hence the light absorption property, the solid solution cadmium sulfoselenide (CdS_xSe_{1-x}) was explored in SSCs, which provides an elegant way of adjusting the band energy of light absorber by simply varying the composition without changing its dimension.

Leventis and co-workers have shown that the charge separation remains a major problem when narrow band gap semiconductors such as PbS, PbSe *etc.* are utilized to sensitize metal oxides (*e.g.* TiO_2, ZnO *etc.*) having more negative CB edge as

compared to that of the narrow band gap sensitizers.[20] When TiO_2 is used as electron transporter for PbS-sensitizer based SSCs, only those QDs with higher band gap energy, thus higher CB energy than that of TiO_2 can inject charge carriers into the metal oxides. On the other hand SnO_2 is well known to have much lower conduction band minimum (CBM) and much higher electron mobility than TiO_2. While SnO_2 is notorious as photoanode in DSCs, it may provide a good solution to address the above issues in SSCs.[21,22] Because of the significant lower CBM, it is expected that SnO_2 makes type-II band alignment with most of the moderate band gap semiconductor sensitizers, even larger sized PbS QDs. In addition, owing to the superior carrier transport properties, these injected electrons are expected to be collected efficiently at the external circuit.[21,22] In this context, SnO_2 would enable us to use narrow band gap semiconductor sensitizers, such as PbS with sufficiently large size or even its bulk size so that the near infrared light in the solar spectrum can be harvested for conversion to electricity.

However, compared with TiO_2 the synthesis of SnO_2 nanoparticles is much less studied and only little work has been reported thus far on the preparation of monodispersed SnO_2 nanocrystals and their assemblies of different morphologies in a large scale. Therefore, this study also aims to prepare SnO_2 nanostructures by a facile electrochemical anodization method which is cost effective because of the ambient synthesis conditions.[23]

1.3 Scope

The thesis represents a comprehensive study on TiO_2 and SnO_2-based semiconductor-sensitized solar cells, which covers facile synthesis of nanocrystalline

metal oxides, development of novel semiconductor sensitizers and systematic studies on the band energetics, charge collection/separation characteristics of the devices. Starting from the conventional TiO_2-based SSCs, insightful understanding of the interface has led to a big leap of the power conversion efficiency. Introduction of ternary semiconductor sensitizers makes the selection and preparation of light absorber for TiO_2 more facile and flexible. Going beyond the well-studied TiO_2, SnO_2 was attempted as an alternative photoanode, which greatly improves the cell charge separation efficiency with close to unity external quantum efficiency being achieved. In addition, owing to the lower lying CBM of SnO_2, much enhanced charge injection was achieved when PbS was used as light absorber.

1.4 Organization

This thesis is composed of eight chapters. Chapter 1 presents the background information of the semiconductor-sensitized solar cells. Chapter 2 describes the experimental details and theory related to the characterization of solar cells. Chapter 3 clarifies the role of CdS in CdSe-sensitized TiO_2-based solar cells. Chapter 4 introduces a novel approach of preparing solid solution cadmium sulfoselenide (CdS_xSe_{1-x}) as an alternative to the cascaded CdS/CdSe. Chapter 5 studies the SnO_2-based solar cells sensitized with CdS, CdSe and their cascaded CdS/CdSe and solid solution CdS_xSe_{1-x} sensitizers. Chapter 6 includes the application of narrow band gap PbS sensitizer in SnO_2-based solar cells. Chapter 7 shows the preparation of SnO_2 by a simple and inexpensive electrochemical anodization method followed by a post-treatment technique for assemblies into various superstructures for utilization in SSCs. Chapter 8 ends up with the conclusions of this thesis and recommendations for future study.

2 Theory and Experimental Details

In this chapter, the necessary steps and techniques required for fabrication of semiconductor-sensitized solar cells, such as the photoelectrode, the sensitizer, the hole conducting electrolyte, and the counter electrode are described in detail. In addition, the frequently used state-of-the-art characterization techniques and theories of solar cells are also briefly discussed.

2.1 Preparation of TiO_2 and SnO_2 electrodes

2.1.1 Paste preparation

(1) ***TiO_2 paste***: Titanium (IV) oxide (TiO_2) nanoparticles (Degussa, P25) mixed with a small amount of ethanol were ground by pestle and mortar to break up agglomerates. TiO_2 paste was prepared by a modified method of a previously reported procedure for making TiO_2 paste by Seigo Ito *et al.*[24] In a typical procedure, two kinds of pure ethyl cellulose (EC) powders *ca.* EC (30-50 mPas, #46080, Fluka) and EC (5-15 mPas, #46070, Fluka) were dissolved in ethanol to a 10 w% solution. These 10 w% ethanolic EC solutions were mixed in a ratio of 0.78:1 (w/w), respectively with the ground TiO_2 powder and then α-terpineol and ethanol were mixed with the TiO_2/cellulose mixture. TiO_2 nanoparticles in the mixture were then dispersed using an ultrasonic probe (Sonics, Vibra-Cell) for 1 hour to break the agglomerate and then stirred for another 1 hour using a magnetic stirrer for homogeneous mixing. Ethanol was removed finally from the TiO_2/cellulose mixture while it was homogenized by a three-roll mill (EXAKT M-50, Germany) under a canopy.

(2) ***SnO_2 paste***: The mesoporous SnO_2 electrodes were prepared following a similar procedure for making TiO_2 paste. In a typical procedure, tin (IV) oxide (SnO_2) nanoparticles (Alfa Aesar, Nanoarc) mixed with a small amount of ethanol were ground by pestle and mortar to break up agglomerates. EC solutions and α-terpineol were then mixed with the ground SnO_2 powder following the same procedure for making TiO_2 paste.[24]

2.1.2 Preparation of mesoporous electrodes by screen printing method

Fluorine-doped tin oxide (FTO) coated glass (TEC 15 Ω/□) was cleaned by sequential sonication in 5% Decon 90 solution, deionized water and denatured ethanol (95% ethanol and 5% methanol) for 15 minutes each. Cleaned FTO glass was dried in an electric oven before use. TiO_2 and SnO_2 electrodes were prepared by screen-printing (90T mesh/cm) the above paste onto FTO glass several times in order to get an appropriate thickness. Each printed layer of these metal oxides was relaxed in ethanol vapour in a transparent petri dish to reduce the irregularity in the film. Then it was heated at 125 °C to remove the ethanol followed by cooling to room temperature and another layer deposited. This procedure was repeated several times to get an appropriate thickness of the electrodes. In some cases, a 4 μm thick light scattering layer (WER2-O, Dyesol, 350-450 nm TiO_2 particles) was screen printed onto the TiO_2 layer, but the SnO_2 layer was made of only 10-40 nm particles. The printed films were then sintered in air by heating gradually to 325 °C and holding for 5 minutes, then at 375 °C for 5 minutes, at 450 °C for 15 minutes, and finally at 500 °C for 15 minutes. The resulting mesoporous TiO_2 and SnO_2 electrodes were semi-transparent. The projected area of these electrodes was approximately 0.28 cm^2 (circles with 0.6 cm

diameter). The thickness of the electrodes was determined by an Alpha-Step IQ surface profilometer (KLA-Tencor).

2.1.3 Pre-treatment of TiO_2 and SnO_2 electrodes in $TiCl_4$ aqueous solution

The screen-printed electrodes were then treated with $TiCl_4$ aqueous solution by a chemical bath deposition method.[25] In a typical procedure, the TiO_2 electrodes were soaked in a 40 mM solution of aqueous $TiCl_4$ solution at 70 °C for 30 minutes. Then they were rinsed with deionized water and sintered on a hotplate at 500 °C for 30 minutes. The $TiCl_4$ treatment of TiO_2 electrodes is believed to improve the adhesion and mechanical strength of the nanocrystalline TiO_2 layer. It has been reported that the specific surface area of mesoporous TiO_2 films decreases with $TiCl_4$ treatment but it enhances the adsorption of sensitizers, especially, dye molecules which in turn leads to improve device performance.[25]

The SnO_2 electrodes were pre-treated with the same $TiCl_4$ solution (immersed into 40 mM aqueous $TiCl_4$ solution at 70 °C for 40 minutes), except that the $TiCl_4$ treated SnO_2 electrodes were dried in an electric oven at 70 °C instead of sintering at 500 °C (commonly used for pre-treatment of TiO_2 electrodes) as the sintering at high temperature may lead to form islands of TiO_2 on the SnO_2 surface. This very thin TiO_2 layer on SnO_2 is believed to reduce the density of trap states in its surfaces; thus affects both the photocurrent and the photovoltage in the solar cells.[26]

2.2 Sensitization of mesoscopic TiO_2 and SnO_2 electrodes

Semiconductor sensitizers with excellent physical and chemical properties are desired for efficient light absorption and subsequent charge separation, so that a good overall conversion efficiency of the device is expected. A sensitizer should harvest a wide range of the photons in the solar spectrum, and it must be capable of being grafted itself on the surface of metal oxides for efficient charge injection to the CB of metal oxides. In addition, it should be photoelectrochemically stable for a prolonged period of time. One of the salient properties of semiconductor sensitizers is their size dependent optical properties known as quantum confinement effect which enables absorbing photons with different energies in the solar spectrum. When the size of nanocrystalline semiconductor sensitizers is reduced to smaller than their characteristic Bohr diameter, they are known as QDs, the electrons and holes are spatially confined within the QDs and then their bulk energy bands begin to separate into discrete energy levels.

Various nanocrystalline chalcogenide semiconducting materials such as CdS,[27] CdSe,[28] PbS,[15] Cu_2S,[29] CdTe,[28] Sb_2S_3,[30] *etc.* have been employed as sensitizers for SSCs, which are either grafted by a bifunctional linker molecule or directly deposited on nanocrystalline wide band gap metal oxide semiconductors to harvest the incident photon flux. In this study, CdS, CdSe, CdS_xSe_{1-x}, and PbS were investigated as semiconductor sensitizers for nanocrystalline TiO_2 and SnO_2 electrodes. The exciton Bohr radii of CdS, CdSe and PbS are reported to be 6 nm, 5.6 nm and 18 nm, respectively, implying that the PbS has stronger quantum confinement effect than the former two. Thus it has greater flexibility to tune its band gap energy for harvesting photons of different energies in the solar spectrum.[31-33]

2.2.1 Deposition methods of semiconductor sensitizers

Two approaches are generally used to sensitize the mesoporous electrodes of metal oxides (TiO_2, SnO_2, *etc.*). Firstly, monodisperse QDs are pre-synthesized by the hot-injection method, using precursors and capping agents, such as trioctylphosphine (TOP) or trioctylphosphine oxides (TOPO) under controlled reaction temperature to tailor the size and shape of QDs and engineer their band gap energy. Then they are attached to pre-treated metal oxides with bifunctional linker molecules such as mercaptopropionic acid (MPA) or thioglycolic acid (TGA), in which the carboxyl group attaches to metal oxides and the thiol group attaches to QDs.[12,34] While the monodispersed QDs prepared by this method is ideal for photophysical studies, it has issues like incomplete coverage of sensitizers on metal oxide electrodes impairing the cells' performance: the exposed surface of metal oxide to the electrolyte accelerates the carrier recombination kinetics; the attached insulating bifunctional linker molecules further inhibit the charge injection into metal oxides. In addition, the synthesis of monodispersed QDs normally involves low yield and high temperature methods such as hot injection, greatly increasing the cost.

Secondly, very thin semiconductor layers or sometimes QDs depending on sensitizers are grown directly on metal oxide electrodes by successive ionic layer adsorption and reaction (SILAR) method which is also known as a modified version of chemical bath deposition (CBD). CBD was used to prepare CdS and CdSe on metal oxides until the SILAR method became popular.[35-40] In the SILAR method, the dissolved cationic and anionic precursors adsorb and react on the surface of metal oxides followed by nucleation and growth. While simple, the semiconductor sensitizers deposited by SILAR method are generally polydispersed as a result of non-uniform growth on the surface of metal oxides. In this study, considering its

feasibility and the superior overall performance of the cells, the SILAR method was employed to sensitize the metal oxide electrodes and will be discussed in detail in the following section.

2.2.2 Successive ionic layer adsorption and reaction (SILAR) method

This method was first used to deposit Cu_2O thin film on a glass slide by Ristov *et al.* in 1985,[41] however, an important rinsing step between dips in successive precursor solutions was missing. Afterwards, Ristov's method was modified by adding the rinsing steps and the name SILAR was later adopted by Nicolau and co-workers.[42,43] The SILAR method is based on the adsorption and reaction of the ions from the solutions where the precipitation as often occurs in CBD is avoided by using dilute precursor solutions and frequent washing steps to remove the unnecessary ions by rinsing in between the reactions. The attractive force of ions in the precursor solution toward the substrate is responsible for their heterogeneous adsorption at the solid/liquid interface. Since the basic building blocks are ions, properties of deposited materials can feasibly be controlled by adjusting the deposition parameters such as concentration of precursor solution, type of solvent, temperature, nature of substrate and the number of deposition cycles.

Cationic precursor solution: $CX = C^+ + X^-$

Anionic precursor solution: $AY = A^- + Y^+$

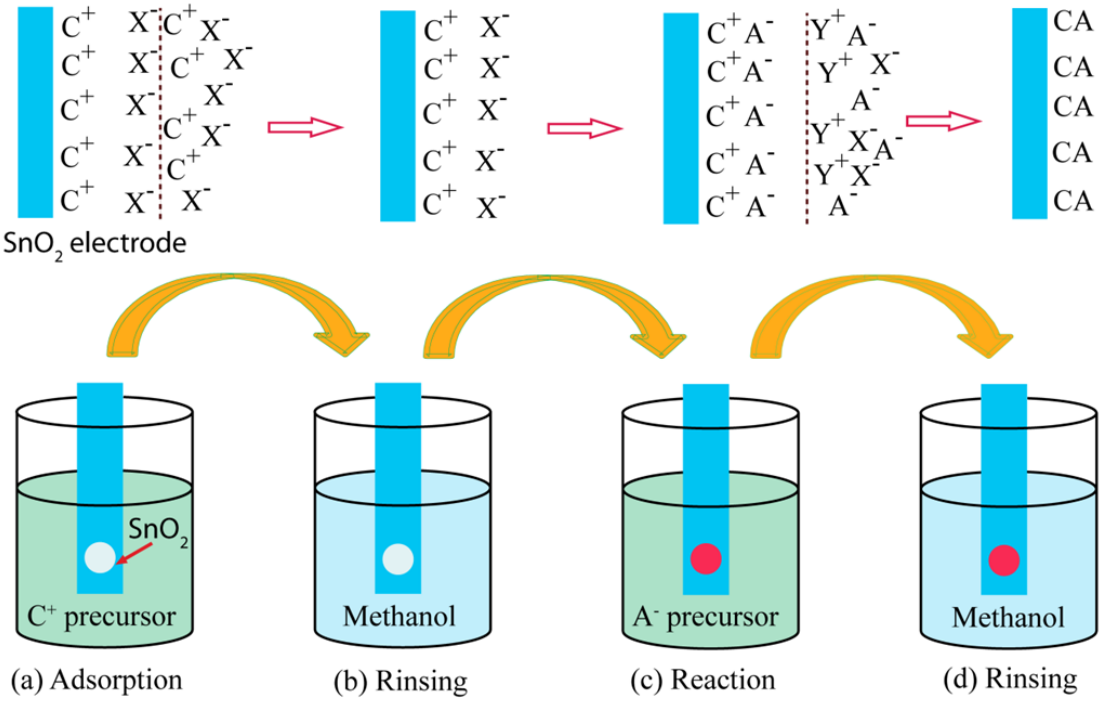

Figure 2. 1 The procedure of the SILAR method, (a) adsorption of cations (C^+) on metal oxide (*e.g.* SnO_2), (b) rinsing off the redundant ions from diffusion layer, (c) reaction between C^+ and anions (A^-) represents the characteristic colour (red) of deposited sensitizer (CA) on SnO_2, and (d) finally the rinsing step removes the redundant cations (Y^+) and anions (X^-).

In a typical procedure of SILAR, the metal oxide electrodes are dipped into the cationic precursor solution to adsorb cations (C^+) and the redundant anions (X^-) are well separated by electrical double layer and remains in the diffusion layer (Fig. 2.1(a)). Following the adsorption of C^+, the redundant anions and excess adsorbed cations are washed away from the diffusion layer by rinsing with solvent (Fig. 2.1(b)). Then the electrodes are usually dried for an effective permeation of anionic (A^-) precursor solution into the mesoporous electrodes where they react with the pre-adsorbed cations (C^+) and then form the desired compound (CA) (Fig. 2.1(c)). Finally, the excess ions are removed from the diffusion layer by rinsing with solvent and only the desired sensitizers remain on the substrates (Fig. 2.1(d)).

Much more reproducible growth of sensitizers have been achieved utilizing dilute precursor solutions and thorough rinsing steps as they may allow uniform nucleation sites for the subsequent growth of semiconductor sensitizers.[40] In addition, solvent with low surface tension is required to facilitate the permeation of precursor solution deep into the mesoporous films; thus a conformal layer of semiconductor sensitizers can be deposited on the metal oxide substrates. Due to the superior wetting capability of methanol and ethanol on mesoporous TiO_2 and SnO_2 to deionized water, they are mainly used as solvent in this study. Moreover, fast removal of methanol or ethanol during drying process is also advantageous for penetration of precursor solution in the subsequent dipping cycles; hence thin sensitizer layers can be prepared without clogging the pores within the mesoporous TiO_2 or SnO_2 electrodes.[40] However, because of low solubility of some precursors, *e.g.* sodium sulfide nonahydrate ($Na_2S.9H_2O$) in methanol, a mixture of methanol and water (1/1, v/v) is normally required.

2.3 Preparation of semiconductor-sensitized photoelectrodes

2.3.1 CdS, CdSe and cascaded CdS/CdSe-sensitized mesoscopic TiO_2 and SnO_2 electrodes

Kapton tape was used to mask the bare FTO, leaving the mesoscopic TiO_2 and SnO_2 electrodes (0.6 cm diameter) uncovered, they were sensitized with CdS and CdSe using the previously described SILAR method. In a typical procedure, the TiO_2 and SnO_2 electrodes were immersed in a solution containing 0.02 M cadmium nitrate tetrahydrate ($Cd(NO_3)_2 \cdot 4H_2O$, Fluka, >99.0%) in methanol for 1 minute, to allow Cd^{2+} to adsorb onto the TiO_2, and then rinsed with methanol for 1 minute to remove

the excess Cd^{2+} and unnecessary anions from the diffusion layer. Electrodes were then dried in a gentle stream of N_2 for 1 minute. The dried electrodes were then dipped into a solution containing 0.02 M sodium sulfide nonahydrate ($Na_2S{\cdot}9H_2O$, Sigma Aldrich, >98%) in a mixture of methanol and deionized water (1:1, v/v) for 1 minute, where the pre-adsorbed Cd^{2+} reacts with S^{2-} to form the desired CdS. Electrodes were then rinsed in methanol for 1 minute and dried again with N_2. This procedure for depositing CdS was repeated several times to get the desired amount on the TiO_2 and SnO_2 electrodes.

CdSe has been prepared by the CBD method based on slow release of selenide ions (Se^{2-}) from Na_2SeO_3 in the presence of Cd^{2+}.[37,38,44] However, this method requires prolonged time or sometime overnight to deposit desired amount of materials on substrate, which also has reproducibility issues. In addition, the poor selectivity of deposition on substrate rarely makes a conformal layer, and thus generates inefficient solar cell performance. In a modified approach, Lee *et al.*[28] stabilized the Se^{2-} in ethanol by reducing the selenium dioxide (SeO_2) with a sodium borohydride ($NaBH_4$) reducer in argon atmosphere as follows:

$$SeO_2 + 2NaBH_4 + 6C_2H_5OH = Se^{2-} + 2Na^{+} + 2B(OC_2H_5)_3 + 5H_2 + 2H_2O$$

This stabilized Se^{2-} was used to prepare CdSe by the SILAR method. The Se^{2-} solution was prepared by mixing 0.333 g SeO_2 (Sigma-Aldrich, 99.9%) and 0.216 g $NaBH_4$ (Sigma Aldrich, 99.99%) in 100 ml ethanol according to the above reaction. In a typical procedure, the TiO_2 and SnO_2 electrodes were dipped into a solution containing 0.03 M $Cd(NO_3)_2{\cdot}4H_2O$ in ethanol for 30 seconds and rinsed with ethanol for 2 minutes, then dried for 2 minutes in an argon atmosphere. Subsequently, the

dried electrodes were dipped into a solution containing 0.03 M Se^{2-} for 30 seconds. One deposition cycle was completed by further rinsing in ethanol for 2 minutes and drying again in an argon atmosphere for 2 minutes. This procedure was repeated several times to get different amounts of CdSe on the TiO_2 and SnO_2 electrodes. To prepare cascaded CdS/CdSe electrodes, CdS was deposited at first and then CdSe was deposited on top of the CdS-coated TiO_2 and SnO_2 electrodes.

The amount of deposited materials on mesoporous electrodes is controlled by varying the deposition cycles of CdS and/or CdSe. It is believed that the nucleation of CdS or CdSe occurs in first cycle and then they grow via a layer-by-layer structure fashion in the subsequent deposition cycles:

Nucleation: $Cd^{2+} + Se^{2-} \rightarrow CdSe$

Growth: $(CdSe)_m + Cd^{2+} + Se^{2-} \rightarrow (CdSe)_{m+1}$

Aggregation: $(CdSe)_m + (CdSe)_n \rightarrow (CdSe)_{m+n}$

where *m* and *n* denotes the number of deposition cycles by the SILAR method. Aggregation may also happen and give rise to the formation of islands, thus blocking the mesopores in TiO_2 and SnO_2 electrodes. This can be avoided by optimizing the deposition conditions such as the precursor concentration, types of solvent, reaction time and number of deposition cycles *etc*.

2.3.2 CdS_xSe_{1-x}-sensitized mesoscopic TiO_2 and SnO_2 electrodes

In a typical procedure, at first, one cycle CdS was deposited onto TiO_2 and SnO_2 electrodes by the above SILAR method. Following the CdS deposition, one cycle of

CdSe was then deposited immediately onto the CdS-coated TiO_2 and SnO_2 electrodes by the above SILAR method. Following the CdSe deposition, one cycle of CdS was deposited again on CdS/CdSe-coated TiO_2 and SnO_2 electrodes. This alternate SILAR deposition of CdS and CdSe was repeated several times to get a homogeneous mixture of CdS_xSe_{1-x} on the TiO_2 and SnO_2 electrodes. The number of alternate deposition cycles by SILAR was repeated until the desired amount of CdS_xSe_{1-x} is obtained for an optimized solar cell performance.

2.3.3 PbS/CdS-sensitized mesoscopic SnO_2 and TiO_2 electrodes

The mesoscopic SnO_2 and TiO_2 electrodes were sensitized with PbS and CdS using a previously reported SILAR methods.[28,45] In a typical procedure, the SnO_2 electrodes (pre-treated with $TiCl_4$ solution) were immersed in a solution containing 0.02 M lead nitrate ($Pb(NO_3)_2$, Aldrich, >99.0%) in methanol for 1 minute in an argon-filled glove box, to allow Pb^{2+} to adsorb onto the SnO_2, and then rinsed with methanol for 1 minute to remove the excess Pb^{2+}. Electrodes were then dried for 1 minute in argon atmosphere. The dried electrodes were then dipped into a solution containing 0.02 M $Na_2S{\cdot}9H_2O$ in a mixture of methanol and deionized water (1:1, v/v) for 1 minute, where the pre-adsorbed Pb^{2+} reacts with S^{2-} to form the desired PbS on metal oxide substrates. Electrodes were then rinsed in methanol for 1 minute and dried again for 1 minute. This procedure was repeated to deposit (grow) a few layers of PbS onto SnO_2 electrodes as described below:

$$SnO_2 + Pb^{2+} \rightarrow SnO_2/Pb^{2+}_{ad.}$$

$$SnO_2/Pb^{2+}_{ad.} + S^{2-} \rightarrow SnO_2/PbS$$

Following the PbS deposition, a few layers of CdS were then deposited subsequently also by the SILAR method using ethanol as the solvent. In elaboration, to deposit CdS onto PbS-coated SnO_2, the electrodes were dipped into a solution containing 0.02 M $Cd(NO_3)_2 \cdot 4H_2O$ in ethanol for 1 minute, and rinsed with ethanol for 1 minute, then dried for 1 minute. Subsequently, the dried electrodes were dipped into a solution containing 0.02 M $Na_2S \cdot 9H_2O$ in a mixture of methanol and deionized water (1:1, v/v) for 1 minute. Then electrodes were dried again for 1 minute and repeated several times to get a few layers of CdS. For the best-performed electrodes, a buffer CdS layer was deposited prior to the PbS deposition. Alternating layers of PbS and CdS were also deposited onto SnO_2 electrodes to tune the optical properties of the resulted electrodes. All the deposition was performed in an argon-filled glove box, as PbS is not very stable in air. For comparison, TiO_2 electrodes were also used where the rest of the fabrication procedure was identical to that used for cascaded and alternately deposited PbS/CdS-sensitized SnO_2 photoelectrodes. It is worth mentioning that the precursor solutions of CdS, CdSe and PbS are toxic, thus proper safety measures should be taken according to the materials' safety data sheet.

2.4 ZnS passivation layer

ZnS is a wide band gap (3.6–3.8 eV) semiconductor which is widely used to coat narrow band gap semiconductor sensitizers to protect them from aggressive electrolyte species under irradiation in SSCs. Yang *et al.* showed that a ZnS passivation layer prepared by SILAR on a PbS/CdS-sensitized TiO_2 not only prevented the photocorrosion of PbS/CdS, but also greatly improved the performance of the cells by suppressing the recombination.[46] Thereafter, ZnS post-treatment has become an essential part of photoanode design, especially for SILAR grown

sensitizers, and it is widely used as passivation layer in SSCs because of the dramatic improvement in photovoltaic performance.[23,37,47-49] These improvements are attributed to the passivation of surface states (which acts as recombination centre for photo-excited charge carriers) of CdS, PbS sensitizers by ZnS.[49] As a result, charge separation and collection in the cells are generally enhanced. In addition, it is believed that the higher conduction band energy of ZnS than that of sensitizer acts as a barrier preventing electron resided in the sensitizer from recombining with the acceptor states in the electrolyte. However, the valence band offset of the straddled band alignment of ZnS to that of the sensitizers should also act as a barrier for the regeneration process – hole injection from sensitizer to electrolyte, which could be realized presumably by the specific adsorption of electrolyte donor states on the surface of the very thin ZnS layer facilitating the regeneration process.

The deposition of ZnS passivation layer on the CdSe and CdS/CdSe-coated TiO_2 and SnO_2 electrodes was carried out by SILAR method using 0.1 M aqueous zinc acetate dihydrate ($Zn(CH_3COO)_2 \cdot 2H_2O$, Sigma Aldrich, >99.5%) and 0.1 M aqueous $Na_2S \cdot 9H_2O$, dipping for 1 minute in each solution, with 1 minute of rinsing in deionized water between each immersion in a precursor solution.[45,48-50] It is worth mentioning that the deionized water should be used for ZnS deposition for stable device performance. Attempts were carried out to deposit ZnS passivation layer using methanol and ethanol as solvent for precursor solutions, however, the cells were found unstable, presumably the deposited ZnS was less compact which led to incomplete coverage of sensitizers. All the CdSe, CdS/CdSe, CdS_xSe_{1-x} and PbS/CdS-sensitized TiO_2 electrodes used in this study were coated with two ZnS passivation layers (two SILAR cycles).

2.5 Redox electrolyte

In a photoelectrochemical solar cell, a redox couple is required to regenerate the oxidized sensitizers by scavenging the photogenerated holes in the photoanode. The iodide/triiodide (I^-/I_3^-) redox couple has been extensively used and optimized in DSCs but it is corrosive to most metals and semiconductor sensitizers, causing a rapid decay of photocurrent.[51,52] Therefore, alternative iodine-free redox couples or hole-transporting materials, such as Ferrocene/Ferrocenium,[53] cobalt bipyridyl complex ($Co(bpy)_3^{2+/3+}$),[54] sulfide/polysulfide electrolyte (S^{2-}/S_x^{2-}),[55] and spiro-OMeTAD,[40,56] *etc.* have been extensively explored in SSCs to stabilize the sensitizers. Among these, the S^{2-}/S_x^{2-} demonstrates the best device performance as a result of superior asymmetric kinetics between sensitizer regeneration and recombination.

Upon illumination the generated electrons are injected into the conduction band of the metal oxide. While transporting through the mesoscopic photoanode to the external circuit, these high-energy electrons undergo recombination via different channels and meanwhile the holes remained in the sensitizer CdSe are scavenged by the electron donor species in the polysulfide electrolyte (S^{2-}) as shown below.[57]

$$CdSe + h\nu \longrightarrow CdSe\,(h^+ + e^-)$$

$$CdSe\,(h^+ + e^-) + TiO_2 \longrightarrow CdSe\,(h^+) + TiO_2(e^-)$$

$$CdSe\,(h^+) + S^{2-} \longrightarrow CdSe + S^{-\cdot}$$

In order to have better wettability towards the surface of the mesoscopic photoanode and at the same time to have better dissociation of ionic species in the electrolyte, a mixture of methanol/water (7/3, v/v) was frequently reported as a

solvent. However, methanol was reported to be a sacrificial agent, which decomposes on the surface of the photoelectrode under illumination, giving rise to an overestimated photocurrent. In addition, a modified organic sulfide/polysulfide electrolyte, tetramethylammonium sulfide/polysulfide $[CH_3)_4N]_2S/[(CH_3)_4N]_2S_n$ in 3-methoxypropionitrile solvent has been reported with a very positive redox potential; however, the extremely low solubility of the sulfide-based compound remains a question for efficient sensitizer regeneration.[58] More recently, pyrrolidinium ionic liquid-based S^{2-}/S_x^{2-} electrolyte reported by Ivan *et al.* has shown great promise for long-term stability of SSCs.[59] In this study, unless otherwise stated, an aqueous sulfide/polysulfide electrolyte composed of 1 M S, 1 M $Na_2S{\cdot}9H_2O$ and 0.1 M NaOH was generally employed to avoid any side reactions.[45] For efficient regeneration of semiconductor sensitizer, the redox potential of the electrolyte must be more negative than the HOMO of semiconductor sensitizer. However, too negative redox potential would be detrimental to the photovolatge of the device. Therefore, there should have an optimal driving force for sensitizer regeneration efficiency. Because of the chemical compatibility of the chalcogenide semiconductor sensitizers and ultrafast hole extraction capabilities, the S^{2-}/S_x^{2-} redox couple was used in this study.

2.6 Counter electrodes (cathodes)

Counter electrodes with more catalytic activity are desired for fast reduction of redox species in SSCs. Platinized FTO cathode has shown good catalytic activity toward I^-/I_3^- redox couple in DSCs. However, these noble metals such as Pt,[37] Au,[18] were reported not to be good electrocatalysts for the S^{2-}/S_x^{2-} redox couple. As such, numerous counter electrode materials have been extensively investigated, some of

which have shown excellent electrocatalytic property toward S^{2-}/S_x^{2-}, such as CoS,[60,61] PbS,[61,62] Cu_2S,[45,55,61,63] and carbon,[64] *etc*. However, some of these materials are not stable in the long run because of lower mechanical integrity and sometimes even contaminate the photoanode.[61] The counter electrode should have high conductivity, mechanical and electrochemical stability. We observed that while the platinized FTO cathode is not as good as the sulfide-based cathodic materials, it works reasonably well in SSCs and in this study it will be used to make stable devices for impedance spectroscopic measurement. Instead, Cu_2S cathode was employed to evaluate the photovoltaic characteristics of SSCs. The following subsections describe the preparation of these two cathodes.

2.6.1 Transparent platinized FTO cathodes

Platinized FTO counter electrodes were prepared with small holes drilled into one corner on FTO to facilitate injection of electrolyte into the cell. The FTO was cleaned by sequential sonication in aqueous 5% Decon 90 solution, deionized water and denatured ethanol (95% ethanol and 5% methanol) for 15 minutes each. Following cleaning, FTO pieces were heated to 400 °C in a hot air stream for 15 minutes to get rid of any organic contaminants. Once they had cooled to room temperature, the Pt catalyst 15 mM hexachloroplatinic acid (H_2PtCl_6) in ethanol was spread over the FTO and kept in a transparent petri dish ~2 minutes to dry. Once the ethanol had evaporated, they were heated again to 400 °C in a hot air stream for 15 minutes for thermal decomposition of Pt precursor as described by Ito *et al*.[24] Then they were immediately used for device fabrication.

2.6.2 Opaque Cu_2S cathode on brass sheet

Brass sheet (alloy 260, Alfa Aesar) was polished by sand paper and de-agglomerated alumina suspension (particles' size 1.00 and 0.05 microns) sequentially and cleaned by sonication in deionized water. The clean brass sheet was then etched in 37% HCl at 70 °C for 5 minutes to expose more copper from the copper-zinc matrix and the yellowish colour of the brass changed to a dark red which is the typical colour of copper sheet.[45,61,65,66] The etched brass was then rinsed with deionized water to remove residual HCl and dried at 70 °C in an electric oven. One drop of an aqueous polysulfide solution containing 1 M S, 1 M $Na_2S{\cdot}9H_2O$ and 0.1 M NaOH was added onto an unmasked part (7 mm diameter) of the etched brass causing it to suddenly become black, indicating the formation of Cu_2S. Then it was dried under vacuum before fabricating solar cell with photoanode.

2.7 Fabrication of the sensitized mesoscopic solar cells

To fabricate SSCs with Cu_2S cathodes, a hole was made within 1 mm from the edge of the TiO_2 and SnO_2 layer on the photoanode prior to the deposition of semiconductor sensitizers. For the cells used for impedance study, the platinized FTO counter electrodes were made by drilling a hole on FTO prior to the deposition of Pt catalyst. CdSe, CdS/CdSe, CdS_xSe_{1-x}, and PbS/CdS-sensitized TiO_2 and SnO_2 photoanodes and cathodes were sealed together in a sandwich configuration using a hot-melt polymer (Surlyn, DuPont). The inter-electrode space was filled with S^{2-}/S_x^{2-} electrolyte by vacuum backfilling. Holes were sealed using a small piece of hot-melt polymer and a microscope coverslip.

2.8 UV-vis measurement of sensitized mesoscopic electrodes

Light absorption can be described by the Beer-Lambert's law:

$$I = I_0 \mathrm{e}^{-\alpha(\lambda)l}$$

where I, I_0, α (λ), and l are the transmitted light intensity, incident light intensity, light absorption coefficient, and film thickness, respectively. Direct band gap semiconductors are generally capable of absorbing more light than indirect band gap ones because of higher absorption coefficient (>10^4 cm^{-1}) in the former and the requirement of phonon interaction in the latter. A simple calculation shows that ~1 μm thin film of direct band gap semiconductor, such as CdTe, CIGS *etc.*, can meet the light absorption equivalent to that of >100 μm thick indirect band gap crystalline silicon. Therefore, the materials consumption, hence the cost can be significantly reduced as evident in thin film photovoltaic systems. Optical light absorption spectroscopy was used to measure the optical density of the CdS, CdSe, CdS/CdSe, CdS_xSe_{1-x} and PbS/CdS-sensitized TiO_2 or SnO_2 electrodes in this study and will be discussed accordingly in different chapters.

As a direct band gap semiconductor, the optical absorption near the band edge follows the formula:

$$(\alpha h\nu) = \mathrm{A}(h\nu - \mathrm{E_g})^{\frac{1}{2}}$$

where h, ν, $\mathrm{E_g}$, and A are Planck's constant, frequency of light, optical band gap, and a proportionality constant, respectively. The $\mathrm{E_g}$ of a semiconductor sensitizer can thus

be obtained from the plots of $(\alpha h\nu)^2$ versus photon energy $(h\nu)$. This relationship gives the E_g by extrapolating the straight portion of $(\alpha h\nu)^2$ against photon energy $(h\nu)$, which is known as a Tauc plot.[67] In this study, the optical properties of the sensitized mesoscopic electrodes were carried out in transmission mode utilizing a single beam in a Shimadzu UV-Vis-NIR spectrophotometer (Solidspec-3700).

2.9 Characterization of the sensitized mesoscopic TiO_2 and SnO_2 solar cells

A solar cell can be represented as a current source connected in parallel with a rectifying diode. The corresponding *j-V* characteristic is described by the Shockley equation.

$$j(V) = j_{sc} - J_0(e^{\frac{qV}{mk_BT}} - 1)$$

where k_B is the Boltzmann constant, *T* is the absolute temperature, *q* is the elementary electron charge, *V* is the voltage at the terminals of the cell, J_0 is the diode saturation current density, j_{sc} is the short circuit photocurrent density which is closely related to the photon flux incident on the cell and *m* ($1< m <2$) is the diode ideality factor.

Figure 2.2 shows the current density as a function of voltage (*j-V*) of a cell in which the maximum value of photocurrent and photovoltage in a cell is represented by the short circuit photocurrent density (j_{sc}) and open circuit photovoltage (V_{oc}), respectively. However, in a practical cell, the j_{sc} and V_{oc} cannot be achieved, simultaneously, rather a maximum photocurrent density (j_m) and photovoltage (V_m) corresponding to a maximum power point (P_{max}) for an optimized load is observed, as

shown in Figure 2.2. Therefore, an overall power conversion efficiency (η) of a cell is given by the following expression:

$$\eta = \frac{j_m V_m}{P_{\text{in}}} = \frac{j_{sc} V_{oc}}{P_{\text{in}}} ff$$

where P_{in} is the incident irradiance (W m^{-2}) and ff is the fill factor. The j-V characteristics also depend on series resistance (R_s) and shunt resistance (R_{sh}). A lower R_s value is desired as it determines the current flow through the device, and it includes the charge transport resistance through the photoanode and FTO contact, resistance in electrolyte and charge transfer resistance at counter electrodes. In contrast, a higher value of R_{sh} is desired which implies negligible leakage current in the device.

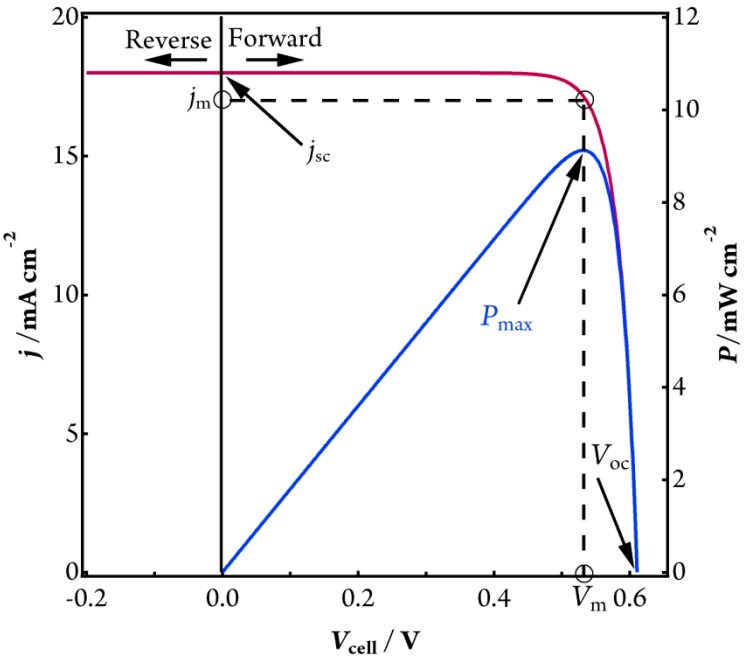

Figure 2. 2 Simulated j-V characteristics based on Shockley equation and power output of a solar cell with j_{sc} = 18 mA cm^{-2}, J_o = 10^{-9} mA cm^{-2} and diode ideality factor m = 1.

The j_{sc} can be calculated by integrating the incident photon flux obtained from the standard spectral irradiation spectra AM 1.5G, as shown in Figure 2.3, and the incident photon-to-current conversion efficiency (IPCE) of a solar cell. Where $b_s(\lambda)$ is the solar photon flux.

$$j_{sc} = q \int b_s(\lambda)\ IPCE\ (\lambda)\ d\lambda$$

The *IPCE* (λ) is related to the light harvesting by sensitizers. It can also be referred to as the external quantum efficiency (*EQE*) of the solar cell, and it is defined as the number of photogenerated electrons in the external circuit divided by the number of incident photons with different wavelength.

$$IPCE(\lambda) = \frac{Photocurrent\ density}{Wavelength\ x\ Photon\ flux} = \eta_{\mathrm{lh}}(\lambda)\,\eta_{\mathrm{sep}}(\lambda)\,\eta_{\mathrm{col}}(\lambda)$$

$$\eta_{\mathrm{lh}}(\lambda) = 1 - 10^{-\alpha(\lambda)l}$$

$$\eta_{\mathrm{sep}}(\lambda) = \eta_{\mathrm{inj}}(\lambda)\eta_{\mathrm{reg}}(\lambda)$$

where the light harvesting efficiency $\eta_{\mathrm{lh}}(\lambda)$ is estimated from the optical density (OD) spectra of the photoanode at wavelength $\lambda\,(nm)$, and $\alpha(\lambda)$ is the light absorption coefficient of the sensitized photoanode, which in turn is determined by the molar extinction coefficient, and the concentration of the sensitizing semiconductor in the photoanode. The charge separation efficiency $\eta_{\mathrm{sep}}(\lambda)$ depends on the carrier injection efficiency $\eta_{\mathrm{inj}}(\lambda)$ from the excited sensitizer into the conduction band of metal oxide (TiO_2, SnO_2 *etc.*) and on the sensitizer regeneration efficiency $\eta_{\mathrm{reg}}(\lambda)$ which further depends on background electron concentration. The

charge collection efficiency $\eta_{col}(\lambda)$ measures how efficiently the injected carrier can be collected at the external circuit which can be measured by impedance measurement.

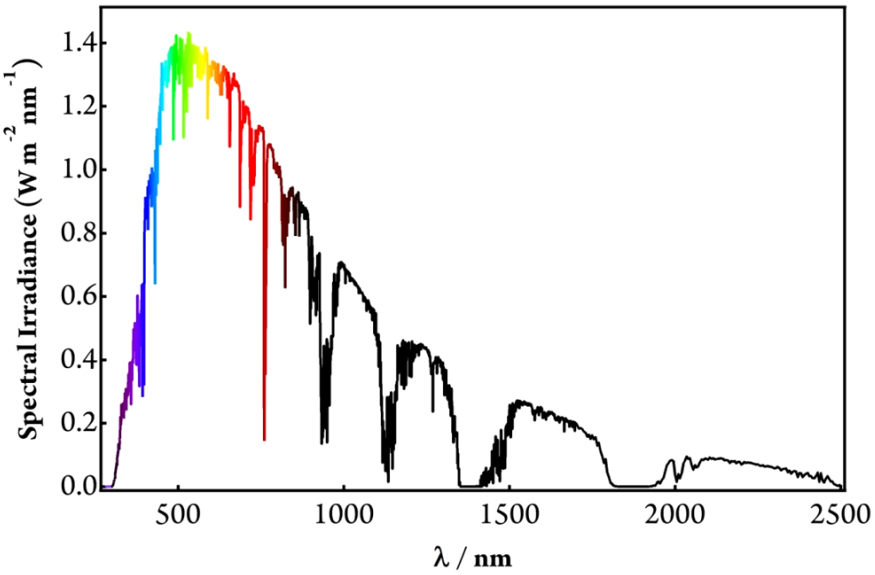

Figure 2. 3 Air Mass 1.5 Global (AM 1.5G) solar spectrum from ASTM G173-03 reference spectrum (energy as a function of wavelength).

The AM 1.5G (Air Mass 1.5 Global) spectrum is adopted as the standard spectrum for testing solar cells as it includes both directs and diffusive radiation. When the absorption bands of the atmosphere and a dilution factor of 1.56 x 10^{-5} are considered for blackbody spectrum at temperature 5800 K, its total power of the photon distribution becomes approximately similar to the AM 1.5G spectrum.[68] The integrated power density of AM 1.5G is 100 mW cm^{-2} with the spectral intensity distribution matching that of sunlight at the earth's surface at an incident angle of 48.2°. Almost 50% of the integrated power resides in the infrared spectral region and ~45% is in the visible region and ~5% in the UV region, suggesting that an ideal light absorber should absorb both visible and infrared light in the solar spectrum.

Photocurrent-voltage (*j*-*V*) characteristics under simulated AM 1.5 illumination were measured using a Keithley Source Meter and the PVIV software package (Newport). Simulated AM 1.5 illumination was provided by a Newport solar simulator and the light intensity was measured using a calibrated Si solar cell. The cells were scanned from forward to reverse bias at a scan rate of 12.5 mV/sec for *j*-*V* measurements. The active area of the cells was defined by a mask to be 0.12 cm^2.

IPCE spectra were measured with a spectral resolution of *ca.* 5 nm using a 300 W xenon lamp and a grating monochromator equipped with order sorting filters (Newport/Oriel). The incident photon flux was determined using a calibrated silicon photodiode (Newport/Oriel). Photocurrents were measured using an auto-ranging current amplifier (Newport/Oriel). Controlling of the monochromator and recording of photocurrent spectra were performed using a PC running the TRACQ Basic software (Newport).

Impedance spectra were measured using an Autolab potentiostat/galvanostat and the Nova 1.6 software package. Experiments were performed with cells under illumination provided by a red LED (centre wavelength λ = 627 nm) and biased at the V_{oc} induced by the illumination. The highest light intensity used was sufficient to produce a V_{oc} approximately equal to that obtained under AM 1.5 1 Sun illumination and the incident photon flux was of the order of 10^{17} cm^{-2} s^{-1}. A 15 mV RMS voltage perturbation was used and the frequency range was 10^5–0.1 Hz. Different illumination intensities were achieved using neutral density filters mounted in an automated filter wheel system (Newport), which was controlled by the Nova 1.6 software. Impedance measurements were carried out in order of descending light intensity.

3 CdSe-Sensitized Mesoscopic TiO_2 Solar Cells: the Role of CdS Buffer Layer

3.1 Introduction

Semiconductor nanocrystals, especially QDs, have been attracting considerable attention due to their potential use as sensitizers in sensitized mesoscopic solar cells.[69,70] The ease with which the band gap can be tuned by varying particle size, and other inherent high extinction coefficients, makes them very promising candidates for efficient light harvesting materials in solar cells.[15,34,69-71] Good progress has been made in improving the power conversion efficiency of SSCs in the past few years by optimizing components constituting the device, such as the microstructure of the photoanode, the configuration of semiconductor sensitizers on the metal oxide, the counter electrode, and the electrolyte *etc*.[18,36,45,63,72-74] Utilization of light from the visible to the near infrared region in the solar spectrum and favorable band alignment for efficient charge separation remain the key requirements for the further improvement of device performance.

Among various semiconductor sensitizers, II-VI compound semiconductors CdS,[27,51,75] and CdSe[28,44,76,77] are the most widely used to sensitize nanocrystalline TiO_2, either alone or together.[18,35,45,48,63,72,74,78-81] The loading of CdS or CdSe onto a mesoscopic photoanode can be achieved by various wet chemistry methods, such as CBD, SILAR, or chemical adsorption of the as-synthesized nanocrystals of CdS or CdSe with the help of linker molecules. Of these methods, SILAR offers easy fabrication as well as the most efficient SSCs to date. Under optimum conditions, a

power conversion efficiency of 4.92% has been attained under AM 1.5 100 mW cm^{-2} illumination when cascaded CdS/CdSe-sensitized TiO_2 was used along with a polysulfide electrolyte.[63] Kamat *et al*., recently showed 5.42% efficient cell using a transition metal, Mn^{2+}-doped CdS/CdSe-sensitized TiO_2 as photoanode. The Mn^{2+} dopant species was incorporated into the CdS and CdSe QDs, which created midgap states in the QDs and due to slow Mn d-d transition, carrier lifetimes were substantially increased.[13] The superior performance of the CdS/CdSe cascade was attributed to the presence of CdS underneath CdSe serving as a buffer layer, which on one hand was believed to facilitate the charge separation as a result of the favorable staircase band alignment at the CdS/CdSe interface (type-II heterojunction),[19,82] and on the other hand promotes the subsequent deposition of CdSe and consequently enhances light harvesting at long wavelength.[35,78]

However, in a recent study, Bisquert and co-workers demonstrated that CdSe-sensitized TiO_2 electrodes perform better in devices than CdS/CdSe-sensitized electrodes when more CdSe was deposited on TiO_2.[45] This observation raises an important question: is the superior performance of CdS/CdSe-sensitized TiO_2 observed previously a result of facilitated charge separation or simply because of enhanced light harvesting? Unfortunately, the CdSe electrode in the aforementioned study had a much higher optical density (OD) than that of the CdS/CdSe electrode, making the comparison difficult. Therefore, in this study CdSe-sensitized TiO_2 electrodes of nearly identical OD to the best-performed CdS/CdSe electrodes were fabricated and their photovoltaic properties were scrutinized. The latter was examined by varying the thickness of CdS and CdSe layers, and 5CdS/5CdSe (5 is the number of deposition cycles) was found to be the best cascade-structured sensitizer under the present SILAR deposition conditions, which was then used as a reference to the CdSe

cells. It is interesting that CdSe-sensitized TiO_2 exhibits better performance than the CdS/CdSe in the study. Careful optical studies reveal that the presence of CdS significantly promotes the growth of CdSe, which then greatly improves light harvesting of the electrode. However, when sufficient CdSe is deposited on TiO_2 by its own, better performance was observed due to the enhanced photo-conversion of long wavelength photons and eliminated recombination at TiO_2/sensitizer interface.

3.2 Morphology and structural characterization of CdSe and CdS/CdSe-sensitized TiO_2

Figure 3.1(a) and 3.1(b) show a low- and high-resolution transmission electron microscopy (HRTEM) image of the as-grown CdSe on ~25 nm sized TiO_2 crystal grains after 7 cycles of SILAR deposition (denoted as 7CdSe). It is evident that while the lattice fringes of the TiO_2 crystal grain with *d*-spacing 0.35 nm are clearly seen, its surface is conformally covered with a 3–4 nm thick amorphous layer, which is presumably the deposited CdSe. For comparison, the cascade 5CdS/5CdSe (the best performing sensitizer) was also measured (Fig. 3.1(c)). However, layers of CdS and CdSe on the edge of TiO_2 crystal grains were not seen rather an amorphous like material was observed, which is presumably the deposited 5CdS/5CdSe.

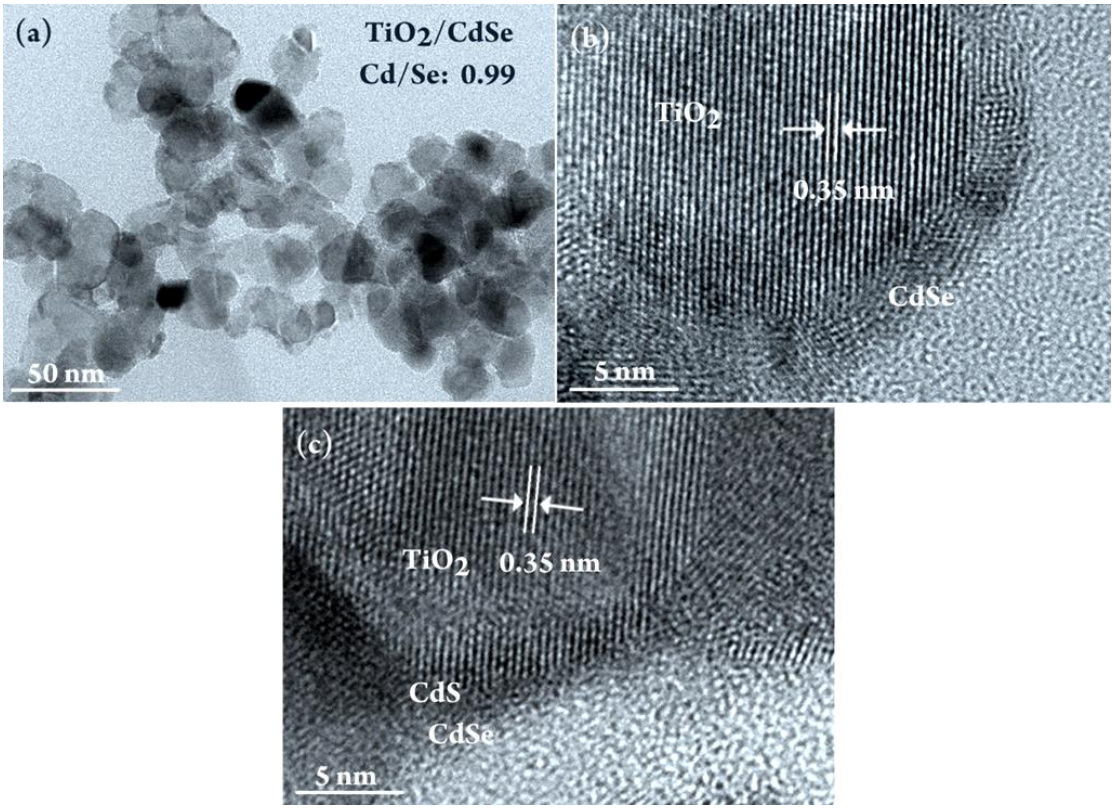

Figure 3. 1 (a) Low-resolution TEM and (b) High-resolution (HRTEM) images of 7CdSe deposited on TiO_2 nanoparticles (Degussa, P25). HRTEM of the cascaded 5CdS/5CdSe deposited on TiO_2 is shown in (c).

The CdS, CdSe and CdS/CdSe-sensitized TiO_2 electrodes were further characterized by X-ray diffraction (XRD) as shown in Figure 3.2, where only TiO_2 reveals distinct diffraction peaks, indicating that the as-grown sensitizers on TiO_2 are amorphous in nature. However, all the electrodes except individual CdS show broadened characteristic diffraction peaks after heat treatment at 350 °C for 2 hours in an evacuated (~10^{-6} mbar) quartz tube, indicating the presence of crystallized phase of CdSe. The presence of CdS causes a slight shift and broadening of the XRD peaks of CdS/CdSe electrode with respect to the pure CdSe which is plausibly a result of alloying between CdS and CdSe at elevated temperature considering the favorable thermodynamics for near ideal miscibility between these two materials and their

intimate contact at mesoscopic level. In order to avoid interference from the FTO substrate, all samples for XRD measurements were made with TiO_2 films printed on microscope glass slides. As shown in Figure 3.2, both the rutile (JCPDS No. 89-4920) and anatase (JCPDS No. 89-4921) phases are clearly seen in the bare TiO_2 (Degussa, P25) electrode. Energy-dispersive X-ray spectroscopy (EDS) elemental analysis was used to determine the atomic ratio. With the uncertainty of <0.1 wt% of the EDS measurement, it shows that Cd/Se is 0.99 (0.98±0.1) in 7CdSe, and Cd/(S+Se) is 0.98 (0.97±0.1) in 5CdS/5CdSe, being almost stoichiometric. These as-prepared electrodes were used directly for optical measurements, solar cell fabrication and characterizations in the subsequent sections.

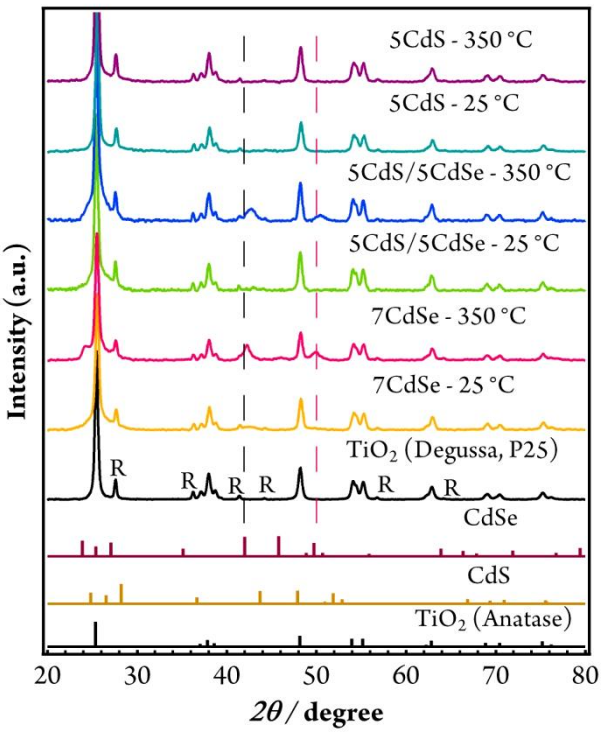

Figure 3. 2 X-ray diffraction patterns of 7CdSe, 5CdS and 5CdS/5CdSe-coated TiO_2 electrodes (Degussa, P25) on microscope glass slides before and after heat treatment. The standard 2θ values for TiO_2 (anatase), rutile (R) phase in TiO_2 (Degussa, P25), wurtzite CdS and CdSe crystals are also shown for comparison.

3.3 Optical properties of sensitized mesoscopic TiO_2 electrodes

The absorption spectra of SILAR-deposited sensitizers on TiO_2 are depicted in Figure 3.3. While the maximum absorption appears at ~400 nm for all the electrodes, the absorption onset of CdSe is significantly red shifted and its peak absorbance is much greater than that of CdS. Similarly, the absorption onsets of the 5CdS/*n*CdSe electrodes shift to longer wavelengths with increasing deposition cycles (*n* = 1-5) of CdSe from ~550 nm for 5CdS/CdSe to ~700 nm for 5CdS/5CdSe, much longer than the onsets for individual CdS and CdSe layers for the same number of SILAR deposition cycles, consistent with the previous observations of Lee *et al*.[78]

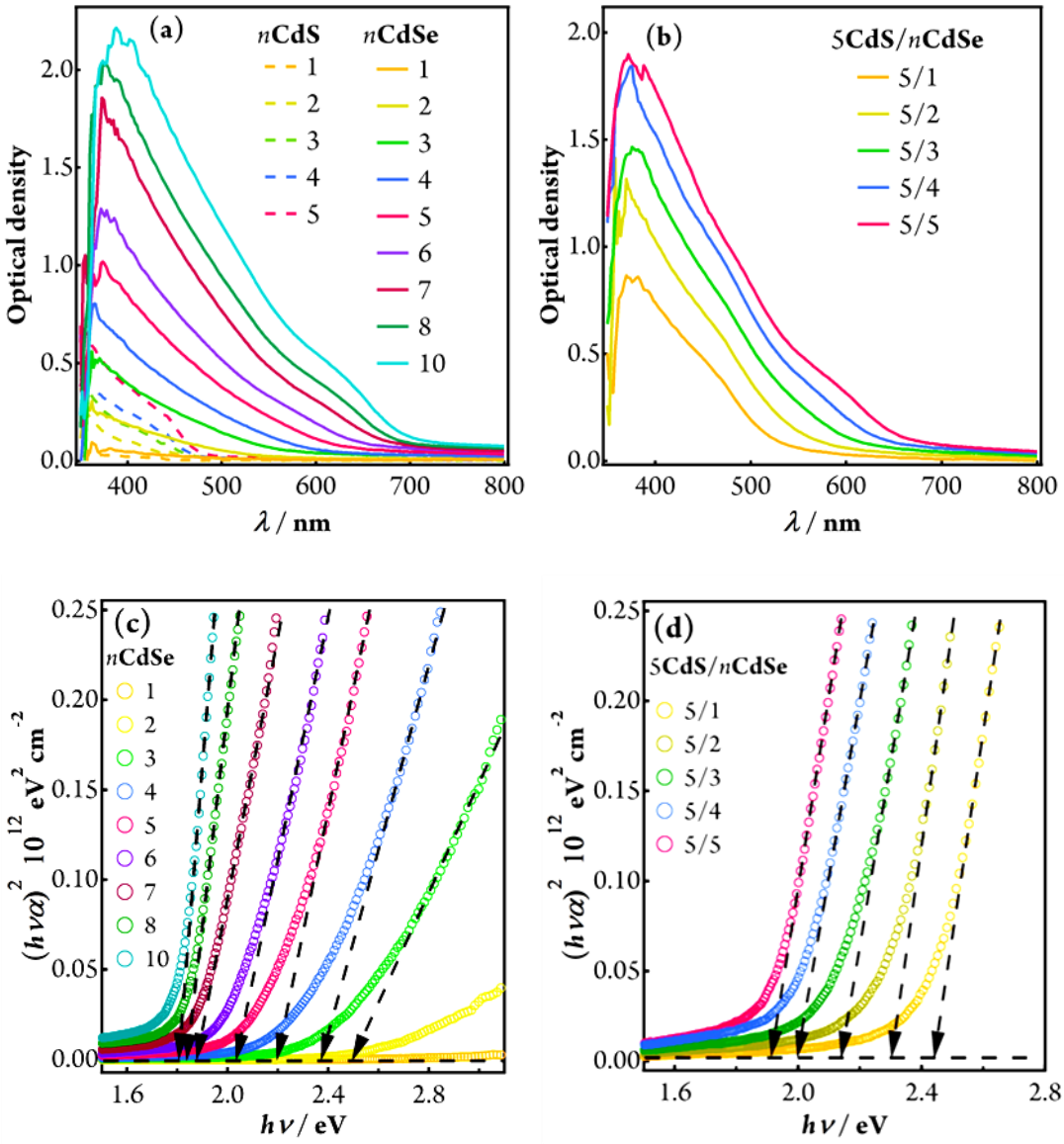

Figure. 3 UV-vis optical density (OD) spectra of as-prepared (a) *n*CdS and *n*CdSe, and (b) 5CdS/*n*CdSe-coated 2.4 μm TiO_2 electrodes, where *n* is the number of SILAR deposition cycles. The OD spectra represent the net light absorption by the sensitizers as the substrate absorption (mesoporous TiO_2) was subtracted from the absorption spectra of corresponding *n*CdS, *n*CdSe and 5CdS/*n*CdSe-sensitized TiO_2 electrodes. Tauc plots of (c) *n*CdSe-coated TiO_2 electrodes, and (d) 5CdS/*n*CdSe-sensitized TiO_2 electrodes.

It should be noted here that, to achieve an identical absorbance the deposition cycle "*n*" may vary with the actual deposition conditions, such as concentration and volume of precursor solutions, solvents, duration for reaction and rinsing steps, size of electrodes, temperature, *etc.* In the present study, as 5CdS/5CdSe was found to be the best-performed cascade-structured sensitizer, it was then chosen for other

characterizations and compared with the CdSe.

As more CdSe layers are deposited, a characteristic hump appears in the spectra of 5CdS/*n*CdSe between 500 and 700 nm and shifts to longer wavelengths with increasing deposition cycles (Fig. 3.3(b)). Interestingly, these humps are missing in the spectra of *n*CdSe alone for the same deposition cycles (Fig. 3.3(a), n = 1-5), for which the peak absorbance is much lower and the onsets are greatly blue shifted compared to that of 5CdS/*n*CdSe. Ning *et al.* recently demonstrated enhanced light absorption from a type-II heterojunction interface when core-shell ZnSe/CdS quantum dots were used as sensitizer for TiO_2, where the absorption onset is changed to longer wavelength due to the narrowing of the effective band gap as a result of the interfacial optical transitions from the valence band maximum of ZnSe to the conduction band minimum of CdS at the heterojunction interface.[83]

Although the junction of CdS/CdSe on TiO_2 was reported to be type-II based on ultraviolet photoelectron spectroscopy (UPS) measurements,[19] the significant absorption hump here seems unlikely to originate from the CdS/CdSe heterojunction interface considering the small absorption cross-section. In addition, as shown in Figure 3.3(a), CdSe alone exhibits such characteristic humps as well when more material was deposited by increasing SILAR deposition cycles to $n \geq 6$. So, the long wavelength hump and the enhanced light absorption for cascaded CdS/CdSe at any given number of SILAR cycles is very likely a result of more CdSe being deposited. This is supported by the previous reports that the nucleation and growth of CdSe on TiO_2 can be greatly accelerated with a CdS underlayer,[35,78] where CdS is rather a promoter for the preferential growth of CdSe. Consequently, a larger amount of CdSe was actually deposited with a 5-cycle deposition, effectively reaching the OD of CdSe

deposited on bare TiO_2 by 7 cycles (Fig. 3.3(a) and inset of Fig. 3.4(a)). The stacking of absorption spectra observed beyond 700 nm is believed to be caused by light scattering effects, which systematically increase with deposition cycles.[48,78]

To estimate the effective band gap of these sensitized electrodes, the above absorption spectra were presented in Tauc plots (Fig. 3.3(c, d)).[67] With increasing SILAR deposition cycles, the intersection of the base line with the tangent line of the linear region of the plots shifts towards lower energy, indicating the effective band gap of the deposited semiconductor sensitizer becomes narrower. The Tauc plot shows that both 7CdSe and 5CdS/CdSe electrodes possess an effective band gap of ~1.9 eV, further implying the identical optical properties of the two electrodes.

3.4 Photovoltaic characteristics

To investigate the photovoltaic performance of CdSe and CdS/CdSe–sensitized mesoscopic TiO_2 electrodes, sandwich type thin layer cells were fabricated with Cu_2S as the counter electrode, and a S^{2-}/S_x^{2-} electrolyte as the hole transporter. To ensure the CdSe sensitizer alone has identical OD to that of cascaded CdS/CdSe, 7 cycles of CdSe were deposited which presents approximately the same OD over the whole wavelength range as the most optimized 5CdS/5CdSe (inset of Fig. 3.4(a)). Scattering layers were not used for the 7CdSe and 5CdS/CdSe electrodes here in order to avoid the comparison between different photoanode structures and to simplify the interpretation of impedance data.

A thin ZnS passivation layer (2 cycles) was deposited onto the CdSe and CdS/CdSe-sensitized electrodes to hinder the backward electron flow from sensitizers to the oxidized species in S^{2-}/S_x^{2-} electrolyte.[49,50,78]

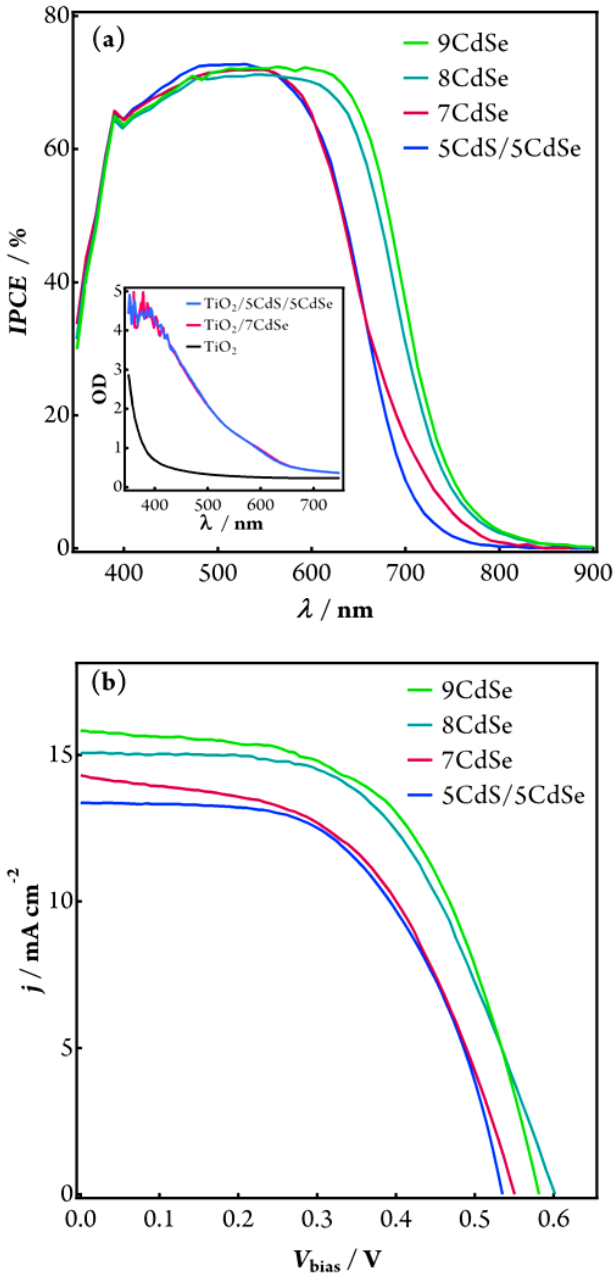

Figure 3. 4 IPCE spectra (a) and *j-V* characteristics (b) of cells made with 7CdSe and 5CdS/5CdSe-sensitized 5 μm thick TiO_2 electrodes without scattering layers, and the 8CdSe, 9CdSe-sensitized TiO_2 electrodes consisting of 5 μm P25 transparent layer and 4 μm thick scattering layers. The inset of figure (a) shows the OD spectra of 7CdSe and 5CdS/5CdSe-sensitized TiO_2 electrodes. Cu_2S on brass and S^{2-}/S_x^{2-} were used as the counter electrode and electrolyte, respectively.

The IPCE spectra of both CdSe and CdS/CdSe-sensitized TiO_2 solar cells exhibit strong photoelectrochemical response over the entire visible light range, with photon

wavelengths even extending to ~800 nm. As shown in the IPCE spectra of Figure 3.4(a), both electrodes exhibit identical external quantum efficiency of ~75% between 400 and 600 nm, while the CdSe-sensitized electrode presents much superior IPCE at longer wavelengths (>650 nm), contributing to the improvement of photocurrent.

Table 3.1 summarizes the device data using 5CdS/5CdSe and 7CdSe electrodes with identical OD and the optimized 8CdSe and 9CdSe electrodes incorporating a light scattering layer. It is clear that CdSe-sensitized TiO_2 electrodes demonstrate better photocurrent and photovoltage in *j-V* measurements, where a power conversion efficiency of 4.1% was attained under simulated AM 1.5 100 mW cm^{-2} illumination when no scattering layer was employed. In contrast, the cell performance is slightly impaired when CdS is used as an underlayer in cascaded CdS/CdSe electrodes, despite the identical light absorption. The presence of a scattering layer greatly promotes the IPCE of 9CdSe-sensitized TiO_2 cells in the long wavelength region, which leads to a power conversion efficiency of 5.21% under AM 1.5 100 mW cm^{-2} illumination, one of the highest cell efficiencies achieved so far for liquid junction SSCs.

Table 3. 1 Characteristics of CdSe and CdS/CdSe-sensitized TiO_2 solar cells with Cu_2S as counter electrode under simulated AM 1.5 100 mW cm^{-2} illumination.

Photoanode	*Sensitizer*	V_{oc} *(V)*	j_{sc} *(mA* cm^{-2}*)*	*ff (%)*	η [a] *(%)*
TiO_2	7CdSe	0.548	14.27	52.36	4.10 ± 0.14
	5CdS/5CdSe	0.535	13.35	56.26	4.02 ± 0.11
TiO_2/scattering	8CdSe	0.600	15.06	55.05	4.97 ± 0.17
layer	9CdSe	0.579	15.77	56.95	5.21 ± 0.10

[a] The sample standard deviation of cell efficiency is based on the data of the best three cells.

Table 3. 2 *j-V* characteristics of cascaded CdS/CdSe-sensitized 5 µm thick TiO_2 (without scattering layers) solar cells made with different number of CdS and CdSe deposition cycles for optimization incorporating platinized FTO cathode under simulated AM 1.5 100 mW cm^{-2} illumination.

Photoanode	*Sensitizer*	V_{oc} *(V)*	j_{sc} *(mA.cm^{-2})*	*ff (%)*	*η (%)*
TiO_2	4CdS/5CdSe	0.560	12.14	42.95	2.92
	4CdS/6CdSe	0.556	11.59	46.01	2.96
	5CdS/5CdSe	0.563	12.70	41.76	3.00
	5CdS/6CdSe	0.548	12.82	41.90	2.94
	5CdS/7CdSe	0.545	12.92	40.53	2.85

In order to investigate the charge transport characteristics in cells, platinized FTO cathodes were used to make stable devices required for impedance spectroscopy measurement. Figure 3.5 and Table 3.3 show the *j-V* characteristics of those cells used for IS measurement. It is also observed that the 7CdSe performs better than the optimized 5CdS/5CdSe electrodes irrespective of TiO_2 film thickness (5 and 10.3 µm thick without scattering layers). The *j-V* curves (Fig. 3.5) show that the V_{oc} of the cells made with 7CdSe photoanode is higher than that of 5CdS/5CdSe electrodes of identical OD. In addition, this V_{oc} difference becomes even pronounced if thicker TiO_2 electrode (10.3 µm) is used which often happens because of increased dark current with film thickness.

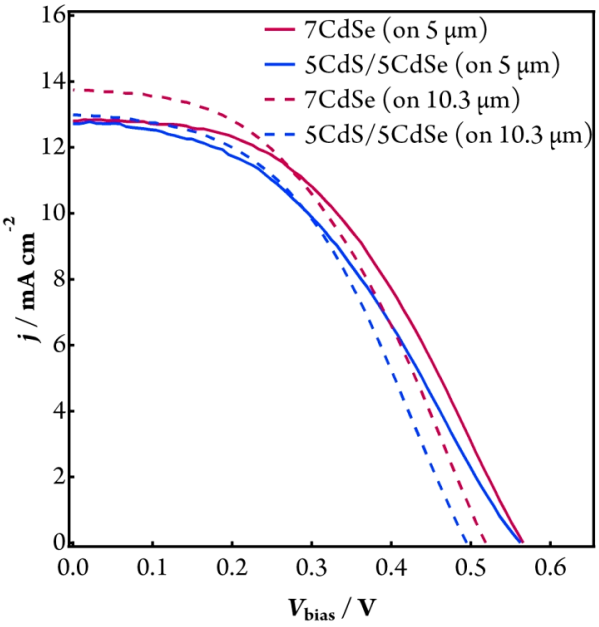

Figure 3. 5 *j-V* characteristics of solar cells used for IS measurement. The cells were made with 7CdSe and 5CdS/5CdSe-sensitized TiO_2 photoanodes (5 and 10.3 μm thick TiO_2 electrodes without scattering layers) and platinized FTO cathode.

Table 3. 3 Characteristics of 7CdSe and 5CdS/5CdSe-sensitized TiO_2 solar cells for IS measurement (TiO_2 electrodes were 5 and 10.3 μm thick without scattering layers) made with platinized FTO cathode under simulated AM 1.5 100 mW cm^{-2} illumination.

Thickness of TiO_2 (μm)	*Sensitizer*	*V_{oc} (V)*	*j_{sc} ($mA.cm^{-2}$)*	*ff (%)*	*η (%)*
5	7CdSe	0.568	12.80	45.71	3.32
5	5CdS/5CdSe	0.563	12.70	41.76	3.00
10.3	7CdSe	0.521	13.70	44.60	3.18
10.3	5CdS/5CdSe	0.496	12.94	45.90	2.95

3.5 Charge collection and separation in CdSe-sensitized TiO_2 solar cells

3.5.1 Investigation of charge transport and recombination processes using impedance spectroscopy

Impedance spectroscopy (IS) measurements of the cells (using platinized FTO counter electrode for improved stability) were performed to further investigate the role of the CdS underlayer. Figure 3.6 shows the equivalent circuit used for analysis of impedance spectra. Here R_s is the series resistance associated with the FTO substrate, external connections and load, R_t is the charge transport resistance in TiO_2, R_{ct} is the charge transfer resistance at photoanode/electrolyte interface, C_μ is the chemical capacitance of TiO_2, C_{sub} is the substrate capacitance, r_t is the distributed transport resistance of electrons in TiO_2, c_μ is the distributed chemical capacitance of the oxide layer, r_{ct} is the distributed charge transfer resistance at photoanode/electrolyte interface, Z_d is a Warburg impedance of diffusion of redox species in the electrolyte, R_{Pt} is the charge transfer resistance at the platinized FTO cathode/electrolyte interface and C_{Pt} is the corresponding double layer capacitance. These lower case resistances and capacitances (distributed parameters of the transmission line model),[84,85] are related to total resistances and capacitances by $r_t = R_tA/d$, $r_{ct} = R_{ct}Ad$, and $c_\mu = C_\mu/(Ad)$ where, d and A are the thickness and projected area of TiO_2 electrode.

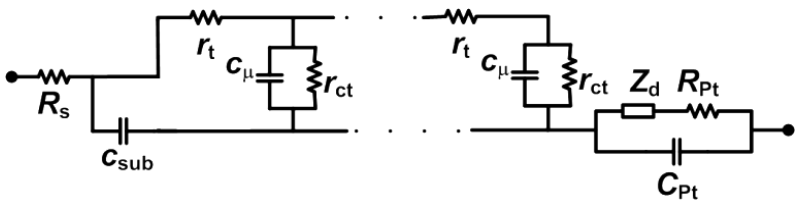

Figure 3. 6 Equivalent circuit used for fitting impedance spectra of mesoscopic TiO_2 and SnO_2-based solar cells.

TiO_2 electrodes of thickness 5 and 10.3 μm were used to make solar cells for IS measurements; therefore, the obtained parameters R_{ct}, R_t, and C_μ from the fitting results were normalized to the film thickness and the projected cell area. The units for the distributed parameters r_t, r_{ct}, and c_μ are Ω cm, Ω cm^3, and F cm^{-3}, respectively. Bisquert has shown that the effective electron diffusion length (L_n) can be determined by R_{ct} and R_t as follows:

$$L_n = d\sqrt{\frac{R_{ct}}{R_t}}$$

Good fits to most impedance spectra (Fig. 3.7(a, b)) of cells made with photoanodes of identical OD could be obtained using an equivalent circuit based upon the diffusion-reaction model for porous electrodes shown in Figure 3.6.[84] As shown in Figure 3.7 (d), while the c_μ-V_{oc} plots for both cells are nearly identical within a wide range of bias voltage, r_{ct} for the cell with a 7CdSe electrode is ~2 times higher than for the cell with a 5CdS/5CdSe electrode at the same quasi-Fermi level, indicating that the presence of CdS underlayer in 5CdS/5CdSe cells promoted the backward interfacial charge transfer (Fig. 3.7(c)). As a consequence, the V_{oc} of 5CdS/5CdSe cell is slightly lower than that of 7CdSe cell. The accelerated recombination could arise from the presence of trap states introduced by the CdS buffer layer in between TiO_2 and CdSe, which is plausible because of the extra interface in the CdS/CdSe-sensitized TiO_2 electrode compared to the CdSe electrode.

Hod *et al.* have recently reported that the chemical capacitance of semiconductor-sensitized TiO_2 measured by impedance spectroscopy is a combination of localized states in both TiO_2 and semiconductor sensitizer, which are indistinguishable and represent a single entity.[86] If this were the case, the detailed recombination

mechanism for electrodes using a CdS buffer layer would be very complex. Unambiguous interpretation of the origins of the trap states and their roles in charge recombination would require systematic investigation of different electrode configurations.

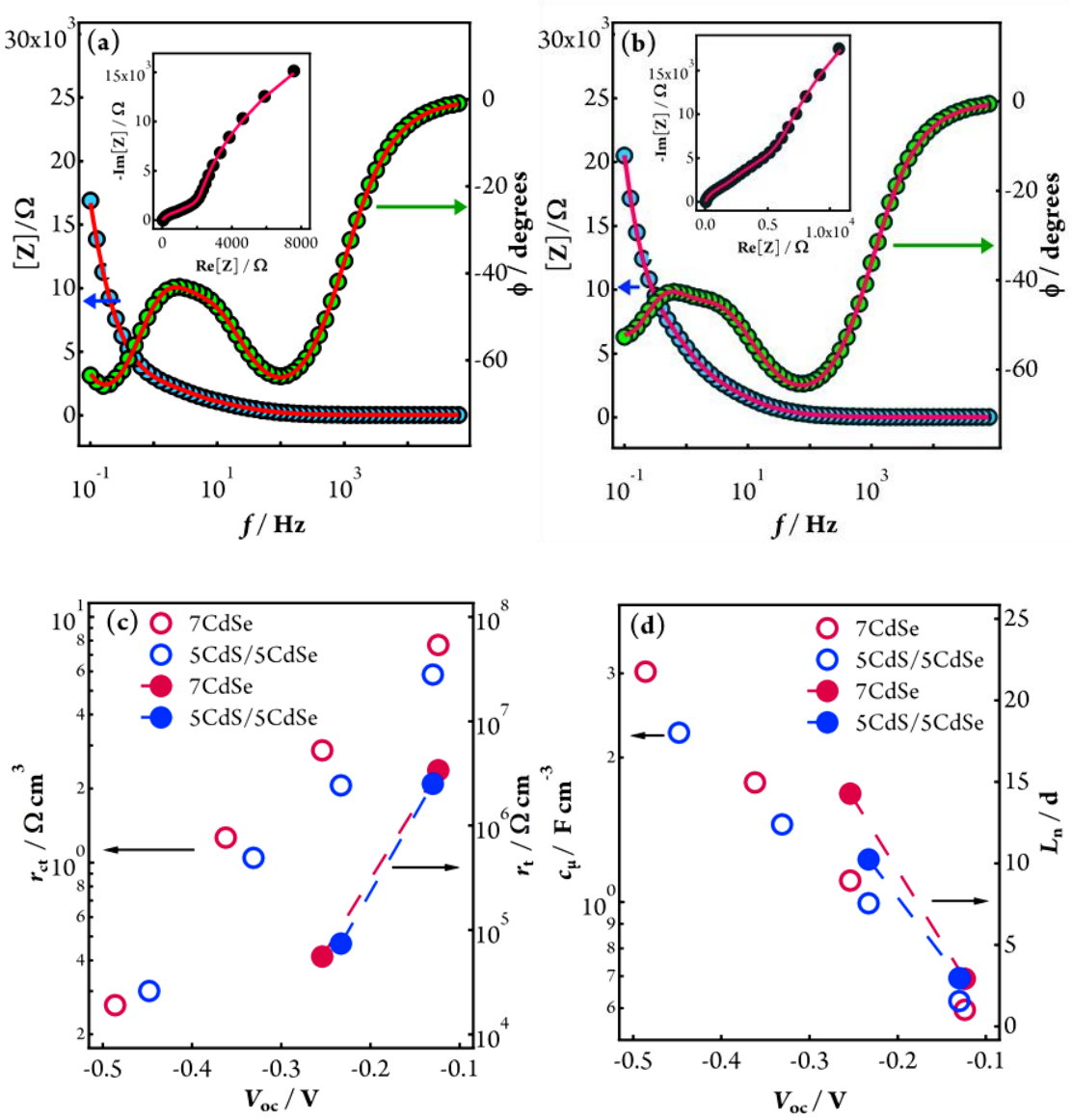

Figure 3. 7 Bode and Nyquist plots showing typical IS results (circle) and best fits using the diffusion-reaction model (solid red lines) for SSCs utilizing (a) 7CdSe- and (b) 5CdS/5CdSe-sensitized 5 μm TiO_2 electrodes and platinized FTO cathodes. (c) Dependence of distributed charge transfer resistance (r_{ct}), electron transport resistance (r_t) and (d) chemical capacitance (c_μ) and electron diffusion length divided by the TiO_2 film thickness (L_n/d) on open circuit photovoltage (V_{oc}) of the corresponding cells. The *j*-*V* performances of these cells are shown in Table 3.3.

In addition, we note that the 627 nm light used in the impedance measurement will not directly excite the CdS in CdS/CdSe electrodes, which intuitively would hinder charge separation under the illumination conditions. However, if CdS simply acts as a barrier between the TiO_2 and the CdSe and/or the electrolyte, then recombination would be suppressed. In fact, an opposite result in the recombination resistance was observed here as derived by the impedance measurements, further supporting the above conclusions.

A Warburg impedance representing finite length electron diffusion in TiO_2 can be clearly observed in the IS spectra in the photovoltage range of 0.1–0.3 V. As shown in Figure 3.7(c), in contrast to recombination the fitted electron transport impedances of both CdSe and CdS/CdSe-sensitized TiO_2 electrodes are fairly comparable. The corresponding electron diffusion lengths (L_n) are then determined which is at least 2 times greater than the TiO_2 film thickness, sufficient to ensure unity charge collection in both cells (Fig. 3.7(d)).[48] Similar results were also found for devices made with 7CdSe and 5CdS/5CdSe-sensitized 10.3 μm thick TiO_2 electrodes (Fig. 3.8).

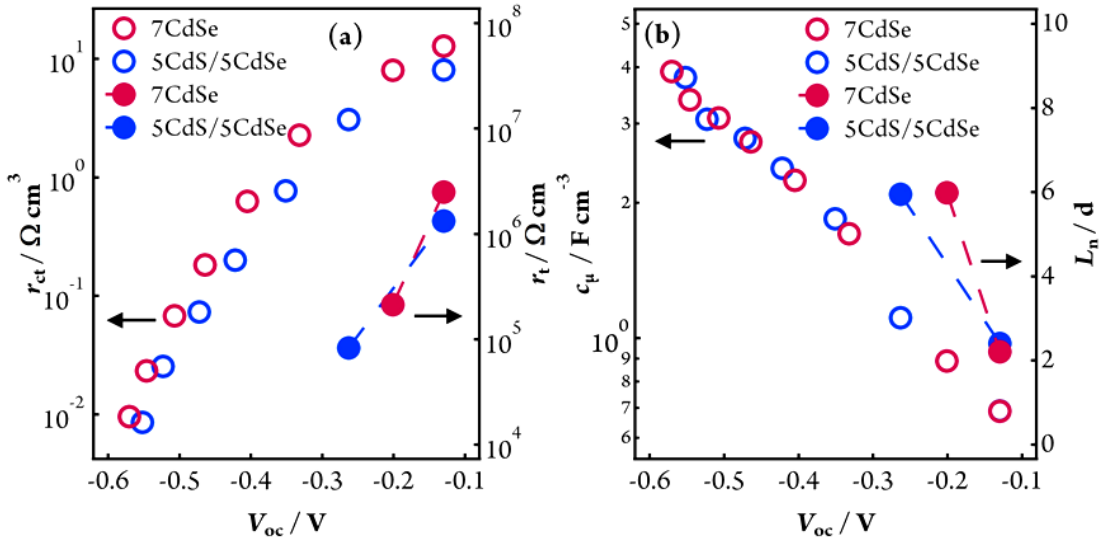

Figure 3. 8 Dependence of distributed charge transfer resistance (r_{ct}), electron transport resistance (r_t) (a) and chemical capacitance (c_μ) and electron diffusion length divided by film thickness (L_n/d) (b) versus V_{oc} for SSCs utilizing 7CdSe and 5CdS/5CdSe-sensitized 10.3 μm TiO_2 electrodes (without scattering layers) and platinized FTO cathodes.

3.5.2 Estimation of electron injection efficiency

The reliable determination of effective diffusion length of electrons in the sensitized electrode allows for rigorous evaluation of charge separation efficiency in both cells. The IPCE of SSCs can be conceptually factored into three parts as the equation shown in Section 2.9 in Chapter 2. Among these, the charge separation efficiency, $\eta_{\mathrm{sep}}(\lambda)$ depends on the carrier injection efficiency, $\eta_{\mathrm{inj}}(\lambda)$ and the sensitizer regeneration efficiency, $\eta_{\mathrm{reg}}(\lambda)$. The diffusion length of electrons was found to be at least two times the TiO_2 film thickness at all voltages from IS measurements, which implies a near unity charge collection efficiency ($\eta_{\mathrm{col}}(\lambda)$). The light harvesting efficiency ($\eta_{\mathrm{lh}}(\lambda)$) was estimated from the optical density (OD) spectra of the electrodes. Then the IPCE spectra can be simulated utilizing the OD spectra of the corresponding photoelectrodes by varying the charge separation efficiency to match the actual IPCE spectra (Fig. 3.9). In the simulation, a correction for electrolyte absorption (aqueous S^{2-}/S_x^{2-} electrolyte) at short wavelengths was also made, while a porosity of 0.5 of the TiO_2 electrodes for electrolyte penetration was used and the charge separation (electron injection/hole scavenging) yield was allowed to vary to obtain a good fit. The $\eta_{\mathrm{reg}}(\lambda)$ is believed to be unity because of large driving force (energy difference between HOMO of sensitizers and E_{redox} of S^{2-}/S_x^{2-} electrolyte) for sensitizer regeneration along with the good ionic strength of S^{2-}/S_x^{2-} electrolyte; thus the varied yield in Figure 3.9 was believed to be only $\eta_{\mathrm{inj}}(\lambda)$.

As shown in Figure 3.9, the simulated IPCE spectra only match at shorter wavelengths, which give an average electron injection efficiency of ~88% for both electrodes. At longer wavelengths disagreement between simulation and experiment

arises due to uncorrected light scattering by the photoanodes. It is interesting to note in a recent study by Lin *et al.*, that faster charge transfer from CdS/CdSe to TiO_2 was observed when compared with that of CdSe/CdS-sensitized electrodes (CdSe is deposited in between CdS and TiO_2).[82] However, since the obtained charge separation efficiency for both cells is quite similar at short wavelengths, no evidence was found here that the presence of CdS buffer layer could favourably facilitate charge separation as compared to the CdSe-sensitized electrodes.

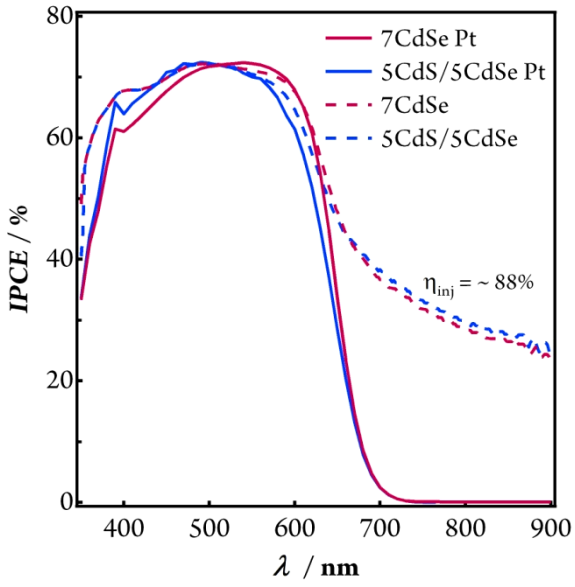

Figure 3. 9 IPCE spectra of 7CdSe and 5CdS/5CdSe cells made with platinized cathode (solid lines) and the simulated IPCE spectra based on the light absorption spectra of 7CdSe and 5CdS/5CdSe-sensitized thin (2.4 μm) TiO_2 electrodes (dashed lines).

Although the influence of sensitizer configuration on IPCE was not evidently observed at short wavelengths, the enhanced external quantum efficiency of CdSe cells at longer wavelengths (>650 nm, Fig. 3.4(a)) clearly infers that CdSe-sensitized TiO_2 possess superior charge extraction capability to that of CdS/CdSe cells for the charge carriers generated by low energy photons. Considering that both cells have

unity charge collection and nearly identical light harvesting, the enhanced IPCE of 7CdSe at longer wavelengths would only be a result of facilitated charge separation, while it is deteriorated by the presence of CdS interlayer. Since sensitizer regeneration has no significant wavelength dependence, the enhancement of charge separation could be further attributed to facilitated charge injection from CdSe to TiO_2, which is however impeded in the presence of CdS buffer layer.

3.6 Band alignment of the CdS/CdSe and CdSe-sensitized TiO_2 electrodes

To understand the wavelength-dependent charge injection arisen from different electrode configurations, it is speculated that a type-I band alignment was formed between CdS and CdSe on TiO_2 as illustrated in Figure 3.10(a). While it is pertinent to note that UPS measurement has indicated a type-II junction between CdS and CdSe when deposited on TiO_2,[19] a type-I band alignment is not impossible considering the inhomogeneous deposition of CdSe on CdS, where the preferential growth of CdSe would lead to a significant shrinkage of the band gap and consequently downward shift of the conduction band. Actually such situation is not rare and the formation of type-I band alignment between CdS and CdSe has been reported in core-shell quantum dot hetero-structures.[87-89] As a result, the relative band position displacement of CdS and CdSe may give rise to a straddled band alignment with the conduction band minimum of CdSe lower while valance band maximum higher than that of CdS. As such, while hot electrons generated in CdSe by short wavelength photons (hv_1) are still energetically favorable to transfer into TiO_2 through the conduction band of CdS layer, those generated by long wavelength photons (hv_2) might be hindered in presence of the CdS buffer layer as an energy barrier in between CdSe and TiO_2.[90] In

contrast, charge carriers generated by these long wavelength photons would viably be injected into TiO_2 in CdSe cells, as shown in Figure 3.10(b).

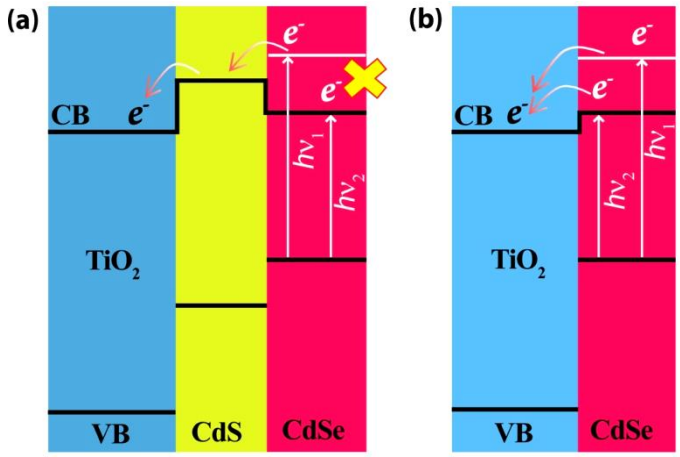

Figure 3. 10 Speculated band alignment of (a) CdS/CdSe and (b) CdSe-sensitized TiO_2 prepared by SILAR method. The type-I band alignment between CdS and CdSe could be caused by the inhomogeneous deposition of the light absorbing layers on TiO_2. CdSe excited by short wavelength ($h\nu_1$) and long wavelength ($h\nu_2$) photons shows different charge injection, contingent to electrode configurations.

At the end of this study, it is worthwhile to mention the recent work by Pan *et al.*,[12] who demonstrated an efficiency of 5.32% utilizing an inverted type-I core-shell CdS/CdSe QDs-sensitized TiO_2 electrode, where TiO_2 and CdS were separated by the CdSe. This reverse configuration is somewhat supportive to the above argument. Very recently, they showed a record efficiency of 5.42% using only MPA caped CdSe QDs on TiO_2 electrode which made our argument even stronger.[14]

3.7 Summary

From the above comprehensive study it is concluded that CdSe-sensitized TiO_2 solar cells possess noticeably slower charge recombination at the TiO_2/CdSe interface, and much enhanced light harvesting of long wavelength photons, giving rise

to superior overall device performance to the cascaded CdS/CdSe cells. These findings lead to the important conclusion that while the CdS buffer layer might still be indispensable in some kinds of SSCs,[91,92] it is actually redundant and even causes efficiency losses in CdSe-sensitized TiO_2 solar cells. We anticipate that with the discoveries presented in this study, the performance of semiconductor-sensitized mesoscopic solar cells could be further promoted by rigorous interfacial engineering to improve charge separation and mitigate charge recombination.

4 Ternary Solid Solution CdS_xSe_{1-x}-Sensitized Mesoscopic TiO_2 Solar Cells

4.1 Introduction

To facilitate charge separation in mesoscopic semiconductor-sensitized photoelectrochemical cells, a type-II band alignment between semiconductor sensitizer and metal oxide (*i.e.* TiO_2) is highly desired, where both the conduction and valence bands of the sensitizer are higher in energy than the corresponding band energies of the underlying metal oxide, so that the generated electrons and holes in the sensitizer separate rapidly by transferring electrons into the conduction band of the metal oxide. As a result, the conduction band position, and hence the size, of semiconductor sensitizers is critical to achieve efficient charge separation. As reviewed in Section 3.1 in Chapter 3, although CdSe is the most widely investigated light absorber in SSCs owing to its superior optical and electrical properties,[15,45,63,69,70,78] only small CdSe nanocrystals with sufficiently high conduction band energy relative to that of TiO_2 meet this requirement according to ultrafast transient optical measurements.[90,93] However, to synthesize quantum sized CdSe, except the CBD method, complex and cumbersome synthetic protocols have to be adopted.

On the other hand, while SILAR offers great flexibility for depositing various semiconductor sensitizers on mesoporous TiO_2 directly, it lacks precise control of the growth of CdSe sensitizer and polydispersed CdSe is usually obtained as described in Section 2.4.1 in Chapter 2. In addition, compositional synthesis has been emerging as

a promising approach to tune the optical and energetic properties of semiconductor sensitizers while keeping the particle size constant, where the optical band gap and the associated band edge position can feasibly be varied by changing the composition of the semiconductor sensitizers. Hence, instead of synthesizing CdSe QDs with reduced size, an alternative approach is to utilize a solid solution of CdSe formed with another wider band gap material, for instance CdS, which leads to the formation of cadmium sulfoselenide (CdS_xSe_{1-x}).

CdS_xSe_{1-x} is a member of the ternary chalcogenide compounds, which have recently attracted great attention for their potential application in photovoltaic devices.[94-96] Owing to the small lattice mismatch (~3.9%), CdS and CdSe are miscible over a wide range of compositions, which leads to the formation of CdS_xSe_{1-x} ($0 \leq x \leq 1$) solid solution with almost zero enthalpy change $\Delta H_{mix} \approx 0$, close to the ideal mixing condition.[97] CdS_xSe_{1-x} with controlled composition has been successfully prepared by mixing both the hexagonal wurtzite CdS and CdSe crystals in a thermal vapour transport system, or by mixing their precursors in a stoichiometric ratio in a solution method such as hot injection, to control the composition of CdS_xSe_{1-x} and hence engineer its band gap in between the bulk CdSe (1.75 eV) and CdS (2.5 eV).[94,98-102]

Nanocrystalline CdS_xSe_{1-x} of different morphologies such as colloidal QDs,[103] thin film,[94] nanowire,[104], nanorod,[105] nanobelt,[106,107] *etc.*, have been extensively studied and demonstrated good photoluminescence quantum efficiency and enhanced photoconductivity and charge carrier dynamics, which are generally desired for photovoltaic applications.[102,108-111] While the optical and electrical properties have been extensively investigated, the use of CdS_xSe_{1-x} as sensitizer in SSCs has rarely

been reported. Recently, Kang *et al.* prepared conformal coating of crystalline CdS_xSe_{1-x} solid solution on Nb_2O_5 nanowires by thermal chemical vapour transport of CdS and CdSe powders and they used these electrodes for photocurrent and hydrogen generation rates in a photoelectrochemical cells, which shows that these can be used as a photoanode in SSCs.[112]

More recently, Shu *et al.* also prepared CdS_xSe_{1-x} by SILAR using $Na_2Se_xS_{1-x}$ and $Cd(NO_3)_2$ in methanol as anionic and cationic precursors solution, respectively.[96] They made the methanol solution of $Na_2Se_xS_{1-x}$ by dissolving elemental selenium (Se) and Na_2S in methanol at various ratios to modulate the concentration of Se^{2-} and S^{2-} ions in the anionic precursor solution for the SILAR method. Their reported efficiency of CdS_xSe_{1-x}-sensitized TiO_2 cells made with platinum counter electrode and with an electrolyte comprised of 2 M Na_2S, 0.5 M S and 0.2 M KCl in water/methanol (7/3, v/v) was 2.27%. However, after depositing a few layers of CdSe on the CdS_xSe_{1-x}-sensitized TiO_2 electrodes by SILAR method, an efficiency of 3.17% was reached, which implies that there is much room for the improvement of cell performance by using more catalytic counter electrodes for the S^{2-}/S_x^{2-} electrolyte (*i.e.* CoS, Cu_2S *etc.*).[96]

Herein we present a comprehensive study on CdS_xSe_{1-x}–sensitized mesoscopic TiO_2 solar cells and their comparison with the widely-used cascaded CdS/CdSe sensitizer.[18,45,63,78,81,113] In addition, instead of using the high-temperature thermal vapour transport or hot injection methods, SILAR was employed to facilely prepare CdS_xSe_{1-x} by alternately depositing layers of CdS and CdSe directly onto mesoscopic TiO_2 electrodes. The electron microscopy and X-ray diffraction study of as-grown sensitizers on TiO_2 were carried out to understand their structure and morphology.

Optical characterization, *j-V* characteristics, IPCE and electrochemical impedance spectroscopy were combined to understand the separation and collection of charge carriers in this SSC. Using this newly synthesized CdS_xSe_{1-x} solid solution sensitizer, a power conversion efficiency of 4.05% has been achieved under simulated AM 1.5 100 $mWcm^{-2}$ illumination, which may rival that of the commonly used cascaded CdS/CdSe sensitizer.

4.2 Morphology of CdS_xSe_{1-x}-sensitized TiO_2

CdS_xSe_{1-x}-sensitized TiO_2 electrodes were prepared by alternate deposition of CdS and CdSe by SILAR as discussed in Section 2.3.2 in Chapter 2. Figure 4.1(a) shows a HRTEM image of the as-grown solid solution CdS_xSe_{1-x} on ~25 nm sized TiO_2 crystal grains after 6 cycles of SILAR deposition (denoted as $6CdS_xSe_{1-x}$). For comparison, the cascaded 5CdS/5CdSe (the best performing sensitizer of the analogue) prepared from the same batch of precursor solution was also measured (Fig. 4.1(b)). It is evident that, while the lattice fringes of the TiO_2 crystal grains are clearly seen, their surface is covered with a layer of 4~5 nm thick amorphous material after the SILAR deposition, which is presumably the deposited solid solution $6CdS_xSe_{1-x}$ or 5CdS/5CdSe.

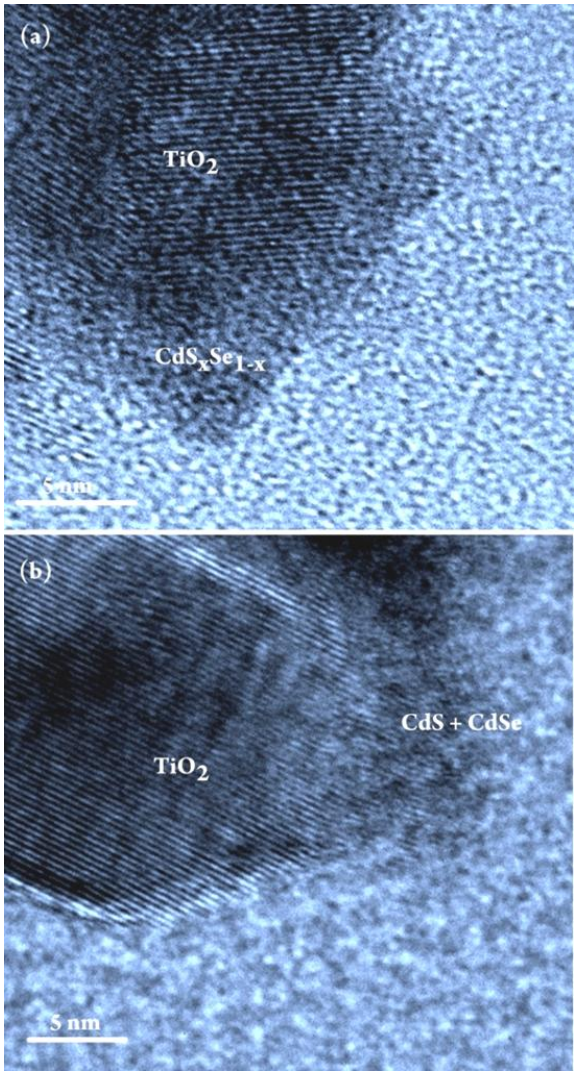

Figure 4. 1 HRTEM images of (a) solid solution $6CdS_xSe_{1-x}$ and (b) cascaded 5CdS/5CdSe deposited on TiO_2 nanoparticles (Degussa, P25).

The compositions of the as–prepared sensitizers were determined by EDS elemental analysis, which yielded an atomic ratio Cd/(S+Se) of 0.90 for $6CdS_xSe_{1-x}$ and 0.98 for 5CdS/5CdSe, indicating that on average the solid solution was slightly cadmium poor, while the cascaded layers were almost stoichiometric. From the EDS elemental analysis the calculated formula of the solid solution was found to be $Cd_{0.9}S_{0.42}Se_{0.58}$ in terms of the atomic ratio Se/S = 1.403, which is very close to the hexagonal $CdS_{0.42}Se_{0.58}$ (JCPDS No. 50-0720). It is anticipated that the composition

of CdS_xSe_{1-x} can feasibly be tuned by controlling the deposition parameters, such as concentration of precursor solution, solvent, duration for reaction and rinsing steps, and temperature, *etc.*, with which the optical and electrical properties of CdS_xSe_{1-x} will then be easily modulated.

4.3 Structural investigation on CdS_xSe_{1-x} sensitized TiO_2

Figure 4.2 shows the XRD patterns of $6Cd_{0.9}S_{0.42}Se_{0.58}$-sensitized TiO_2 electrodes before and after heat-treatment. The XRD patterns of heat-treated CdS and CdSe were also collected for comparison. The XRD pattern of $Cd_{0.9}S_{0.42}Se_{0.58}$-sensitized TiO_2 shows features only from TiO_2, indicating the as-grown solid solution is amorphous in nature. However, after heat treatment at 350 °C, broad peaks appear at 42.75° and 50.71°, implying crystallization of the amorphous phase (Fig. 4.2). The set of diffraction peaks is fairly close to those of individual CdSe and CdS — with the 2θ values slightly larger than for the former while smaller than for the latter.[94,108] The shift of the XRD peaks of CdS_xSe_{1-x} relative to those of CdS and CdSe indicates a decrease in the spacing of the crystal planes of CdS_xSe_{1-x} with respect to CdSe due to the incorporation of S^{2-} into the CdSe host lattice because of near ideal miscibility between these two materials and their intimate contact at mesoscopic level. In general, these results indicate a composition of the solid solution in between the two end compounds CdS and CdSe obtained by using a fixed precursor concentration during SILAR deposition, which is further confirmed by the distinct absorption spectrum from that of cascaded 5CdS/5CdSe in UV-vis light absorption measurement.

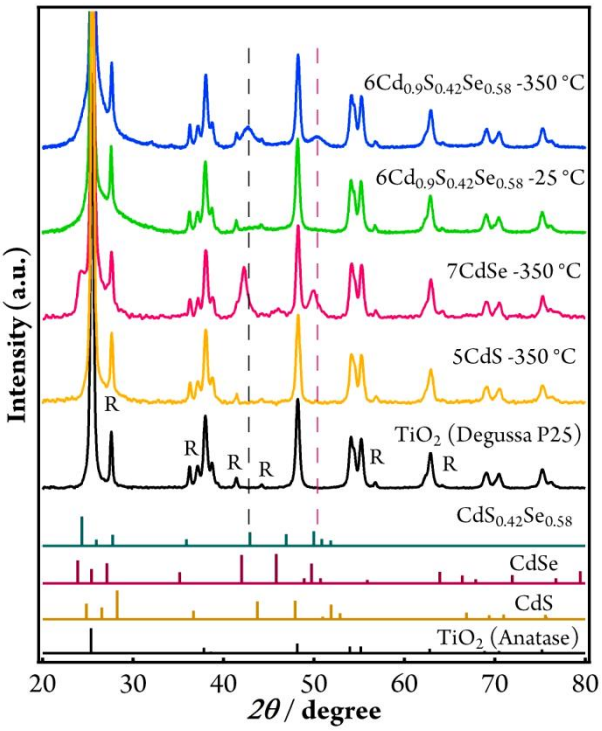

Figure 4. 2 XRD patterns of $6Cd_{0.9}S_{0.42}Se_{0.58}$, 5CdS/5CdSe, 7CdSe and 5CdS-sensitized TiO_2 electrodes made on microscope glass slides before and after heat treatment. The standard 2θ values for TiO_2 (anatase), rutile (R) phase in TiO_2 (Degussa, P25), wurtzite CdS, CdSe and $CdS_{0.42}Se_{0.58}$ crystals are also shown for comparison.

4.4 Optical properties of *n*CdS_xSe_{1-x}-sensitized TiO_2 electrodes

The OD spectra of *n*CdS, *n*CdSe, and *n*CdS_xSe_{1-x} (*n* = 1-8) sensitized TiO_2 electrodes are depicted in Figure 4.3. The thickness of the TiO_2 electrodes is 2.4 µm. With increasing deposition cycles, the absorption onsets of the *n*CdS and *n*CdSe-sensitized electrodes shift to longer wavelength due to reduction of size-induced electronic quantization of the band structure. Meanwhile, a characteristic absorption shoulder appears at around 550-650 nm in the CdSe-sensitized electrodes, which shifts gradually to longer wavelength with increasing SILAR deposition cycles as shown in Figure 4.3(a).

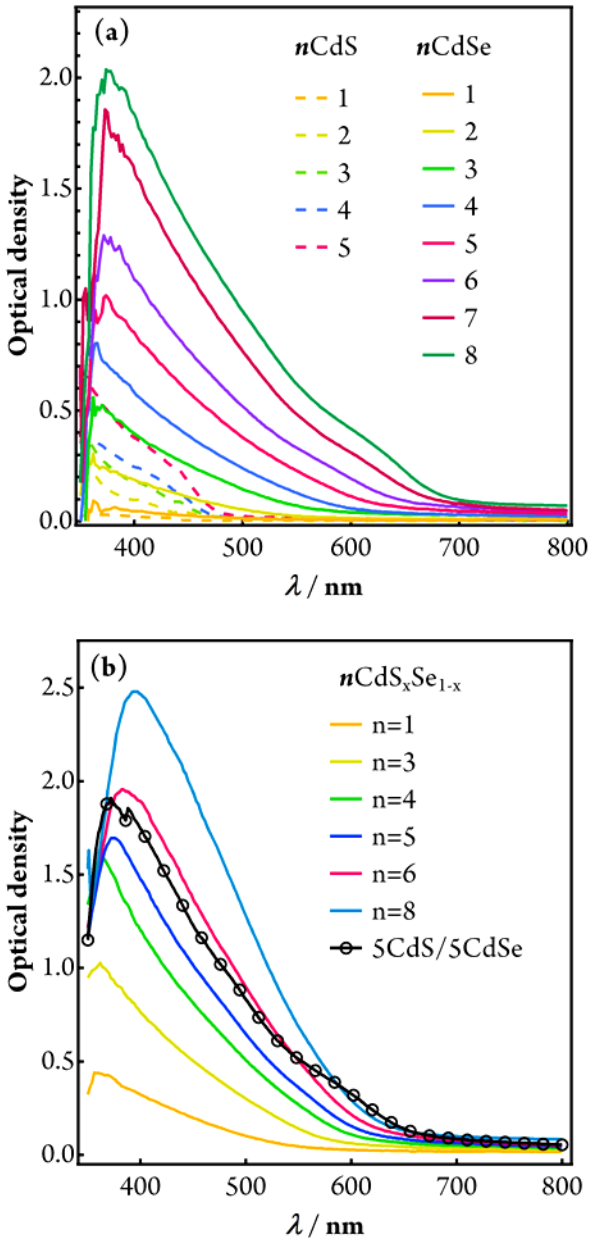

Figure 4. 3 UV-Vis spectra of individual (a) CdS, CdSe, and (b) solid solution $n CdS_xSe_{1-x}$-coated TiO_2 electrodes with different SILAR deposition cycles (n = 1-8). The spectrum of cascaded 5CdS/5CdSe-sensitized TiO_2 is also included in (b) for comparison.

Cascaded 5CdS/5CdSe-sensitized electrodes were also measured, and were found to exhibit similar characteristic absorption at ~600 nm due to the preferential growth of CdSe on pre-deposited CdS underlayer (solid black line with circular marks in Fig. 4.3(b)).[35,78] In contrast, these humps are missing in the spectra of $n CdS_xSe_{1-x}$-

sensitized TiO_2 electrodes, indicating the alternate deposition leads to the formation of solid solution, distinct from the cascaded 5CdS/5CdSe where both CdSe and CdS are separated phases. Similarly, the absorbance of CdS_xSe_{1-x} continuously increases with the number of alternate CdS and CdSe deposition cycles on TiO_2, while the shift of absorption onsets of these spectra (Fig. 4.3(b)) is less significant compared with that of CdSe in Figure 4.3(a).

In addition, the incorporation of S^{2-} in the resulting CdS_xSe_{1-x} gives rise to a significant blue shift of the spectrum as compared to that of pure CdSe for the same number of deposition cycles, which is also clearly revealed by the spectra of $5CdS_xSe_{1-x}$ and 5CdS/5CdSe in Figure 4.3(b). This indicates that the band gap of the CdSe-based light absorber can facilely be tuned by varying its composition by changing the deposition mode. In addition, 5CdS/5CdSe has slightly higher OD than that of the solid solution for the same deposition cycles ($5CdS_xSe_{1-x}$) over most of the wavelength range, while its absorbance becomes lower at wavelengths beyond 700 nm. The slightly higher OD of $n CdS_xSe_{1-x}$ at long wavelength becomes more apparent for n >5, which is believed to be partly due to increased light scattering. But as shown later by IPCE spectra, it also contributes to the light harvesting in SSCs.[45,78] To study their photoelectrochemical properties, these as-prepared electrodes were used directly for device fabrication and characterization in the subsequent sections.

4.5 Photovoltaic characterization

To investigate the photovoltaic performance of $n CdS_xSe_{1-x}$-sensitized mesoscopic TiO_2 electrodes (n = 6, 7 and 8), solar cells were fabricated with platinized FTO and Cu_2S on brass as the counter electrode, and an aqueous S^{2-}/S_x^{2-} electrolyte as the

hole transporter. To facilitate charge transport and prevent recombination at the TiO_2/sensitizer/electrolyte interfaces, TiO_2 electrodes were pre-treated with $TiCl_4$ aqueous solution prior to sensitizer deposition, and post-treated by depositing a thin passivation layer of ZnS onto the sensitized electrodes by SILAR.

As the IPCE spectra show in Figure 4.4(a), all the cells exhibit strong photo-response over the entire visible light range, with converted photon wavelengths even extending to ~900 nm. In comparison, while the CdS_xSe_{1-x} cells present identical IPCE of ~75% between 350 and 650 nm to that of 5CdS/5CdSe, with increasing deposition cycles enhanced quantum efficiency is observed with the CdS_xSe_{1-x} cells at longer wavelengths (> 700 nm), which is apparently consistent with the increased OD in Figure 4.3(b) and indicates that this is not solely caused by light losses arising from the direct transmission measurement geometry.

Figure 4.4(b) shows the *j-V* characteristics of these cells. The photocurrent generally increased with increasing SILAR deposition cycles but the overall cell performance declined as a result of inferior fill factor and V_{oc}. Among all the solid solution electrodes, cells made with $7CdS_xSe_{1-x}$ show the best performance, yielding j_{sc} = 14.96 mA cm^{-2}, V_{oc} = 0.526 V, fill factor = 51.40%, and η = 4.05% under simulated AM 1.5 100 mW cm^{-2} illumination as listed in Table 4.1. In comparison, cells made with the optimized cascaded 5CdS/5CdSe-sensitized electrode yielded j_{sc} = 14.68 mA cm^{-2}, V_{oc} = 0.558 V, fill factor = 50.21%, and η = 4.12%. Evidently, the power conversion efficiency of CdS_xSe_{1-x}-sensitized SSCs is fairly comparable to the best-performing cascaded 5CdS/5CdSe cells as shown in Table 4.1.

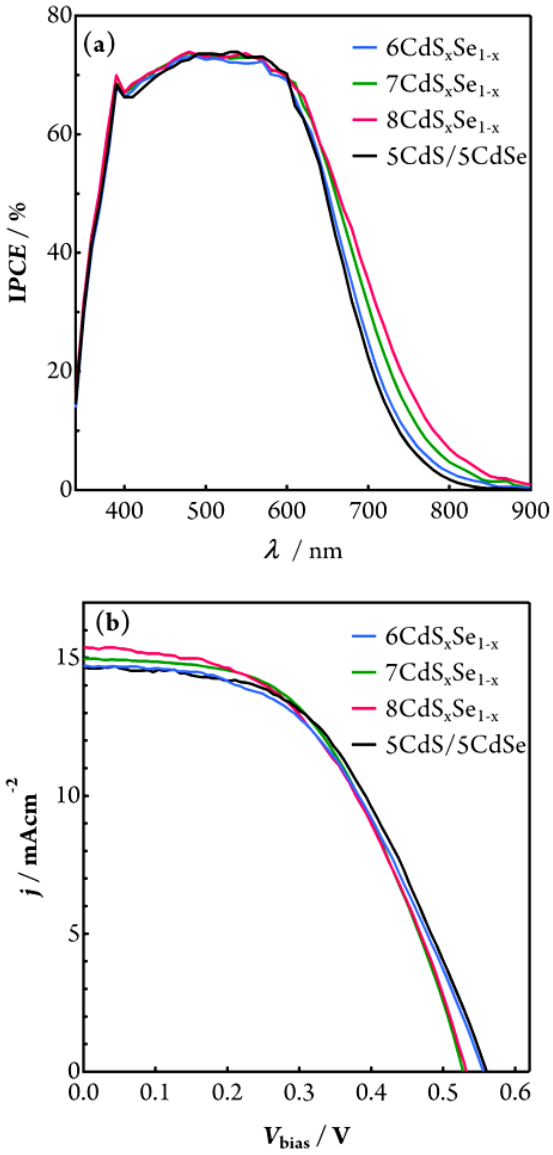

Figure 4. 4 (a) IPCE spectra and (b) *j-V* characteristics of cells made with solid solution $nCdS_xSe_{1-x}$ and cascaded 5CdS/5CdSe-sensitized TiO_2 electrodes consisting of a 5 µm transparent layer (Degussa, P25) and a 4 µm scattering layer (WER2-O, Dyesol). Cu_2S on brass counter electrode and aqueous S^{2-}/S_x^{2-} electrolyte were used for all cells.

Table 4. 1 Characteristics of $nCdS_xSe_{1-x}$ and 5CdS/5CdSe-sensitized solar cells under simulated AM 1.5 100 mW cm^{-2} illumination. Cu_2S on brass counter electrode and aqueous S^{2-}/S_x^{2-} electrolyte were used for all cells.

Photoanode	V_{oc} *(V)*	j_{sc} *(mA* cm^{-2}*)*	*ff (%)*	*η (%)*
$6CdS_xSe_{1-x}$	0.554	14.72	48.61	3.96
$7CdS_xSe_{1-x}$	0.526	14.96	51.40	4.05
$8CdS_xSe_{1-x}$	0.531	15.34	48.50	3.95
5CdS/5CdSe	0.558	14.68	50.21	4.12

Cells with enhanced stability were also fabricated using platinized FTO as the counter electrode for IS measurements. The characteristics of the cells made with platinized FTO cathodes are shown in Figure 4.5 and Table 4.2, which shows comparable performance of $6CdS_xSe_{1-x}$ and 5CdS/5CdSe-sensitized solar cells. The higher j_{sc} and V_{oc} of cascaded 5CdS/5CdSe cells compared to $6CdS_xSe_{1-x}$ cells as shown in Figure. 4.5 will be investigated by IS measurement in the following section.

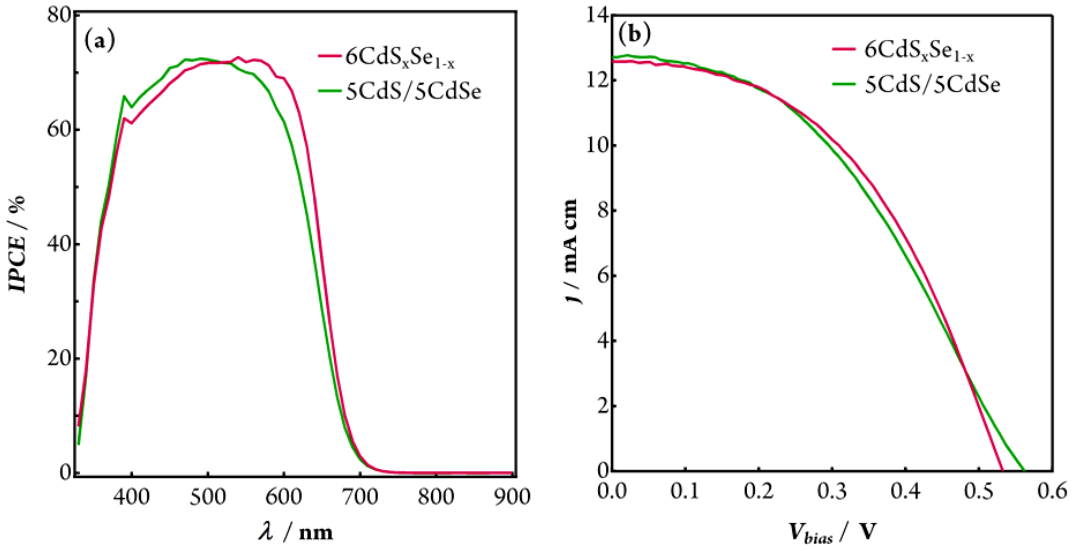

Figure 4. 5 IPCE (a) and *j-V* characteristics (b) of solar cells made with $6CdS_xSe_{1-x}$ and 5CdS/5CdSe-sensitized TiO_2 photoanodes (5 µm thick TiO_2 electrodes without scattering layers) with platinized FTO cathodes for impedance study.

Table 4. 2 Characteristics of $6CdS_xSe_{1-x}$ and 5CdS/5CdSe-sensitized TiO_2 solar cells made with platinized FTO cathode for IS measurements as shown in Figure 4.5.

Photoanode	*Sensitizer*	V_{oc} *(V)*	j_{sc} *(mA cm^{-2})*	*ff (%)*	*η (%)*
TiO_2 (5 µm)	$6CdS_xSe_{1-x}$	0.539	12.57	43.83	2.97
	5CdS/5CdSe	0.563	12.70	41.76	3.00

4.6 Charge transport and transfer investigation by impedance measurement

To understand the charge collection and separation kinetics in CdS_xSe_{1-x}-sensitized cells, IS measurements were carried out with $6CdS_xSe_{1-x}$ cells utilizing platinized FTO as the counter electrode for improved stability. In addition, only the transparent mesoporous TiO_2 layer was used in the sensitized photoanode to simplify the interpretation of impedance data. For photovoltages in the range of 0.1–0.3 V, a well-defined Warburg-like feature can be observed in the intermediate frequency region of the spectra, which can be assigned to electron transport in the TiO_2 layer (Fig. 4.6 (a, b)). A good fit to most spectra could be obtained using an equivalent circuit (Fig. 3.6, in Chapter 3) based upon the diffusion-reaction model for a porous electrode, as described by Bisquert.[84]

The fits of charge transfer resistance (R_{ct}) and transport resistance (R_t) at different open-circuit photovoltages are plotted in Figure 4.6(c). Apparently, both R_{ct} and R_t attenuate exponentially with increasing bias voltage at elevated illumination intensity. As shown in Figure 4.6(d), the effective electron diffusion length (L_n) is calculated to be ~6 times as long as the TiO_2 film thickness (d) at lower bias (< 0.15 V) and becomes even longer at higher bias, ensuring almost unity charge collection.[48]

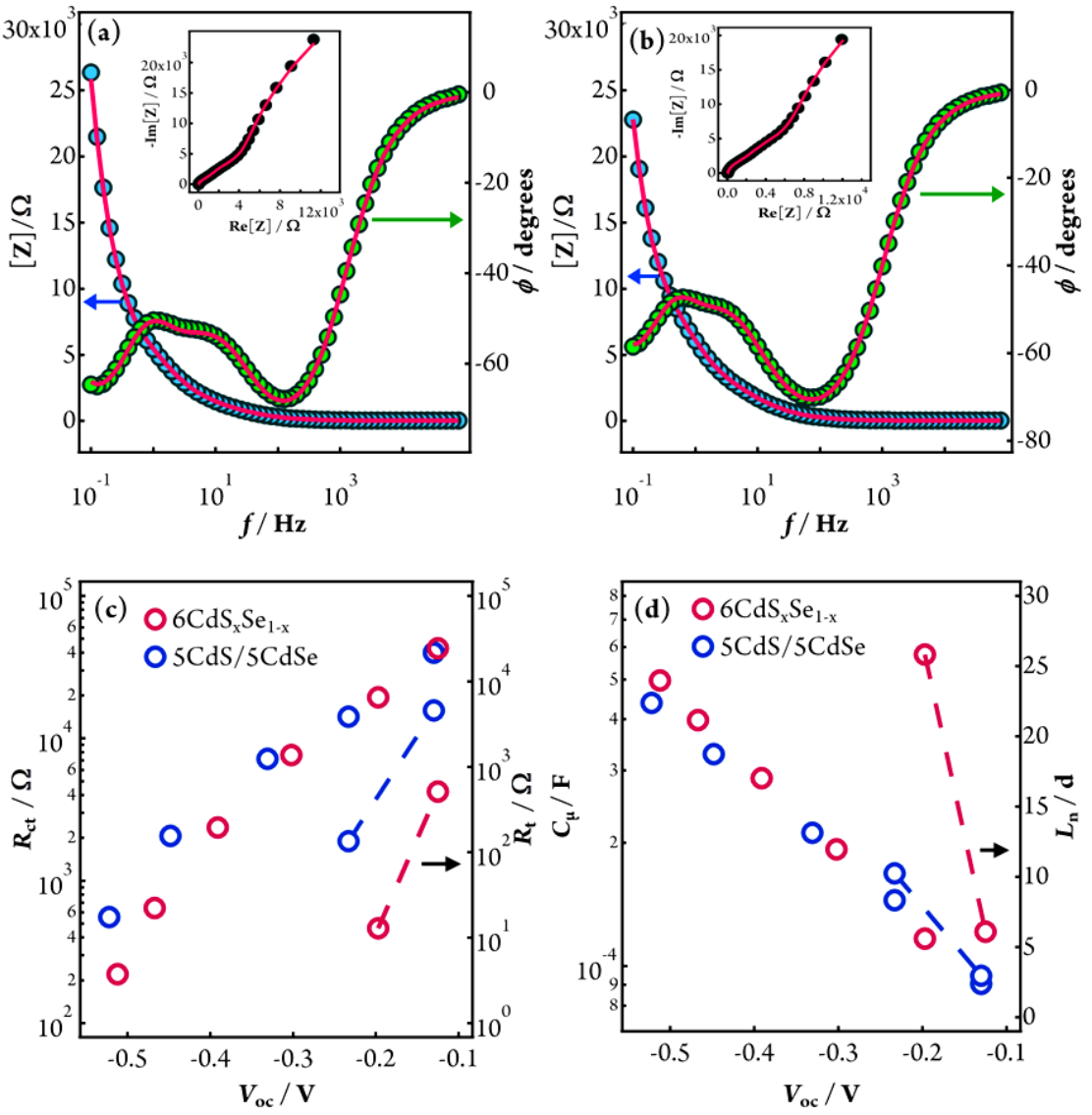

Figure 4. 6 Bode and Nyquist plots showing typical IS results (circle) and best fits using the diffusion-reaction model (solid red lines) for SSCs utilizing (a) $6CdS_xSe_{1-x}$ and (b) 5CdS/5CdSe-sensitized 5 μm TiO_2 electrodes and platinized FTO cathodes. Charge transfer resistance (R_{ct}) and transport resistance (R_t) (c), and chemical capacitance (C_μ) and electron diffusion length divided by film thickness (L_n/d) (d) obtained from IS fitting result and plotted versus open-circuit photovoltage (V_{oc}).

Figure 4.6 also compiles the kinetic parameters of the 5CdS/5CdSe cell obtained from IS measurements under similar conditions. As shown in Figure 4.6(c), R_{ct} for the $6CdS_xSe_{1-x}$ cell was slightly lower than for the cell made with 5CdS/5CdSe when the bias potential is higher. This indicates a higher recombination rate in the former cells,

explaining the slightly lower V_{oc} of the $6CdS_xSe_{1-x}$ cells as compared to that of 5CdS/5CdSe (Table 4.2). In contrast, while the exact reason is to be elucidated, the R_t of the 5CdS/5CdSe cell is almost 10 times larger than the $6CdS_xSe_{1-x}$ cell in the measureable potential range (Fig. 4.6(c)), which yields a much shorter diffusion length. However, since L_n is still at least 2 times longer than the film thickness, the charge collection loss should not be an issue in 5CdS/5CdSe cells (Fig. 4.6(d)). On the other hand, the C_μ-V_{oc} plots of both cells are nearly identical. As reported by Hod *et al.*, the chemical capacitance of semiconductor-sensitized TiO_2 measured by IS is a combination of localized states in both TiO_2 and semiconductor sensitizer, which are indistinguishable by electrical techniques.[86] However, in the present case the density of localized states, which may contribute to the recombination, is rather close regardless of the sensitizer on the surface. A similar phenomenon was also observed in a comparative study between CdSe and CdS/CdSe-sensitized TiO_2 described in Section 3.5 in Chapter 3, which needs a systematic study to unambiguously understand the detailed origins of the localized states and their roles in interfacial charge recombination.

4.7 Summary

Ternary solid solution, cadmium sulfoselenide (CdS_xSe_{1-x}) was successfully synthesized by the SILAR method, which only involves alternate deposition of CdS and CdSe layers under ambient conditions and was used as sensitizer for mesoscopic TiO_2 electrodes. By tuning the composition or changing the number of deposition cycles of the constituent materials, the optical band gap and consequently the band energies of CdS_xSe_{1-x} can feasibly be adjusted between the energy levels of CdSe and CdS of similar dimensions. The as-prepared amorphous CdS_xSe_{1-x} on TiO_2 exhibits

excellent photovoltaic performance when used as light absorber for SSCs, which is comparable to the more commonly studied cascaded CdS/CdSe electrodes. Using aqueous polysulfide solution (S^{2-}/S_x^{2-}) as electrolyte and Cu_2S as counter electrode, a power conversion efficiency of 4.05 % was achieved with $6CdS_xSe_{1-x}$-sensitized TiO_2 as photoanode under simulated AM 1.5 100 mW cm^{-2} illumination. These findings provide a viable alternative approach to tune the energetic of semiconductor sensitizers with nanostructure metal oxides, especially for those with narrow band gaps to achieve favorable band alignment for efficient charge separation in SSCs.

5 CdSe-Sensitized SnO_2 Solar Cells: A Rival to TiO_2 Cells?

5.1 Introduction

Nanostructured tin dioxide (SnO_2) has generated great scientific and technological interest in the past two decades because of its diverse optical, electrical and electrochemical properties and potential applications, such as a transparent conducting oxide substrate for flat panel display and solar cells,[114,115] anodic material for lithium ion batteries,[116,117] photoelectrode for DSCs,[118,119] sensors,[120,121] *etc.* SnO_2 is an *n*-type semiconductor with an optical band gap of ~3.6 eV, which corresponds to a light absorption onset of ~340 nm.[122] As a result, SnO_2 is less likely to generate holes in the valence band through direct photon absorption, and the solar cell ought to be more robust under UV illumination than the TiO_2.[123] SnO_2 is known to have 10-100 times higher electron mobility than nanostructured TiO_2,[21,22,124] a common choice of material in the aforementioned applications, especially as photoanode in semiconductor- and dye-sensitized solar cells.[23,118,119] In addition, the conduction band minimum (CBM) of SnO_2 is 300-500 mV more positive than that of anatase TiO_2, suggesting more efficient charge injection from light absorbers should be possible.[69,124,125]

As reviewed in Sections 3.1 and 4.1, mostly nanocrystalline TiO_2 is used as the photoanode utilizing CdS, CdSe and cascaded CdS/CdSe sensitizers and the highest efficiencies of SSCs reported in the last few years are in the range of 4-5.5%.[12-14,28,30,45,64,126] While the photovoltaic conversion efficiencies for cells employing SnO_2

are notoriously poor in DSCs, exploitation of the low CBM of SnO_2 should facilitate charge transfer from low band gap sensitizers such as the near infrared light absorbers, PbS,[20,69] PbSe,[127] and $CuInSe_2$,[128] *etc*., where light harvesting could be significantly enhanced by utilizing long wavelength photons. Therefore, nanostructured SnO_2 seems an interesting photoanode material, which could in principle facilitate efficient charge injection and charge collection.

It has been shown by a few groups that the photo-conversion efficiency of a SSC can be enhanced by co-sensitization of CdS and CdSe in a layered structure of TiO_2/CdS/CdSe, where the band edges of the three materials form a stepwise cascade, which is advantageous for the separation of excited electrons and holes across the interfacial region.[19,35,45,78,129] However, the recent study presented in Chapter 3 shows that CdSe alone is better for efficient device fabrication than that of cascaded CdS/CdSe sensitizer. The efficient device performance of CdSe-based cell was realized by suppressed charge recombination at the TiO_2/CdSe interface in the absence of the CdS buffer layer. Therefore, in this study, layers of semiconductors (CdS/CdSe) were coated conformally onto SnO_2 by the SILAR method, and compared with the CdSe-sensitized SnO_2 electrodes. A passivation layer of TiO_2 on the SnO_2 surface is necessary before deposition of CdS or CdSe in order to reduce the density of electron trap states at the surface of SnO_2. Likewise, a barrier layer of ZnS, deposited by a post-treatment onto the CdSe and cascaded CdS/CdSe, is required to inhibit the recombination of injected electrons with acceptor species (S_x^{2-}) in the electrolyte as investigated by our group.[23]

In this study, attempts to improve the photocurrent of SSCs by using SnO_2 as a photoanode instead of TiO_2 are described. The basic *j*-*V*, IPCE, and optical

measurements have been combined with IS measurement in order to scrutinize charge generation, transport, and recombination in these SSCs. Ultimately, a record photocurrent density of 18.57 mA cm^{-2} and 17.40 mA cm^{-2} was obtained for CdSe and CdS/CdSe-sensitized SnO_2-based solar cells, respectively, under simulated AM 1.5, 100 mW cm^{-2} illumination when an aqueous S^{2-}/S_x^{2-} electrolyte and a Cu_2S on brass cathode were used. The maximum IPCE was observed to be close to 80% over a wide wavelength range, indicating almost unity quantum efficiency, after correction for light absorption by the FTO substrate. Utilizing CdSe and CdS/CdSe-sensitized SnO_2 electrodes, very promising overall power conversion efficiencies of up to 4.37% and 3.68% were achieved, respectively, making nanostructured SnO_2 a potential rival to TiO_2 for use in SSCs.

5.2 Preparation of CdSe and CdS/CdSe-sensitized mesoscopic SnO_2 electrodes

The $TiCl_4$ treated mesoscopic SnO_2 electrodes (0.6 cm diameter) were sensitized with CdS and CdSe following the SILAR method discussed in Section 2.3.1 of Chapter 2.[23,28,45] In brief, first CdS was deposited on the SnO_2 electrodes using the SILAR method by repeating 5 times in order to get a suitable CdS loading. In order to prepare CdSe and cascaded CdS/CdSe-sensitized SnO_2 electrodes, SILAR cycles for CdSe deposition were then repeated several times onto bare SnO_2 and CdS-coated SnO_2 electrodes to get a suitable CdSe loading, respectively.[28] A ZnS passivation layer (two SILAR cycles) was deposited on CdSe and CdS/CdSe-coated SnO_2 electrode by the SILAR method described in Section 2.4 in Chapter 2. For comparison, cascaded CdS/CdSe was also deposited on ~9 μm thick TiO_2 electrodes (without scattering layers) following the identical fabrication procedure to that used for CdS/CdSe-sensitized SnO_2 electrodes.

5.3 Morphology investigation of CdSe and CdS/CdSe-sensitized SnO_2 nanoparticles

Figure 5.1(a) shows a TEM image of 5CdS/5CdSe-coated SnO_2 nanoparticles, with approximate sizes in the range of 20–40 nm. HRTEM images (Fig. 5.1(b - d)) suggest that these SnO_2 particles consist of crystal grains of 10–40 nm. EDS elemental analysis shows the existence of Cd, S and Se. The atomic ratio Cd/(S+Se) in 5CdS/5CdSe was found to be 1.31, and Cd/Se in 7CdSe was 1.04, indicating that both sensitizer layers as a whole were Cd-rich and broadly consistent with previous reports where Cd-rich CdSe was deposited by SILAR.[77] A conformal coating of 5CdS/5CdSe and 7CdSe on the SnO_2 nanoparticles was revealed by HRTEM as shown in Figure 5.1(c) and 5.1(d), respectively, and the lack of lattice fringes suggests the as-grown sensitizers are amorphous.

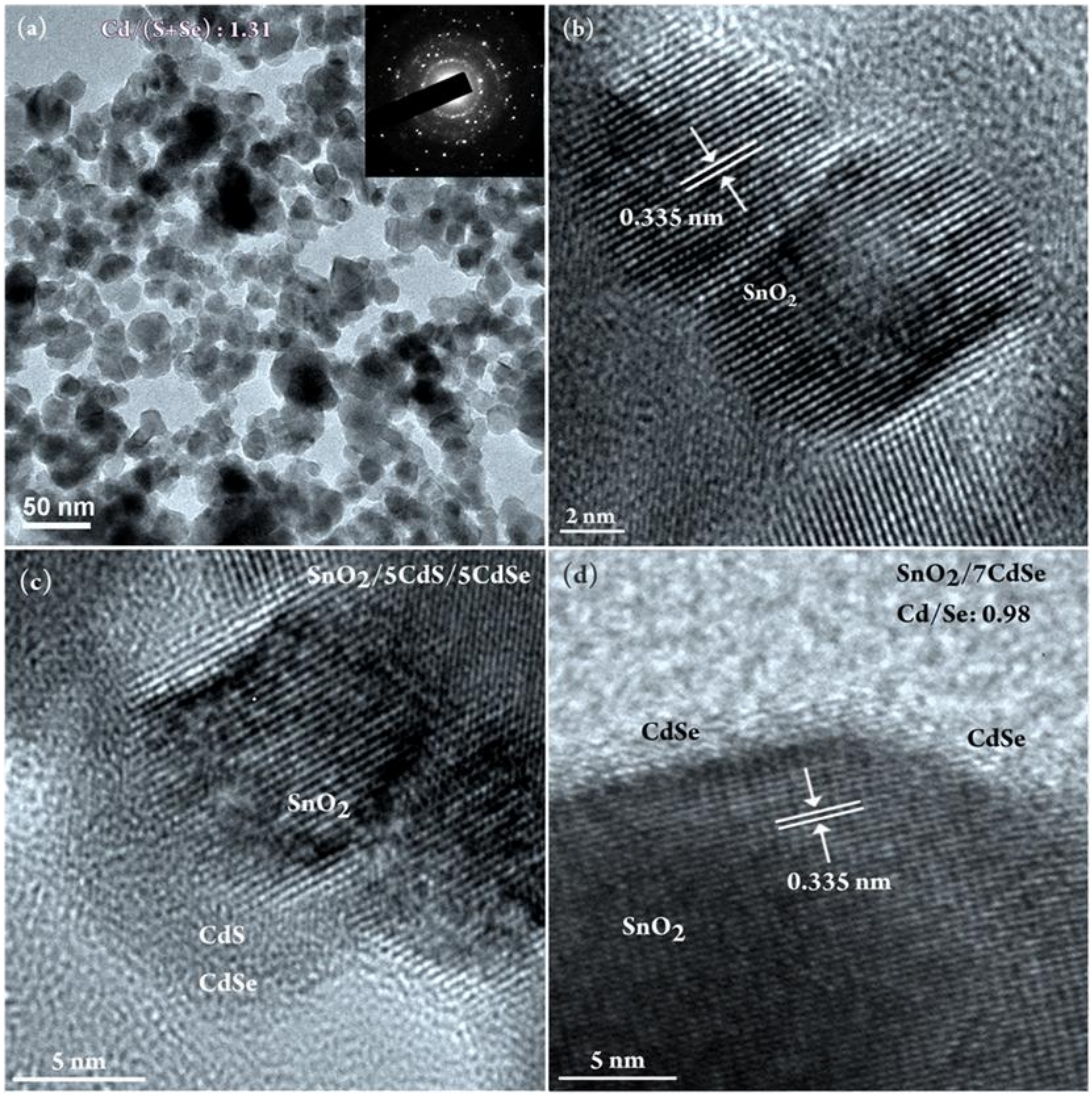

Figure 5. 1 (a) Low resolution TEM image of 5CdS/5CdSe-coated SnO_2 nanoparticles, (b) HRTEM image of SnO_2 nanocrystal grains, (c) conformal coating of 5CdS/5CdSe, and (d) 7CdSe onto SnO_2 nanoparticles.

5.4 Structural characterization of sensitized SnO_2 nanoparticles

The crystal structure of SnO_2 nanoparticles, 5CdS, 7CdSe, and 5CdS/5CdSe-sensitized SnO_2 electrodes were characterized by powder XRD. As shown in Figure 5.2, the XRD pattern reveals that the SnO_2 nanoparticles are polycrystalline, consistent with the HRTEM image (Fig. 5.1(b-d)), which shows lattice fringes with *d*-spacing 0.335 nm, corresponding to the lattice plane (110) of tetragonal rutile SnO_2

(JCPDS No. 72-1147, Fig. 5.2). The calculated grain size of ~12 nm from the Scherrer equation using the first and second peaks of XRD spectra for SnO_2 nanoparticles was consistent with the grain size obtained from analysis of HRTEM images. Additional features due to as-prepared CdS and CdSe were not observed in the XRD analysis, except for a noisier profile, arising because of the amorphous nature of the conformal coating of 5CdS/5CdSe and 7CdSe. However, after heat treatment at 350 °C, the 7CdSe and 5CdS/5CdSe electrodes show broadened diffraction peaks implying the improved crystallinity. These as-prepared electrodes were used directly for optical measurements, solar cell fabrication and characterizations in the subsequent sections of this chapter.

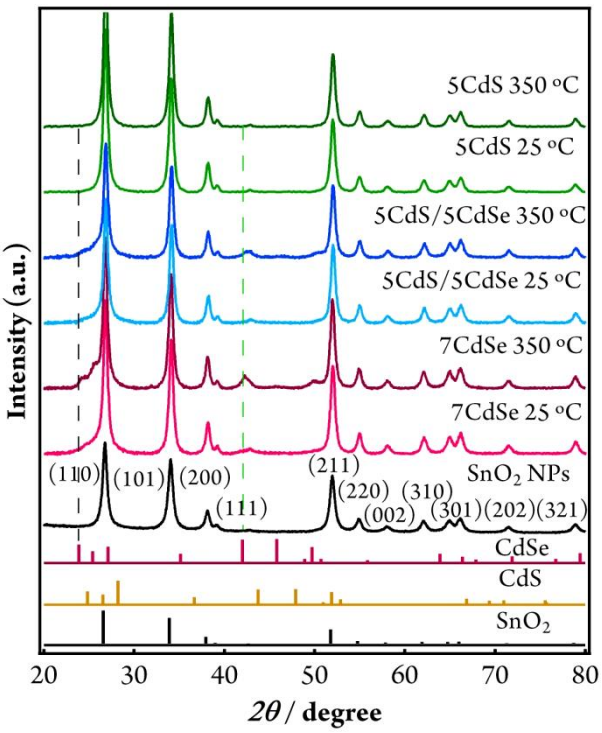

Figure 5. 2 XRD patterns of 5CdS, 7CdSe, and 5CdS/5CdSe-sensitized SnO_2 electrodes made on microscope glass slides before and after heat treatment at 350 °C in a quartz tube under vacuum (~10^{-6} mbar). The standard peak intensities with 2θ values for rutile SnO_2, wurtzite CdS, and CdSe nanocrystals are shown for comparison.

5.5 Optical properties of CdS/CdSe-sensitized SnO_2 electrodes.

Optical density (OD) spectra of CdS, CdSe and CdS/CdSe-sensitized SnO_2 photoelectrodes were collected in a transmission mode utilizing single beam in a Shimadzu UV-vis-NIR spectrophotometer (Solidspec-3700) at room temperature. Figure 5.3 shows OD spectra of a 6.4 µm thick SnO_2 electrode coated with CdS and CdS/CdSe by successive SILAR cycles. The incorporated amount of CdS or CdSe into the SnO_2 films increases with increasing numbers of SILAR cycles. As shown in Figure 5.3, the apparent absorption onset of 5-cycle CdS/SnO_2 electrodes occurs at ~500 nm, representing its bulk nature and optical band gap of 2.50 eV.[130] Successive colour changes from yellow ochre (5/1) to dark red (5/6) were observed with the increase of CdSe deposition cycles (inset of Fig. 5.3), indicating strong absorption of most of the visible wavelengths.

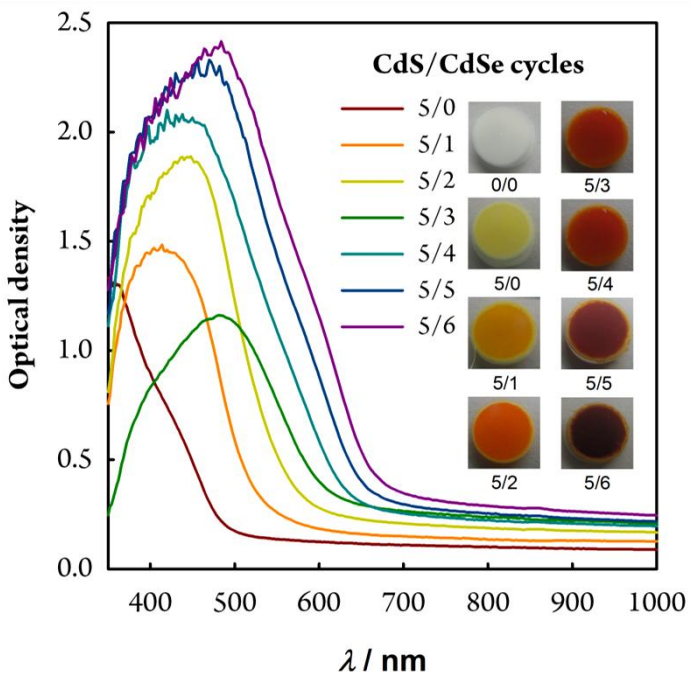

Figure 5. 3 UV-vis optical density spectra of CdS and CdS/CdSe-coated SnO_2 electrodes alongside typical photographs of electrodes with or without 5 cycles of CdS and different numbers of CdSe cycles.

For all spectra an apparent absorbance extending up to 1000 nm was observed which systematically increases with the number of SILAR deposition cycles. We suspect this is due to uncorrected light scattering losses, which increase with increasing CdS/CdSe coverage; rigorous corrections for light scattering using diffuse transmittance and reflectance measurements have not yet been attempted. Despite the ambiguities caused by scattering effects, it still seems very reasonable to assume that the light harvesting efficiency of the sensitized electrodes is almost unity in the wavelength range 400-500 nm, where an OD of > 2 is found for *ca.* 6 µm thick electrodes (note that the electrodes used in complete SSCs were 9 µm thick). The same conclusion can be drawn for a 5.4 µm thick TiO_2 electrodes sensitized with 5CdS/5CdSe SILAR cycles, which have similar OD spectra (Fig. 5.4). Based upon these data, the light harvesting efficiency of the electrode is predicted to be greater than 99% between 400 and 600 nm for the optimized 9 µm thick TiO_2 layers used to fabricate SSCs.

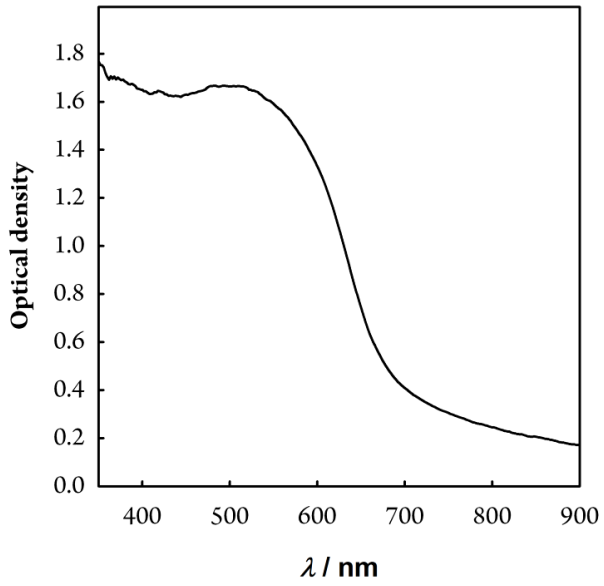

Figure 5. 4 Optical density spectrum for a 5.4 µm thick 5CdS/5CdSe-sensitized TiO_2 electrode.

A deviation in the magnitude of OD was also observed for the specific case of a 5/3 combination of CdS/CdSe, where the absorption onset followed the trend of the other films, but the peak absorption was less than for 5/2 and 5/4 CdS/CdSe combinations. This surprising result was found to be due to inaccurate baseline subtraction (OD of SnO_2 spectrum was subtracted from that of SnO_2/5CdS/3CdSe spectrum). These co-sensitized electrodes have wide wavelength absorption characteristics, emphasizing that the main sensitization comes from CdSe, due to its wider spectral response than CdS. Likewise, due to size-induced electronic quantization phenomena, the absorption onset of CdS/CdSe-sensitized SnO_2 electrodes moves to longer wavelengths with the increase of CdSe deposition cycles, indicating the increment of the thickness of the CdSe layer. The performance of SSCs incorporating CdS/CdSe-sensitized electrodes has been studied and the optimum layer combination is found to be 5CdS/5CdSe. It should be mentioned that the samples of SnO_2/CdS/CdSe used for OD measurements were prepared without $TiCl_4$ pre-treatment or ZnS post-treatment.

5.6 Photovoltaic characteristics of CdS/CdSe-sensitized SnO_2 solar cells

To study the photovoltaic performance of CdS/CdSe-sensitized mesoscopic SnO_2 electrodes, sandwich-type thin layer cells were fabricated with FTO/SnO_2/CdS/CdSe as the photoanode, platinized FTO and Cu_2S on brass as the cathode and S^{2-}/S_x^{2-} as the hole transporter. To prevent recombination at the SnO_2/CdS/CdSe/electrolyte interface, SnO_2 electrodes were treated with $TiCl_4$ aqueous solution prior to CdS/CdSe deposition, and a thin passivation layer of ZnS was deposited onto the sensitized electrode by two SILAR deposition cycles.

Figure 5.5(a) shows the IPCE spectra of CdS/CdSe-sensitized SnO_2 and TiO_2 solar cells, which exhibit a strong photo-response over the entire visible light range, with photon wavelengths even extending to ~850 nm for the SnO_2 SSCs. It has been shown that for the co-sensitized electrode, the higher IPCE in the short-wavelength region is due to the CdS, whereas CdSe harvests light in the long wavelength region; together a better overall IPCE response was observed.[131] IPCEs of ~80% between 400 and 600 nm were achieved with 5/5 layers of CdS/CdSe on SnO_2 and 2 layers of ZnS. Since the IPCE is found to be within a few percent of the transmission of the FTO substrate in this wavelength range, it must be concluded that light harvesting, charge separation and charge collection are all close to unity when SnO_2 electrodes are used.

Figure 5.5(b) shows the *j-V* characteristics of sensitized SnO_2 and TiO_2 SSCs. Photovoltaic parameters of the SSCs are given in Table 5.1. As expected from the IPCE measurements, SnO_2 electrodes exhibit superior short-circuit photocurrents (j_{sc}) as compared to TiO_2 electrodes. The j_{sc} predicted by convolution of IPCE spectra with the AM 1.5 spectrum followed by integration over all wavelengths underestimate the measured 1 Sun j_{sc} values by *ca.* 10%, implying that differences in charge separation and charge collection between the IPCE measurements (which were made using low intensity monochromatic illumination) and the 1 Sun *j-V* measurements are minimal.

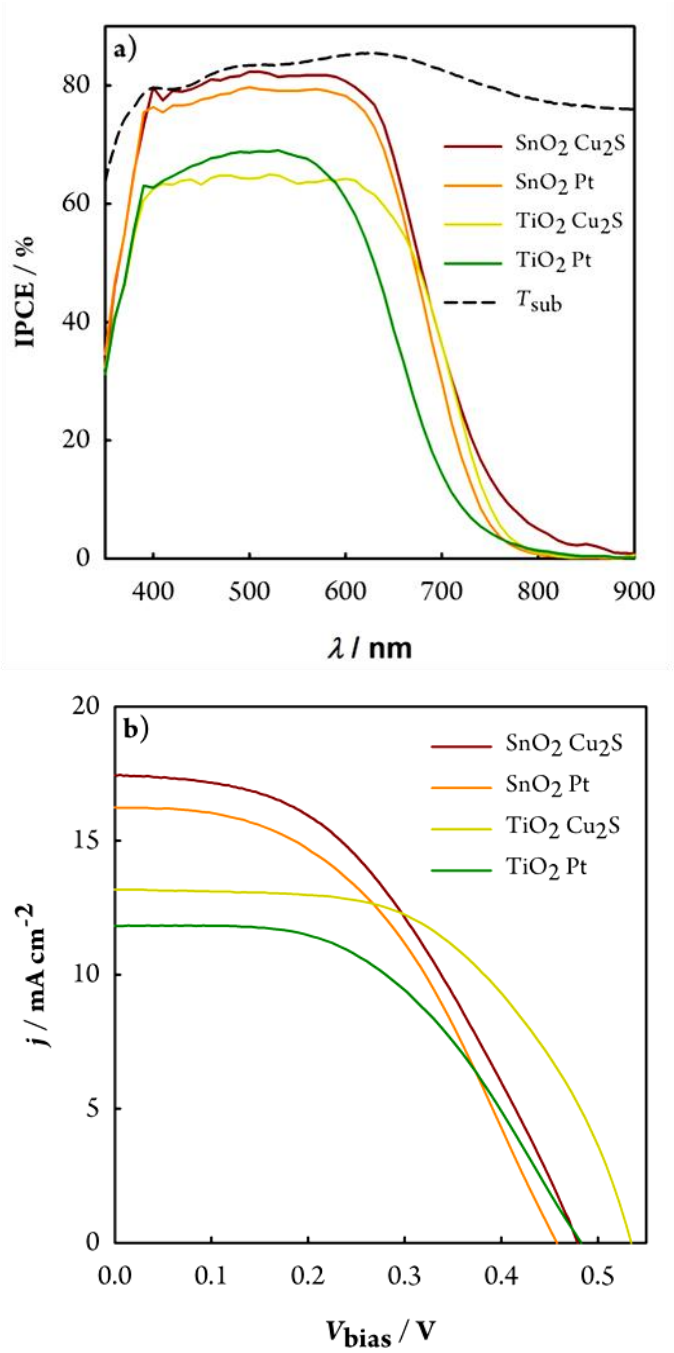

Figure 5. 5 IPCE spectra (a) and *j-V* characteristics (b) of 5CdS/5CdSe-sensitized SnO_2 and TiO_2 solar cells.

The best SnO_2 device was obtained with 5CdS/5CdSe as well as $TiCl_4$ and ZnS pre- and post-treatments, respectively, yielding j_{sc} = 17.4 mA cm^{-2}, V_{oc} = 0.477 V, fill factor = 44.4%, and η = 3.68% under simulated AM 1.5, 100 mW cm^{-2} illumination

(Table 5.1). One plausible reason for the higher photocurrent of the SnO_2 SSC compared with the TiO_2 SSC is better charge transport dynamics in SnO_2 arising from the higher electron mobility, which will shortly be discussed in the light of results from impedance spectroscopy experiments.

Table 5. 1 Characteristics of CdS/CdSe-sensitized SnO_2 and TiO_2 solar cells with platinized FTO and Cu_2S cathodes under simulated AM 1.5, 100 mW cm^{-2} illumination.

Photoanode	*CdS/CdSe*	*Cathode*	V_{oc} *(V)*	j_{sc} *(mA* cm^{-2}*)*	*ff (%)*	*η (%)*
SnO_2	5/5	Pt	0.458	16.20	45.85	3.43
	5/5	Cu_2S	0.477	17.40	44.40	3.68
TiO_2	5/5	Pt	0.484	11.82	49.39	2.85
	5/5	Cu_2S	0.533	13.17	55.28	3.88

It is also known that SnO_2 has a much lower conduction band minimum (CBM) than TiO_2 in the same media. The large driving force for charge injection originating from the low CBM of SnO_2 may help efficient charge injection from excited CdS/CdSe to the conduction band of SnO_2. Leventis *et al.* reported comparative studies of charge separation between PbS-sensitized mesoscopic TiO_2 and SnO_2.[20] Transient optical measurements showed much faster charge injection for the PbS-sensitized SnO_2 electrode.[20] Guijarro *et al.* have shown that the injection of electrons from CdSe into TiO_2 decreases significantly with increasing numbers of SILAR cycles.[77] This could be eliminated by using a low CBM oxide such as SnO_2 for an electron acceptor material. Pijpers *et al.* have shown efficient electron injection from PbSe into SnO_2; however, there was no injection into TiO_2, which was attributed to the different energy band alignments when using these oxides.[132]

$TiCl_4$ treatment effectively passivates the surface of SnO_2 and significantly improves the photovoltaic performance of CdSe-sensitized SnO_2 solar cells.[23] Prasittichai *et al.* have found that the photovoltaic performance of dye-sensitized SnO_2 solar cells increased 5-fold when the surface was passivated with an ultrathin layer of Al_2O_3, stemming from inhibited recombination.[118] In addition, SILAR deposition forms a conformal coating of CdS and CdSe on SnO_2, which acts as a barrier layer (in a similar way to Al_2O_3), preventing injected electrons in SnO_2 from recombining with holes in the electrolyte. Moreover, it is believed that surface modification by ZnS further inhibits the recombination of excited electrons at the electrode/electrolyte interface and increases the injection from the sensitizer into SnO_2.[36,133,134]

For comparison, the same thickness of TiO_2 as that of SnO_2 electrode was used to deposit 5CdS/5CdSe using the same precursor solution. An optimized TiO_2 SSCs yielded j_{sc} = 13.17 mA cm^{-2}, V_{oc} = 0.533 V, fill factor = 55.28%, and η = 3.88%, when Cu_2S cathodes were used (Table 5.1). The better overall performance of the TiO_2 cell with the same configuration arises from the higher fill factor and slightly higher V_{oc}, which compensate for the lower photocurrent. When platinized FTO cathodes were used in place of Cu_2S cathodes, performance with both oxides was found to be lower due to inferior fill factor and j_{sc}. While the photocurrent of CdS/CdSe-sensitized SnO_2-based SSCs is significantly higher than the value reported for CdS/CdSe-sensitized TiO_2 cells,[28,45,78] the overall efficiency still remains lower because of lower fill factor. It is not surprising that the V_{oc} of the SnO_2 cell would be lower than the TiO_2 SSCs because of the low CBM and unchanged redox level of the S^{2-}/S_x^{2-} electrolyte, and in fact a much larger loss in V_{oc} might be expected.

The effect of the SnO_2 mesoporous film thickness on the cell performance was investigated by varying the film thickness from 5.5 to 10.5 μm, with the same CdS/CdSe sensitizer loading. Photocurrents normally increased with film thickness but V_{oc} and fill factor dropped, eventually leading to a decrease in efficiency for thicknesses >9 μm. For the TiO_2-based SSCs an optimum thickness of ~9 μm was also found.

5.7 Charge transport and recombination in CdS/CdSe-sensitized SnO_2 cells

Impedance spectroscopy was used to compare the charge transport and charge transfer processes occurring in TiO_2- and SnO_2-based SSCs. Figure 5.6 shows the representative IS spectra for TiO_2- (Fig. 5.6(a)) and SnO_2-based SSCs (Fig. 5.6(b)). For the case of the TiO_2-based SSCs, excellent fits to most spectra (dashed red lines in Fig. 5.6(a)) can be obtained using an equivalent circuit based upon the now ubiquitous diffusion-reaction model for a porous electrode (Fig. 3.6, in Chapter 3), as described by Bisquert.[84]

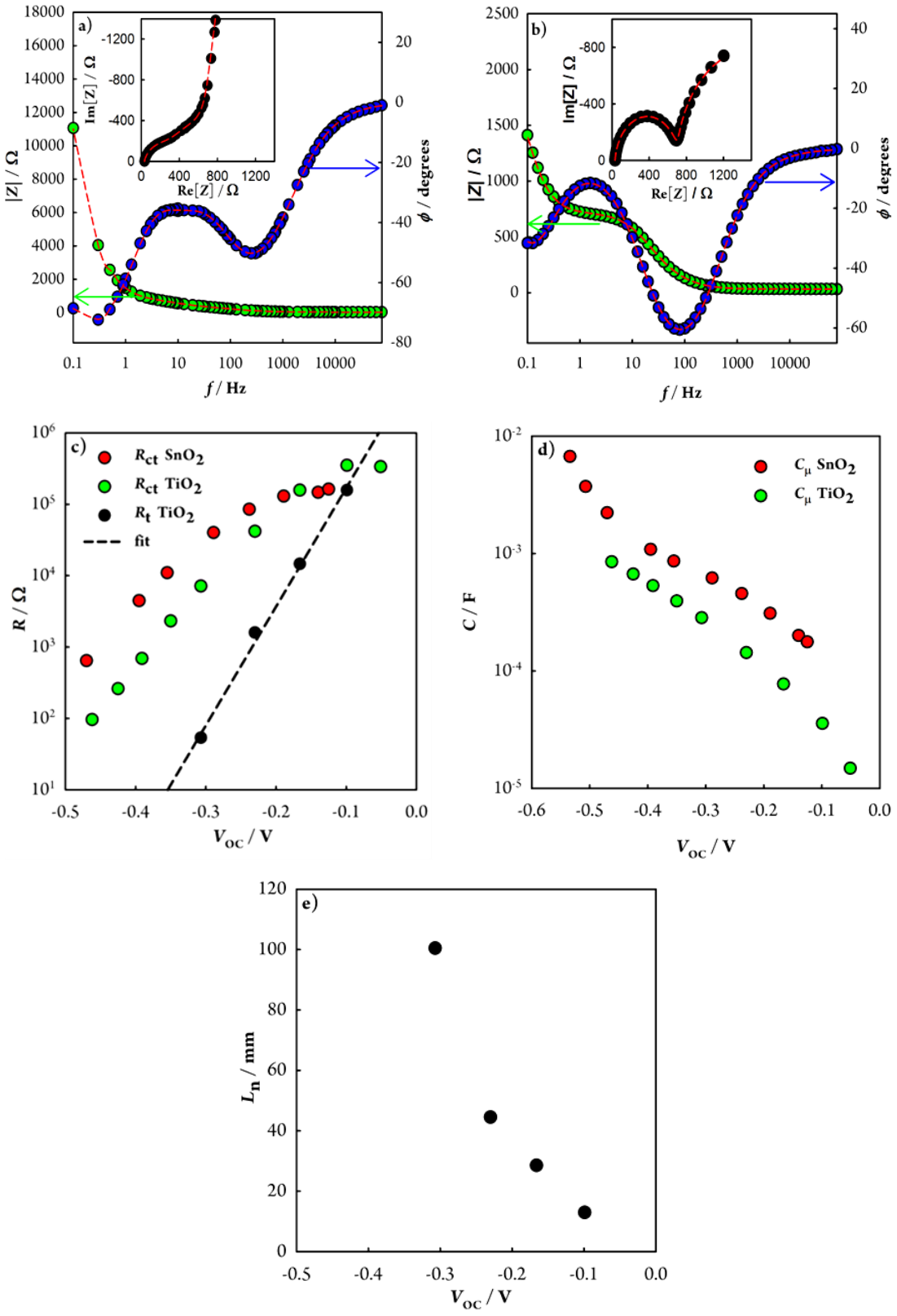

Figure 5. 6 Bode and Nyquist plots showing typical IS results and best fits using the diffusion -reaction model (dashed red lines) for TiO_2- (a; V_{oc} = -0.23 V, incident photon flux *ca.* 3 × 10^{14} cm^{-2} s^{-1}, λ = 627 nm) and SnO_2- (b; V_{oc} = -0.19 V, incident photon flux *ca.* 3 × 10^{14} cm^{-2} s^{-1}, λ = 627 nm) based SSCs; Charge transfer resistance and transport resistance (c), and chemical capacitance (d) parameters obtained from fitting; Dependence of electron diffusion length derived from IS fitting results on open-circuit photovoltage for a TiO_2-based SSC (e).

In spectra recorded for TiO_2-based SSCs, for photovoltages in the range 0.1–0.3 V, a clear Warburg-like feature can be observed, which is consistent with previous reports and can be assigned to electron diffusion in the TiO_2 layer.[45] The associated R_t decreases as V_{oc} becomes increasingly more negative, corresponding to the electron quasi-Fermi level rising towards the CBM and the free carrier concentration in the semiconductor increasing. The slope on a semi-logarithmic plot of R_t versus V_{oc} (dashed black line in Fig. 5.6(c)) is 16.6 V^{-1}, which is in good agreement with the theoretical value of 17 V^{-1} at 295 K, lending support to the assignment of the Warburg-like impedance feature to the electron transport process.

On the contrary, for the SnO_2-based SSCs, no high-frequency Warburg-like feature is observed under any conditions (*cf.* Fig. 5.6(b)) and excellent fits to the data can be obtained with a simplified equivalent circuit consisting of the series connection of a resistor and two parallel RC circuits (Fig. 5.7). One RC circuit represents the SnO_2 layer (with negligible resistance to electron transport), and the other represents the cathode-electrolyte interface.

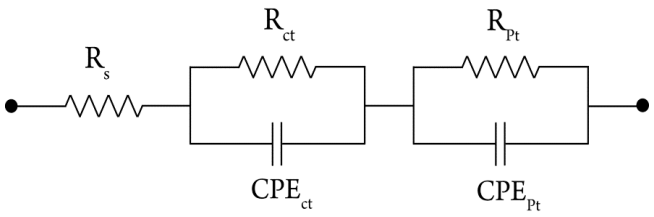

Figure 5. 7 Equivalent circuit used to fit impedance spectra of CdSe and CdS/CdSe-sensitized SnO_2-based solar cells.

R_{ct} is the charge transfer resistance at the photoanode/electrolyte interface; CPE_{ct} is the constant phase element containing the chemical capacitance (C_μ) of SnO_2. R_{Pt} is

the resistance to charge transfer at the platinized FTO cathode and electrolyte interface, and CPE_{Pt} is the corresponding constant phase element containing the double layer capacitance (C_{Pt}) at the platinized FTO electrode. This finding implies that the electron transport resistance for these cells is always much lower than the cathode impedance; if this were not the case it ought to be apparent in the impedance spectrum. Consequently, the electron diffusion length in these cells is expected to be exceedingly long compared with the SnO_2 layer thickness.

A crude estimate of the minimum electron diffusion length at the cell voltage of the maximum power point (V_{mpp}) for the SnO_2-based SSC can be made by taking the SnO_2 interfacial charge transfer resistance (R_{ct}) at a photovoltage corresponding to V_{mpp}, and assuming the electron transport resistance (R_t) is equal to the cathode charge transfer resistance (probably a gross overestimation). This approach yields L_n of the order of 10 times the SnO_2 layer thickness, implying a collection efficiency of practically unity, regardless of optical considerations. This estimate is entirely consistent with the IPCE spectra for SnO_2-based SSCs employing Cu_2S cathodes, where IPCE values approaching the substrate transmission are found (*cf.* Fig. 5.5(a)). Attempts were made to more precisely estimate L_n at various photovoltages by using a combination of intensity-modulated photovoltage spectroscopy (IMVS) and intensity-modulated photocurrent spectroscopy (IMPS). However, ultimately this was not possible because under all conditions studied (open-circuit, various light intensities) the IMPS response was found to be dominated by the RC time constant of the cells and deconvolution of the transport time constant with any reasonable degree of accuracy was impossible.

Attempts were also made to observe electron transport features in the IS spectra by using a Cu_2S electrode to reduce the impedance of the cathode. However, due to the instability of the Cu_2S on brass cathodes, interpretation of impedance spectra were complicated by non-negligible drift of the system on the time scale of the measurements (which typically took ~2 hours) thus further analysis will not be presented here. However, it is noteworthy that, in these experiments, features in the impedance spectra (*e.g.*, slope of ~1 in Nyquist plots), which were clearly attributable to an electron transport resistance were not observed.

For the TiO_2-based SSCs, long electron diffusion lengths are also found for V_{oc} > 0.2 V, where L_n is greater than 3 times the TiO_2 layer thickness, sufficient to ensure almost 100 % efficient charge collection, regardless of illumination direction and absorption coefficient.[135] Below V_{oc} = 0.2 V, L_n decreases into a regime where charge collection losses could begin to become a photocurrent loss mechanism (the extent of which will depend upon the precise absorption coefficient of the sensitized metal oxide layer and on the illumination direction). However, this exceptionally low quasi-Fermi level position (obtained under very low incident light intensity) is unlikely to be encountered in the device under normal 1 Sun operating conditions, where the average quasi-Fermi level in the bulk of the metal oxide layer for cell voltages below V_{mpp} (*e.g.* short-circuit) is expected to be only 0.15 – 0.25 V lower than V_{oc} at the same light intensity.[136-138] The 10-100 times higher electron mobility in crystalline SnO_2[22] than that in anatase TiO_2[21] probably contributing to the conspicuous absence of a prominent Warburg feature in the IS spectra for SnO_2-based SSCs, despite it being observed for otherwise identical TiO_2-based SSCs.

Peak IPCE and j_{sc} values for SnO_2-based SSCs are around 30–40 % higher than for TiO_2-based SSCs (the same batch of precursor solution was used to sensitize the both electrodes). Based upon the diffusion length estimations for the TiO_2-based device it appears unlikely that this difference can be explained by charge collection losses in the TiO_2-based SSCs. This is because, despite the apparently superior transport properties of SnO_2 compared with TiO_2, transport is still fast enough to avoid collection losses in the TiO_2-based SSCs. Assuming that differences in light harvesting efficiency between SnO_2 and TiO_2 electrodes are not significant over most of the absorbed wavelength range (this assumption is supported by light absorption measurements for λ = 400 to at least λ = 500 nm; Fig. 5.4), it is likely that the cause for higher IPCE and photocurrent is that the overall charge separation yield in SnO_2-based SSCs is higher than in TiO_2-based SSCs. Since identical electrolytes and sensitizer deposition procedures were used for both types of SSC, it must be concluded that either charge injection from the CdS/CdSe to the metal oxide is slower in the TiO_2 system compared to the SnO_2 system, or that the reverse process, geminate recombination, is faster in the TiO_2 system.

The CBM of SnO_2 is thought to lie 0.3-0.5 eV below that of anatase TiO_2 and therefore, on purely energetic grounds, a higher charge injection efficiency might be expected. However, one must also consider that use of Marcus-Gerischer electron transfer theory is probably more appropriate for predicting the probability of electron transfer from the semiconductor sensitizer to the metal oxide. In this case the density of acceptor states at the relevant energy (the energy of the excited states of CdS/CdSe) in the metal oxide is more important than the free energy difference between initial and final states in the charge transfer process.

The conventional interpretation of the porous electrode capacitance obtained from IS data using the diffusion-reaction model is that it corresponds to a chemical capacitance, that is, a measure of the effective density of states around the quasi-Fermi level, which, in turn, is related to V_{oc} by $V_{oc} = {}_nE_F - E_{F,redox}$. Since identical electrolytes were used in both types of SSC, comparisons of C_μ at matched V_{oc} ought to reveal differences between the densities of states in the two oxides, on an energy reference scale relevant to the operation of these cells. Figure 5.6(d) clearly shows that at any given V_{oc}, C_μ for the SnO_2-based device is at least 2 times larger than for the TiO_2-based device, and at lower voltages is almost 4 times larger. Thus, if it is permissible to extrapolate these results to the energies relevant to charge injection, the higher IPCE values for the SnO_2-based SSCs compared with the TiO_2 counterparts may be due to enhanced electron injection, as a result of the higher density of electron acceptor states at the appropriate energy. The shift along the voltage axis between the two plots in Figure 5.6(d) might also be viewed as evidence that the SnO_2 layer has a lower conduction band minimum than TiO_2, as expected. However, since the density of states functions for the two materials are not known and are unlikely to be the same, quantifying the difference in band edge energies is not possible without more information.

It is also interesting to note that the charge transfer resistance (R_{ct}) for the SnO_2-based SSC is up to 6 times larger than that for the TiO_2-based SSC. At very low photovoltages similar R_{ct} values are found, but data obtained at these photovoltages are not likely to be relevant to normal operation of the cells. The larger R_{ct} is a factor, which contributes towards the surprisingly high photovoltages achieved by the SnO_2-based SSCs, which are only 26–56 mV lower than for TiO_2-based SSCs, despite the far more positive CBM of SnO_2. However, it must also be borne in mind that the

effective density of states at the CBM (N_C), together with the energy of the CBM, determines the free electron concentration required to produce a particular quasi-Fermi level position and V_{oc}. The effective electron mass in SnO_2 is reported to be *ca.* 35 times smaller than estimates for nanocrystalline TiO_2,[139,140] thus significant differences in N_C between the two materials probably exist, and the relatively small difference in V_{oc} between the cells cannot be solely attributed to slower charge recombination in the SnO_2-based SSCs.

5.8 Photovoltaic and charge transport characteristics of CdSe and CdS_xSe_{1-x}-sensitized SnO_2 solar cells

To investigate the photovoltaic performance of CdSe-sensitized SnO_2 electrodes (7.4 μm thick), cells were made with Cu_2S and platinized FTO cathodes, and S^{2-}/S_x^{2-} hole conductor. As the case of 7CdSe and 5CdS/5CdSe-sensitized TiO_2 electrodes, 7CdSe, 5CdS/5CdSe, and 6CdS_xSe_{1-x}-sensitized SnO_2 electrodes with approximately the same OD (inset of Fig. 5.8(a)), were used to fabricate cells. These OD spectra represent the actual light absorption by sensitizers as light absorption by the substrate (SnO_2) was subtracted from light absorption of the corresponding sensitized electrodes (SnO_2/CdSe *etc.*). Like the TiO_2 cells as discussed in Chapter 3, the IPCE spectra of both 7CdSe and 5CdS/5CdSe-sensitized SnO_2 solar cells exhibit excellent photoelectrical response with photon wavelengths even extending to >800 nm. As shown in Figure 5.8(a), both the cells made with Cu_2S counter electrodes exhibit IPCE of ~80% between 400 and 650 nm, while the CdSe-sensitized SnO_2 electrode presents much superior IPCE at longer wavelengths (> 650 nm), contributing to the improvement of photocurrent.

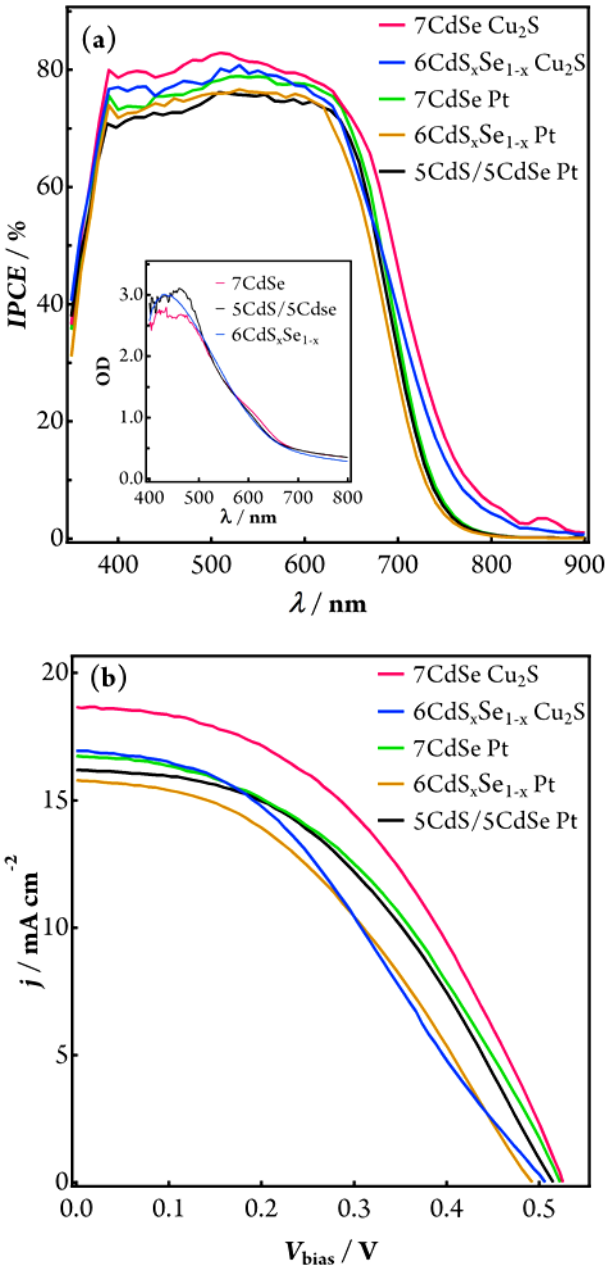

Figure 5. 8 (a) IPCE spectra, and (b) *j-V* characteristics of 7CdSe, $6CdS_xSe_{1-x}$, and 5CdS/5CdSe-sensitized SnO_2 (7.4 μm thick) solar cells with Cu_2S and platinized FTO cathodes under simulated AM 1.5, 100 mW cm^{-2} illumination.

Table 5.2 summarizes the *j-V* data of solar cells made with 7CdSe, $6CdS_xSe_{1-x}$, and 5CdS/5CdSe-sensitized SnO_2 electrodes. Similar to the CdSe-sensitized TiO_2 electrode as presented in Chapter 3, the SnO_2/CdSe cells also demonstrate better j_{sc}

and V_{oc}, hence a better power conversion efficiency of 3.78% was achieved using platinized FTO cathode under simulated AM 1.5 100 mW cm^{-2} illumination. The use of Cu_2S cathode greatly enhances the photocurrent density, 18.57 mA cm^{-2} owing to superior IPCE of cell, especially, in the long wavelength region, which leads to a power conversion efficiency of 4.37% under AM 1.5 100 mW cm^{-2} illumination. However, the performance of CdSe-sensitized SnO_2 cells was deteriorated when CdS was used as an underlayer (cascaded CdS/CdSe) because of impaired photocurrent density and photovoltage. Cells made with solid solution $6CdS_xSe_{1-x}$-sensitized SnO_2 electrodes with platinized FTO and Cu_2S cathodes show even lower efficiency than that of CdSe and cascaded CdS/CdSe-sensitized SnO_2-based cells, which will be explored by IS measurements.

Table 5. 2 Characteristics of 7CdSe, $6CdS_xSe_{1-x}$, and 5CdS/5CdSe-sensitized SnO_2-based solar cells with platinized FTO and Cu_2S cathodes under simulated AM 1.5, 100 mW cm^{-2} illumination.

Photoanode	*Sensitizer*	*Cathode*	V_{oc} *(V)*	j_{sc} *(mA* cm^{-2}*)*	*ff (%)*	*η (%)*
SnO_2	7CdSe	Pt	0.521	16.63	43.56	3.78
	7CdSe	Cu_2S	0.523	18.57	44.96	4.37
	$6CdSe_xSe_{1-x}$	Pt	0.494	15.75	40.62	3.16
	$6CdSe_xSe_{1-x}$	Cu_2S	0.505	16.86	38.07	3.24
	5CdS/5CdSe	Pt	0.516	16.13	42.50	3.53

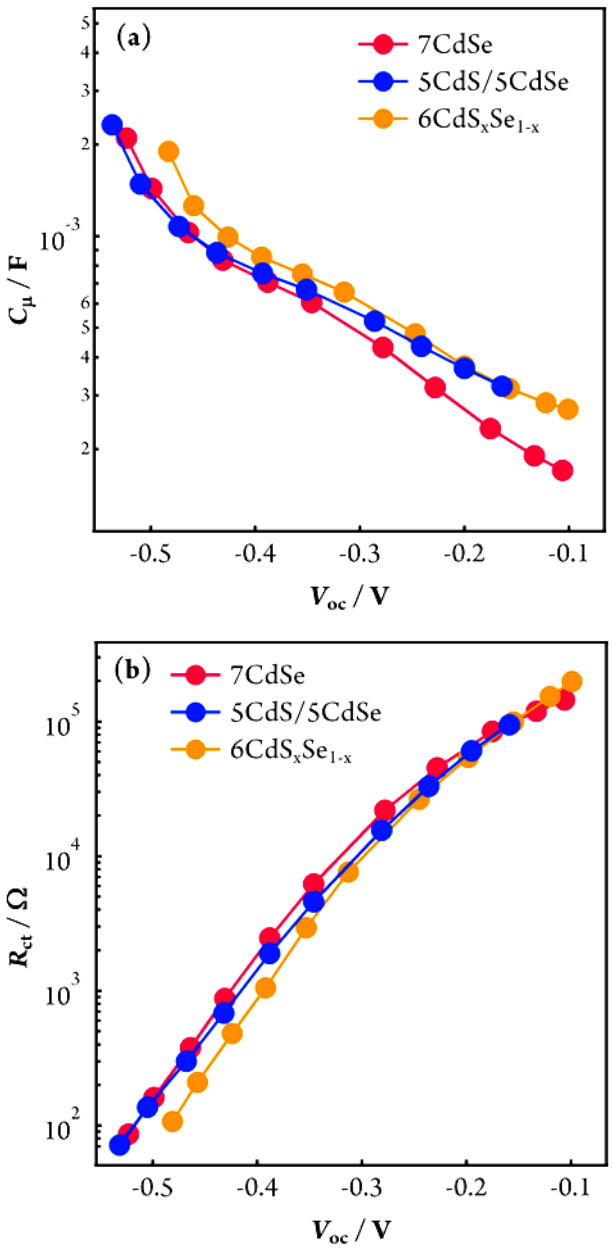

Figure 5. 9 Impedance fitting results of 7CdSe, 5CdS/5CdSe and $6CdS_xSe_{1-x}$-sensitized SnO_2 cells utilizing a simple model consisting of two RC circuits as shown in Figure 5.7. (a) Plots of C_μ versus V_{oc}, and (b) R_{ct} versus V_{oc}.

The charge transport characteristics of these cells made with platinized FTO cathode were investigated by IS measurement. As shown in Figure 5.9 (a), the C_μ-V_{oc} plot is approximately identical for 7CdSe and 5CdS/5CdSe-sensitized SnO_2 electrodes, implying approximately the same quasi-Fermi level; thus R_{ct} of these cells

can be compared directly. The R_{ct}-V_{oc} plot shows that the cell made with 7CdSe-sensitized SnO_2 electrode has slightly larger recombination impedance, than that of 5CdS/5CdSe and 6CdS_xSe_{1-x}-sensitized SnO_2-based cells (Fig. 5.9(b)), which is consistent with the slightly higher V_{oc} of the 7CdSe cell as compared to the other two cells.

5.9 Summary

CdSe and CdS/CdSe-sensitized SnO_2 solar cells exhibited photocurrent densities of up to 18.57 mA cm^{-2} and 17.40 mA cm^{-2}, respectively, under simulated AM 1.5, 100 mW cm^{-2} illumination. Consistent with the high photocurrent density, an IPCE of close to 80% over almost the entire visible spectral region is observed, implying highly efficient charge separation and collection. Open-circuit photovoltage is similar to that obtained by TiO_2-based SSCs, despite the much more positive CBM of SnO_2. Impressive overall power conversion efficiencies of up to 4.37% (using SnO_2/7CdSe) and 3.68% (using SnO_2/5CdS/5CdSe) were achieved, making nanostructured SnO_2 a rival to TiO_2 for use in SSCs.

A detailed comparison between SnO_2 and TiO_2 photoanodes reveals SnO_2 can be considered a superior material to TiO_2 in many respects, owing to higher recombination resistances, faster charge transport, and more efficient charge separation. However, the efficiency of SSCs employing SnO_2 may be limited by the relatively low conduction band energy compared with TiO_2. To overcome this problem we anticipate that control of surface dipoles at the various interfaces (*e.g.*, SnO_2/CdSe, ZnS/electrolyte, *etc.*) will be important in engineering band edge positions with respect to the electrolyte redox level and consequently improving V_{oc}.

Another strategy to improve conversion efficiency might involve replacement of the S^{2-}/S_x^{2-} electrolyte with one possessing a more positive redox potential, however, this approach will almost certainly lead to changes in sensitizer regeneration rate and charge recombination rate, which may or may not be beneficial to device performance.

6 PbS/CdS-Sensitized Mesoscopic SnO_2 Solar Cells for Enhanced Infrared Light Harnessing

6.1 Introduction

Narrow band gap semiconductors have been attracting great attention as panchromatic sensitizers in SSCs owing to their broad spectra of light absorption.[15,40,70,141-146] Among the various narrow band gap semiconductors, lead sulfide (PbS) has a band gap energy of 0.41 eV in the bulk material, which can be easily tuned to harvest photons of different energies by reducing the size as a result of quantum confinement effect.[147,148] The capability of light absorption from visible to near infrared region in the solar spectrum as well as the inherent high extinction coefficient make PbS an important sensitizing material for SSC applications.[34,71]

In addition, owing to the quantized discrete band structures one salient property of PbS nanocrystals as light absorber is the capability for multiple exciton generation. Internal quantum yield greater than unity has recently been reported by Sambur *et al.* in PbS QD-sensitized single crystal anatase TiO_2 cells utilizing a S^{2-}/S_x^{2-} electrolyte, paving the way of achieving power conversion efficiency beyond the Shockley-Queisser limit.[15] While promising, the reported efficiency of liquid junction SSCs utilizing PbS is still much lower than those using semiconductor sensitizers of wider band gap, for instance, CdSe, $CuInS_2$, *etc*.[63,78,145,149,150] Therefore, efforts are continuously being taken to improve the device performance by optimizing the conditions for sensitizer synthesis, employing counter electrodes with better catalytic activity, and exerting rigorous interfacial engineering, *etc.*

In PbS-sensitized solar cells, a type-II band alignment between PbS and metal oxide is desired to facilitate charge separation, where both the conduction and valence bands of the narrow band gap semiconductor sensitizer are higher in energy than the corresponding band energies of the underlying metal oxide, so that the generated electrons and holes in PbS would separate rapidly by transferring electrons into the conduction band of metal oxide (*i.e.*, TiO_2). As such, the conduction band position and hence the size of PbS are critical to achieve efficient charge separation, and only quantum sized PbS nanocrystals with sufficient offset of conduction band energy to that of metal oxide could be used, which on the other hand constraints the harvesting of long wavelength photons as a result of band gap augmentation.

In addition, compositional synthesis has been emerging as an alternative approach to tune the light absorption and energetics of semiconductor sensitizers, where the optical band gap can be feasibly varied by changing the compositions of resulted semiconductors.[111,151] These composition-tunable semiconductors can be easily made if the constituents or their precursors are miscible at atomic level provided that they have sufficiently similar crystal structure and bond length for homogeneous mixture formation. Otherwise, very likely they will form segregated alloys or gradient nanocrystals.[100,102] Ternary alloy $Cd_xPb_{1-x}S$ has been synthesized *via* chemical bath deposition by incorporating Cd^{2+} into PbS matrix to modify the optical property. Although the value of x is limited to 0.15, it provides great flexibility in tuning the spectrum of PbS.[152-155]

Alternatively, instead of reducing the dimension of PbS or using $Cd_xPb_{1-x}S$ alloy, metal oxides with lower CBM could be employed to feasibly improve charge separation without reducing the width of the spectrum of the sensitizer. For instance, a

favorable band alignment between TiO_2 and PbS could only occur if sufficiently small PbS QDs are used as sensitizer, while ultrafast transient absorption measurement revealed that identical PbS QDs could easily inject electrons into SnO_2 owing to the lower CBM of the latter.[20] As shown in Chapter 5, much enhanced charge separation efficiency has also been observed in CdSe-sensitized SnO_2 solar cells with close to unity external quantum efficiency.[48] Considering the much higher electron mobility and wider optical band gap, SnO_2 is deemed to be an ideal photoanodic material for PbS-sensitized mesoscopic solar cells, especially for the unambiguous observation of multiple exciton generation with over unity external quantum yield.[15,16,156,157]

In this study, mesoscopic SnO_2 was employed and examined thoroughly for the first time as the photoanode in PbS-sensitized solar cells with an aqueous S^{2-}/S_x^{2-} electrolyte to exploit the capability of panchromatic PbS/CdS sensitizer. Both cascaded and alternate PbS/CdS layers were deposited onto SnO_2 by SILAR to evaluate their photovoltaic performance.[28,78,145] Optical absorption spectroscopy, TEM, XRD, *j*-V and IPCE measurement were conducted to understand the growth mechanism of sensitizers and the performance of these sensitized electrodes in solar cells. The cascaded *n*PbS/*n*CdS was found to be better than the alternate *n*(PbS/CdS) irrespective of metal oxide electrodes used (*n* is the number of SILAR cycles). An overall power conversion efficiency 2.23% with an unprecedented photocurrent density of 17.38 mA cm^{-2} was attained with PbS-sensitized SnO_2 solar cells using aqueous S^{2-}/S_x^{2-} electrolyte and a Cu_2S cathode, under simulated AM 1.5, 100 mW cm^{-2} illumination.

6.2 Preparation of cascaded *n*PbS/*n*CdS and alternate *n*(PbS/CdS)-sensitized mesoscopic SnO_2 and TiO_2 electrodes

The mesoscopic SnO_2 electrodes (pre-treated with $TiCl_4$ solution) were prepared following the described procedure in Section 2.1 in Chapter 2. For comparison, TiO_2 (Degussa, P25) nanoparticles were also used to make paste and electrodes. It is worthwhile to mention that hole blocking and scattering layers were not used either in SnO_2 or TiO_2 electrodes. After masking the bare FTO with Kapton tape, leaving the mesoscopic SnO_2 or TiO_2 electrodes (0.6 cm diameter) uncovered, they were sensitized with cascaded *n*PbS/*n*CdS sensitizer previously reported by a few groups,[28,45,145] or alternate *n*(PbSCdS), which was described in Section 2.3.3. A ZnS passivation layer was deposited onto both sensitizer coated SnO_2 electrodes by SILAR following the procedure described in Section 2.4 in Chapter 2.[45,48] For comparison, TiO_2 electrodes ~10 µm were used where the rest of the fabrication procedure was identical to that used for cascaded *n*PbS/*n*CdS and alternately deposited *n*(PbS/CdS)-sensitized SnO_2 electrodes.

6.3 Morphological characterization of PbS/CdS-sensitized SnO_2 nanoparticles

Figure 6.1 shows the HRTEM image of cascaded *4*PbS/*4*CdS and alternate *4*(PbS/CdS) deposited on SnO_2 electrodes. The SnO_2 nanoparticles consist of approximately 20 nm crystal grains, which show clear lattice fringes with *d*-spacing 0.335 nm corresponding to a crystal plane of (110) indexed to the tetragonal rutile structure (JCPDS No. 72-1147). Due to the high surface energy of PbS with respect to the underlying metal oxide in the depositing medium, scattered nanocrystals of hemispherical shape were observed at the edge of SnO_2 crystal grains, which is

somewhat similar to the growth of PbS on TiO_2 electrodes as reported by a few groups previously.[40,145]

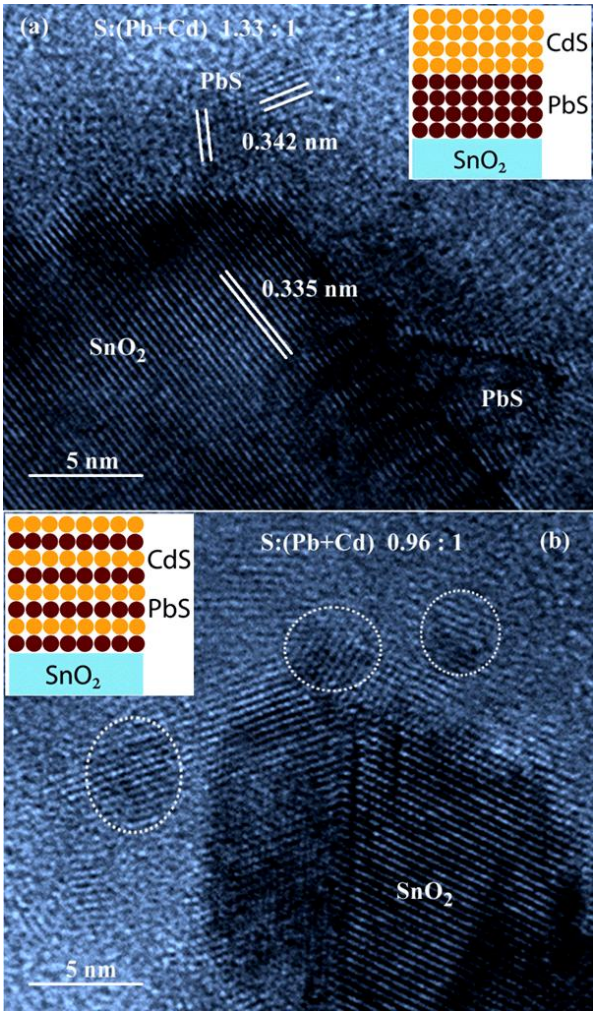

Figure 6. 1 HRTEM images of SnO_2 nanoparticles coated with (a) cascaded *4*PbS/*4*CdS, and (b) alternate *4*(PbS/CdS) sensitizers by SILAR. The insets show the respective configuration of cascaded and alternate PbS/CdS on SnO_2 during their deposition by SILAR.

The lattice fringes corresponding to CdS overlayers on PbS QDs were not seen in cascaded *4*PbS/*4*CdS electrodes, implying that the as-grown CdS is amorphous in nature (Fig. 6.1(a)).[48] Similarly, scattered nanocrystallites surrounding the SnO_2 nanoparticles in the alternate *4*(PbS/CdS) deposited electrodes are observed while the

lattice fringes show slightly smaller *d*-spacing compared to the cascaded electrodes (Fig. 6.1(b)). EDS elemental analysis of the as-deposited sensitizers shows that the atomic ratio S/(Pb+Cd) was ~1.33 in the cascaded *4*PbS/*4*CdS electrodes, indicating that on average it was sulfur rich and broadly consistent with previous reports by cation exchange method,[158] and a ratio ~0.96 was found for the alternate *4*(PbS/CdS) electrodes, indicating that as a whole, it was rather close to the stoichiometric composition.

6.4 Structural characterization of PbS/CdS-sensitized SnO_2 nanoparticles

Figure 6.2 shows the XRD patterns of PbS/CdS-sensitized TiO_2 and SnO_2 electrodes before and after heat-treatment at 350 °C. The as-prepared cascaded *4*PbS/*4*CdS electrodes show Bragg diffraction peaks at 30.15º, 42.85º and 51.50º (shown by vertical dashed lines), indicating the presence of crystallites of cubic PbS (Fig. 6.2(a)). However, the alternate layer deposited electrodes *4*(PbS/CdS) show a small shift (~0.30º) towards higher 2θ compared with the former electrodes (Fig. 6.3 (a-d)). Hodes *et al.* suggested that this small displacement of diffraction peaks might be caused by strain effect due to nearly ambient deposition condition.[155] However, incorporation of Cd^{2+} (smaller ionic radii) into the crystalline PbS matrix by replacing the relatively bigger Pb^{2+} in the as-prepared samples might also cause the shift.[159]

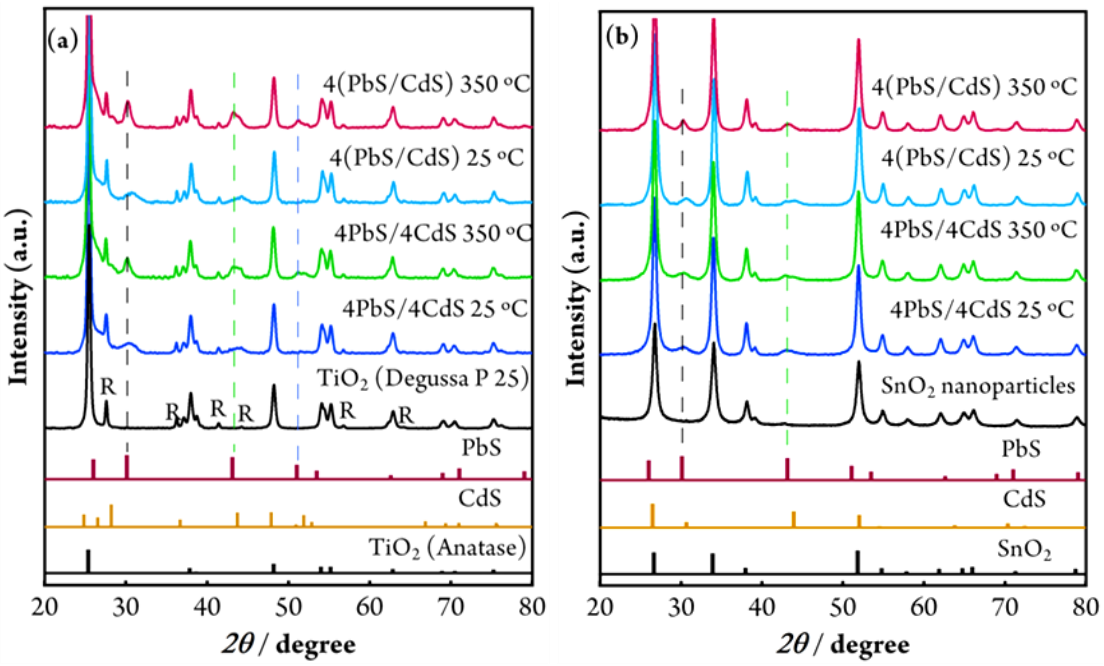

Figure 6. 2 XRD patterns of the cascaded *4*PbS/*4*CdS and alternate *4*(PbS/CdS)-sensitized nanocrystalline (a) TiO_2, and (b) SnO_2 electrodes. The standard peaks for SnO_2, anatase TiO_2, rutile (R) phase in TiO_2 (Degussa P25), wurtzite CdS and cubic PbS are also included for reference.

Pentia *et al.* have reported the formation of solid solution ($Cd_xPb_{1-x}S$, $0 \leq x \leq 1$) by chemical bath deposition method where it can be formed either at low Cd^{2+} and high Pb^{2+} (Cd^{2+} in PbS matrix) or high Cd^{2+} and low Pb^{2+} content (Pb^{2+} in CdS matrix).[160] In our study, a non-stoichiometric ratio of Cd/Pb = 0.23 was found from EDS elemental analysis, and the value of *x* in $Cd_xPb_{1-x}S$ was calculated to be 0.19, which is slightly greater than the threshold value 0.15 at which the phase separation happens as reported by Hodes *et al.*[155] While the as-prepared alternate layer sample exhibits only one set of broad peaks, the evolution of the XRD patterns reveals that the material likely separates into a mixture of two separate phases after annealing at 350 °C (Fig. 6.2).

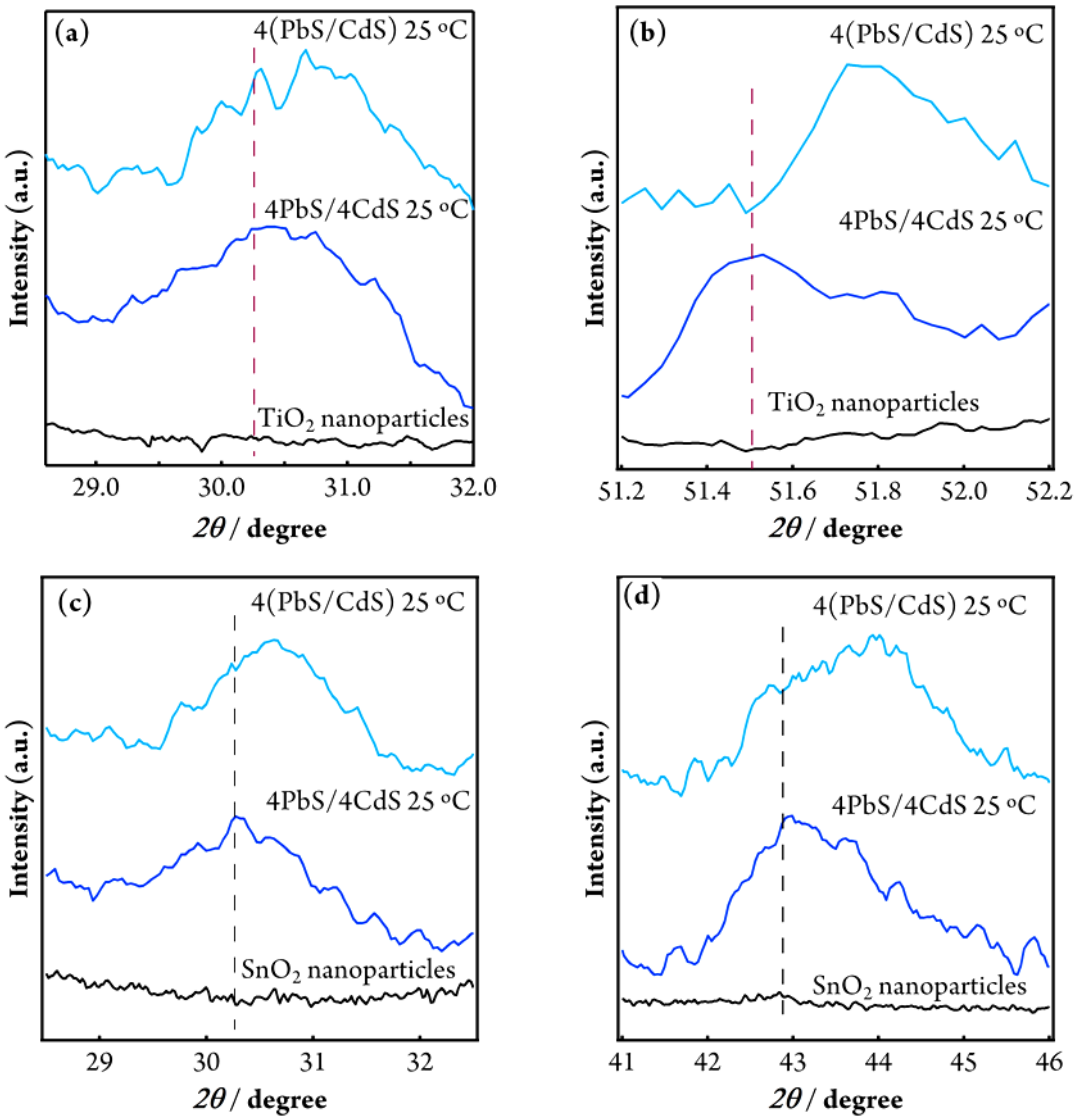

Figure 6. 3 Slowly scanned XRD patterns of the as-deposited cascaded *4*PbS/*4*CdS and alternate *4*(PbS/CdS)-sensitized nanocrystalline TiO_2 (a, b), and SnO_2 (c, d).

In addition, although small nanocrystallites were observed on SnO_2 from HRTEM measurement (Fig. 6.1), both cascaded and alternate PbS/CdS only reveal very small diffraction peaks on SnO_2 even after heat treatment. Considering more PbS/CdS was actually deposited onto SnO_2 as evidenced by the optical measurement in Figure 6.4, it is inferred that the growth of crystalline PbS/CdS is suppressed on the surface of SnO_2, plausibly as a result of unfavorable surface energy for the growth of

crystal grains, which is well distinct to that of TiO_2. These as-prepared electrodes were used directly for optical measurements, device fabrication and characterizations in the subsequent sections.

6.5 Optical properties of the sensitized electrodes

Figure 6.4 (a) and (b) show the optical density spectra of 5.5 μm thick SnO_2 electrodes coated with cascaded *n*PbS/*4*CdS and alternate *n*(PbS/CdS) (*n* = 1-5), respectively. With increasing SILAR deposition cycles of PbS, the spectra of both electrodes shift to longer wavelength gradually, with the absorption edge extending to 1600 nm within the measured wavelength range. While the peak absorbance between 400 and 600 nm is comparable for both cascaded and alternate layer deposited electrodes, the former presents much higher OD at longer wavelength than the latter, indicating the growth of PbS in the cascaded structure is favoured and accordingly the size should be larger. This is understandable considering that the growth of PbS could be easily disrupted by the subsequent deposition of CdS in each alternate layer. As a result, the crystallinity of alternate *4*(PbS/CdS) would be deficient compared with the cascaded *4*PbS/*4*CdS electrodes. Regardless of the SILAR deposition mode, no characteristic excitonic peak could be observed in all the OD spectra, suggesting a dispersed size distribution of the deposited semiconductor nanocrystallites (Fig. 6.4). Optical density spectra were collected in a transmission mode utilizing single beam in a Shimadzu UV-vis-NIR spectrophotometer (Solidspec-3700) at room temperature.

For comparison, TiO_2 electrodes were also sensitized with both cascaded *n*PbS/*4*CdS and alternate *n*(PbS/CdS). As the absorption spectra revealed in Figure 6.4(c) and (d), the absorbance was found significantly lower than that of the SnO_2

electrodes. In addition, for the same SILAR deposition cycles the PbS-sensitized TiO_2 has much blue shifted spectrum compared with that of SnO_2.

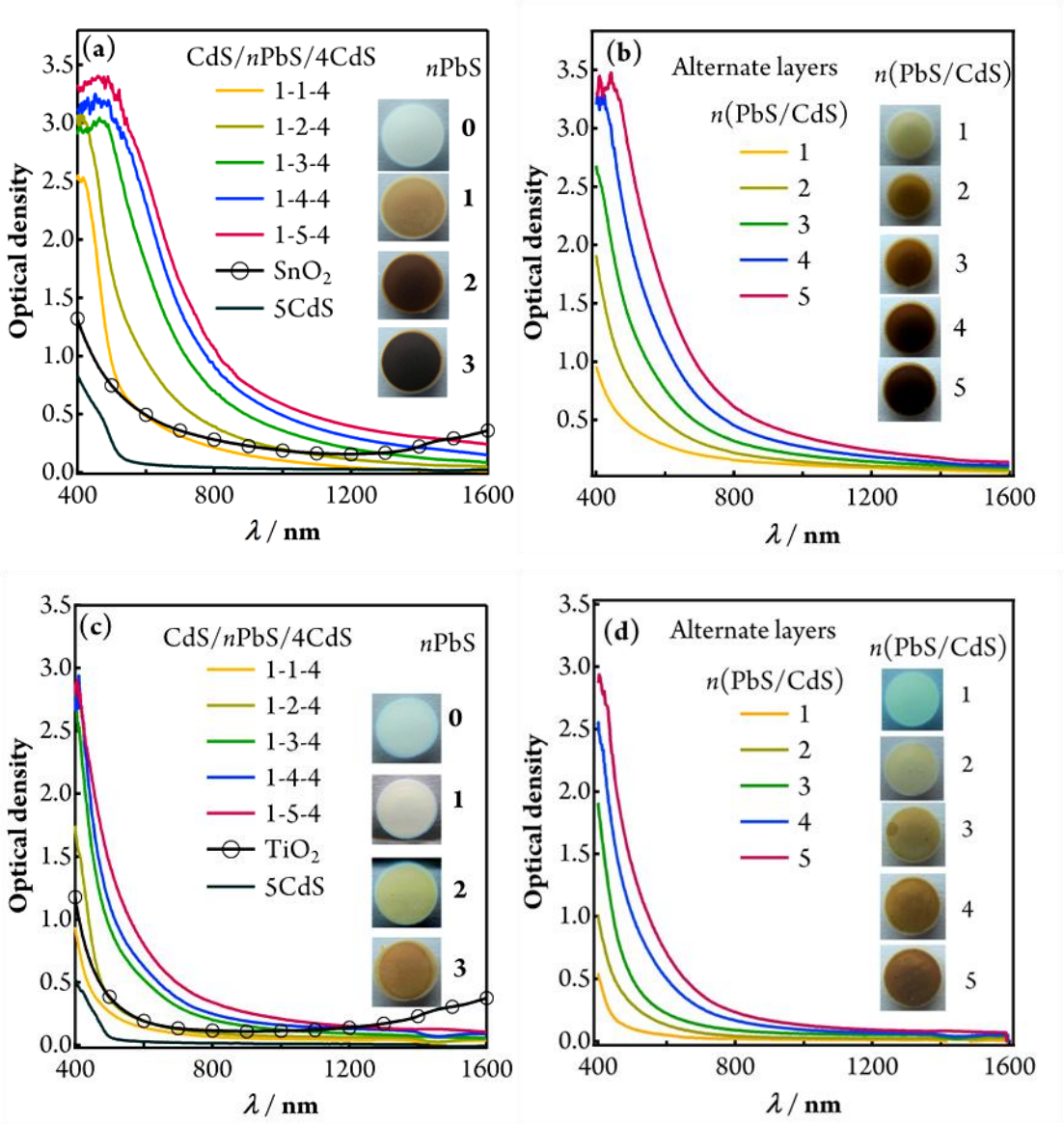

Figure 6. 4 UV-Vis optical density spectra of (a) cascaded CdS/*n*PbS/*4*CdS, (b) alternate *n*(PbS/CdS) (*n* =1-5) deposited on SnO_2 electrodes (5.5 μm); and the spectra of TiO_2 electrodes (5.5 μm) coated with (c) CdS/*n*PbS/*4*CdS and (d) alternate *n*(PbS/CdS) (*n* =1-5). The inset photographs in (a, c) show the PbS-coated SnO_2 and TiO_2 electrodes, respectively and those in (b, d) show the *n*(PbS/CdS)-coated SnO_2 and TiO_2 electrodes, respectively. The absorption spectra of substrates are shown by solid black line with circle mark in (a) and (c), and all other spectra represent the light absorption of the sensitizers as the substrate absorption was subtracted from the light absorption of corresponding electrodes.

As the photographs shown in the inset of Figure 6.4(a), the colour of the sensitized SnO_2 electrodes turns from yellow ochre in the 1st cycle to dark brown after 3 cycles deposition of PbS. In contrast, the sensitized TiO_2 electrodes have very pale colour indicating much less amount of PbS was actually deposited (Fig. 6.4(c)). Several recent studies have revealed that the growth of PbS on TiO_2 by SILAR deposition is not favoured and only gives rise to very scattered hemispherical shaped QDs. To enhance the reaction kinetics of PbS on TiO_2, surface treatment with chemicals such as NH_4F and HF have been carried out to improve PbS deposition by Samadpour *et al.*[149]

In contrast, the inherently more favorable growth of PbS on SnO_2 would be of great advantage for efficient light harvesting in the subsequent photovoltaic applications. Figure 6.5 shows the OD spectra of one CdS buffer layer plus *n*PbS layer (*n* = 1-5) (denoted as CdS/*n*PbS)-sensitized metal oxides are also found to follow the same trend as Figure 6.4, implying that one SILAR cycle of the CdS cannot make a conformal layer on both metal oxides.

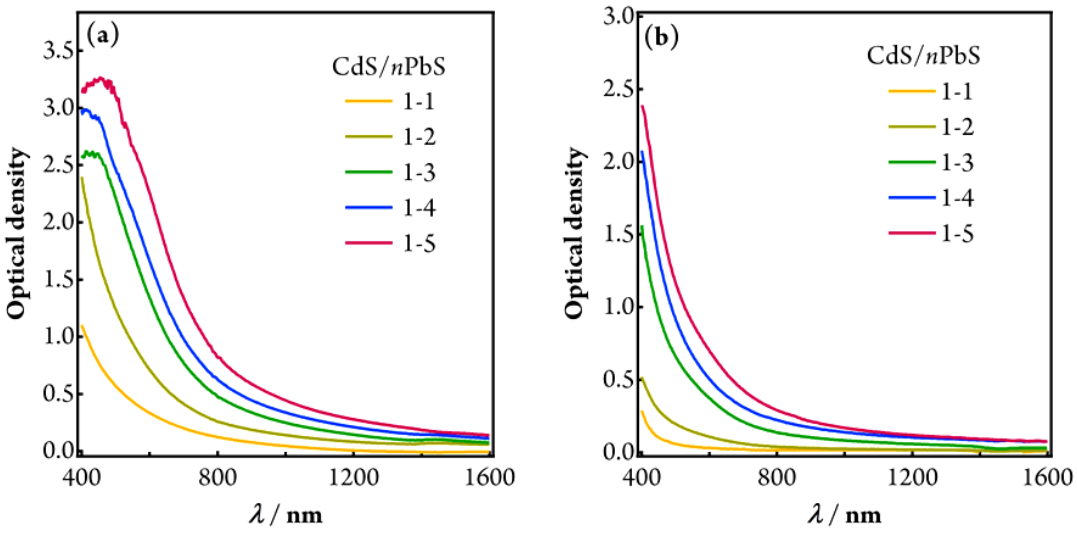

Figure. 5 Optical density spectra of SILAR deposited CdS/*n*PbS sensitizers (*n* = 1-5) on 5.5 µm thick (a) SnO_2 electrodes and (b) TiO_2 electrodes. All these spectra represent the light absorption of the sensitizers as the substrate absorption was subtracted from the light absorption of corresponding electrodes.

6.6 Band alignment of PbS/CdS with SnO_2 and TiO_2

In SSCs, as the amount of semiconductor sensitizer on metal oxide is too small to accommodate a significant band bending, the metal oxide/sensitizer interface region will be crucial for charge separation.[161] In order for efficient charge separation, a staggered band alignment with both the HOMO and LUMO levels of semiconductor sensitizers higher than the valence and conduction band edges of the underlying wide band gap semiconductor is desired in SSCs. Figure 6.6 shows the favorable band alignment of PbS QDs on SnO_2 and TiO_2. As the conduction band edge of SnO_2 is significantly lower than that of TiO_2, it is anticipated that for PbS QDs with similar size the carrier injection in SnO_2 will be much faster than that in TiO_2. To ensure efficient charge separation in TiO_2, PbS QDs with much smaller size would be required, which however compromises light harvesting due to a band gap enlargement.

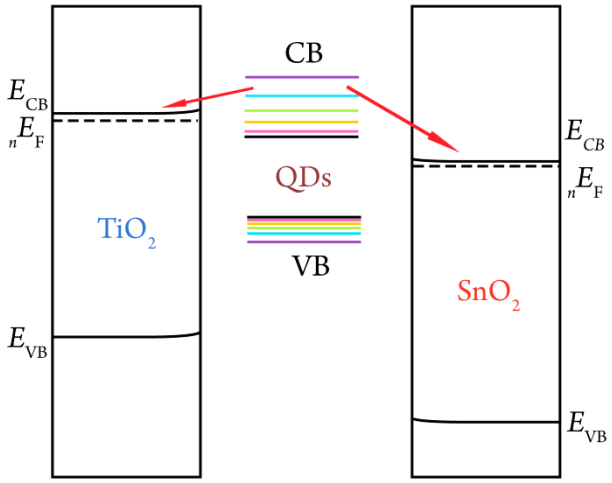

Figure 6. 6 Energy-level alignment of the TiO_2 and SnO_2 conduction band with different sized PbS QDs. The lower CBM of SnO_2 facilitates faster electrons injection from PbS QDs.

6.7 Photovoltaic characteristics

To investigate the photovoltaic performance of these sensitizers on SnO_2 and TiO_2 electrodes, sandwich type thin layer cells were fabricated with Cu_2S on brass as the cathode and polysulfide electrolyte as the hole transporter. A thin ZnS passivation layer (2 cycles) was deposited onto the sensitized electrode by the same SILAR method to prevent charge recombination at the electrode and electrolyte interface.[49,50] As the IPCE spectra shows in Figure 6.7(a), both cascaded and alternate PbS/CdS-sensitized SnO_2 electrodes exhibit a photocurrent response extending to the near infrared region, with a maximum IPCE of ~50% at 390 nm and an average IPCE of ~10% at 1100 nm irrespective of the electrode structures. In comparison, the TiO_2-based SSCs has a peak IPCE of ~40% at 390 nm, which however drops steeply at longer wavelength with an IPCE of only ~2% at 1100 nm. The less efficient quantum yield of TiO_2-based SSCs as compared to that of SnO_2 is likely a result of inefficient charge injection as revealed by few groups.[20,132] The lower CBM of SnO_2 is believed to greatly facilitate the injection of electrons from the relatively lower lying LUMO of sensitizers, which becomes more apparent at longer wavelength as the distinct wavelength dependence of IPCE between these two metal oxides indicated in Figure 6.7(a).[124] In addition, the cascaded *3*PbS/*4*CdS always presents higher IPCE than that of the alternate *4*(PbS/CdS) on the same metal oxide electrode, implying superior charge separation of the former configuration.

The $TiCl_4$ post-treatment of SnO_2 was found to be critical to drastically increase the performance of the cells. A similar phenomenon was also observed for SnO_2/CdSe cells.[23] Snaith *et al.* have shown in a recent study that islands or terraces consisting of 1-2 nm sized TiO_2 nanocrystallites are formed on $TiCl_4$ treated SnO_2 upon heating at 500 °C, which were found to be beneficial for passivating the surface states and the

overall performance of bulk heterojunction dye-sensitized solar cells.[26] It is believed that the role of $TiCl_4$ treatment is similar for semiconductor-sensitized SnO_2 solar cells while unambiguous understanding requires systematic studies.

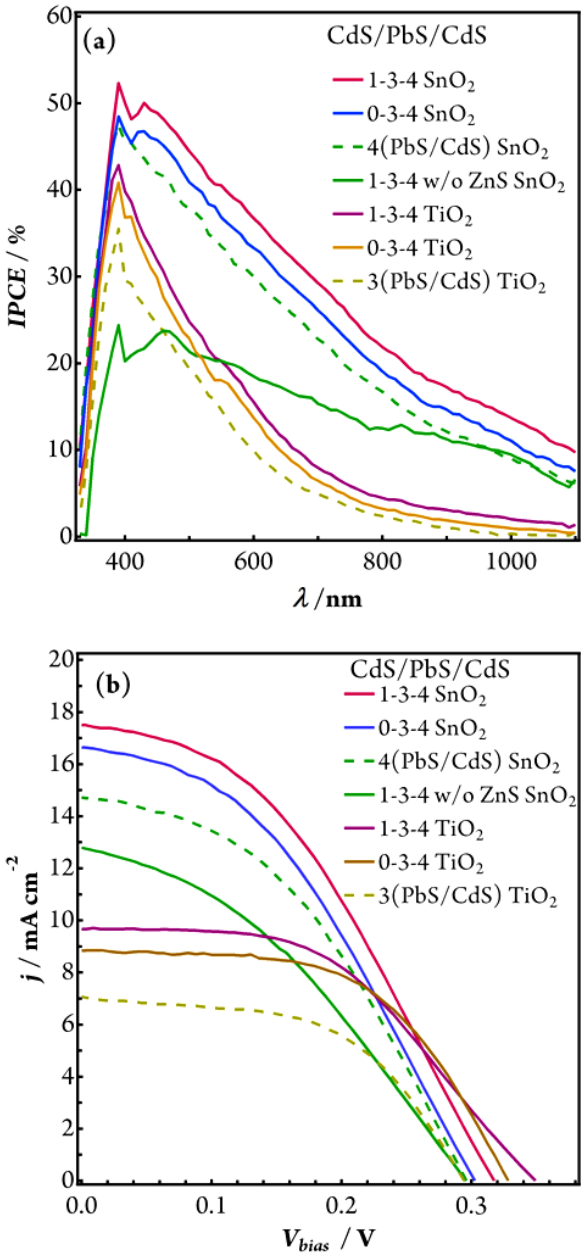

Figure 6. 7 (a) IPCE spectra and (b) *j-V* characteristics of cells utilizing cascaded and alternate PbS/CdS-sensitized SnO_2 and TiO_2 electrodes. Cu_2S on brass and S^{2-}/S_x^{2-} electrolyte were used as the counter electrode and hole scavenger, respectively.

While a CdS buffer layer was found to be redundant in CdSe-sensitized TiO_2- and SnO_2-based solar cells presented in Chapter 3 and 5, respectively, it was observed here that a thin CdS buffer layer underneath the cascaded PbS/CdS sensitizer is always beneficial to the photovoltaic performance of both SnO_2 and TiO_2-based SSCs. As shown in Figure 6.7 (b), both photocurrent and open circuit voltage were noticeably increased when one layer of CdS was coated prior to PbS deposition in cascaded *3*PbS/*4*CdS electrodes. Considering the SILAR method produces cluster-like PbS quantum dots on SnO_2 or TiO_2, it is believed that deposition of a thin layer CdS would passivate the surface states and block the direct contact of the exposed metal oxide surface with the surrounding electrolyte. As a result, charge recombination between injected electrons in metal oxide and acceptor species (S_x^{2-}) in the S^{2-}/S_x^{2-} electrolyte would be greatly suppressed. This is supported by the recent study of Guijarro *et al.*, who found that coating TiO_2 with an analogue material of CdS—CdSe greatly increased the charge transfer resistance at TiO_2/electrolyte interface.[49] In addition, while PbS is widely studied as a panchromatic sensitizer for efficient light harvesting, it is also a good electrocatalyst toward the reduction of S^{2-}/S_x^{2-} electrolyte,[61] and has been employed as counter electrode in this electrolyte based SSCs.[62] This however raises the concern that the presence of PbS as sensitizer may catalyze the recombination reaction at photoelectrode/electrolyte interface.

As reported by Lee *et al*, a ZnS passivation layer is required to hinder the backward electron flow from PbS to the oxidized species in S^{2-}/S_x^{2-} electrolyte.[78] A similar phenomenon was observed here. As shown in Figure 6.7(a), although 4 layers of CdS were coated on top of PbS, peak IPCE of the cascaded *3*PbS/*4*CdS sensitized-SnO_2 still drops by almost 50% in the absence of ZnS passivation layer on the outmost surface. As a consequence, both photocurrent and photovoltage deteriorate

compared with the same electrode treated with two layers of ZnS (two SILAR cycles). In addition, it is interesting to note that the enhancement of IPCE for the ZnS-treated samples is mainly contributed by short wavelength photons (400~800 nm), while only a marginal increment was observed at long wavelength. As ZnS has negligible light absorption in this wavelength range, the distinct wavelength-dependent enhancement of IPCE could be rationalized by the improved separation of charge carriers generated in *4*CdS layer, which only absorbs short wavelength photons. The presence of a ZnS passivation layer on top of CdS greatly suppresses the recombination of electrons residing in CdS with acceptor species in the electrolyte.[37] It is anticipated that the cascaded structure of PbS sensitizer with an underlying CdS buffer layer and overlying CdS overlayers (as buffer layer for the subsequent ZnS deposition), along with the ZnS passivation layer would greatly eliminate interfacial charge recombination and improve the photovoltaic performance of PbS-sensitized SnO_2-based SSCs.

Table 6. 1 Characteristics of cascaded and alternate PbS/CdS-sensitized SnO_2- and TiO_2-based solar cells under simulated AM 1.5, 100 mW/cm^2 illumination. The thickness of both SnO_2 and TiO_2 electrodes is ~10 μm.

Photoanode	*Sensitizer*	V_{oc} *(V)*	j_{sc} *(mA cm^{-2})*	*ff (%)*	*η (%)*
SnO_2	1-3-4	0.318	17.38	40.21	2.23
	0-3-4	0.303	16. 55	39.95	2.00
	1-3-4 w/o ZnS	0.295	12.75	36.61	1.40
TiO_2	1-3-4	0.349	9.72	48.43	1.64
	0-3-4	0.328	8.93	55.30	1.61
SnO_2	4(PbS/CdS)	0.297	14.71	41.81	1.82
TiO_2	4(PbS/CdS)	0.295	7.08	53.34	1.11

The effect of film thickness on the cell performance was investigated by varying the thickness of mesoscopic SnO_2 films and eventually an optimum thickness for SnO_2 electrodes was found to be ~10 μm. For TiO_2-based SSCs, 10 μm thick electrodes were also used to make comparison. Table 6.1 summarizes the data of both SnO_2 and TiO_2-based SSCs. As expected the SnO_2 electrodes exhibit much higher short-circuit photocurrents as compared to TiO_2 electrodes irrespective of the sensitizer configurations, whereas the V_{oc} of SnO_2-based SSCs is only slightly lower than the TiO_2-based SSCs despite the far more positive CBM of SnO_2 (*ca.* 300-500 mV). The reason for the small difference in photovoltage could be twofold: firstly, charge recombination in SnO_2-based SSCs is plausibly slower than that in TiO_2 cells, which has been proved in CdS/CdSe-sensitized cells by careful impedance measurement. As a result, the V_{oc} of CdS/CdSe-sensitized SnO_2 cells is only *ca.* 26—56 mV lower compared with TiO_2 cells as shown in Section 5.6 in Chapter 5,[48] which is similar to the present study.

In addition, the photocurrent of SnO_2-based SSCs is almost two times as high as that of TiO_2 cells. Hence higher electron concentration in SnO_2 is expected, which may cause an upward shift of the electron quasi-Fermi level (closer to CBM) with respect to the redox potential of S^{2-}/S_x^{2-} electrolyte, further offsetting the V_{oc} difference. The best device was obtained with cascaded CdS/*3*PbS/*4*CdS-sensitized SnO_2 electrodes, yielding j_{sc} = 17.38 mA cm^{-2}, V_{oc} = 0.318 V, fill factor = 40.21%, and η = 2.23% under simulated AM 1.5, 100 mW/cm^2 illumination, which represents one of the highest power conversion efficiency achieved so far for PbS-sensitized liquid junction solar cells. In comparison, the alternate *4*(PbS/CdS)-sensitized SnO_2 cells exhibit relatively low photocurrent and photovoltage and consequently much lower power conversion efficiency presumably because of increased carrier

recombination kinetics as observed for CdS_xSe_{1-x}-sensitized TiO_2 solar cells described in Section 4.6 in Chapter 4.

The photovoltaic performance of cells made with TiO_2 electrodes suffered from low photocurrent due to less efficient charge injection as a result of the relatively high CBM of TiO_2 (Fig. 6.6, and 6.7). The best device was obtained with cascaded CdS/*3*PbS/*4*CdS as sensitizer, yielding j_{sc} = 9.72 mA cm^{-2}, V_{oc} = 0.349 V, fill factor = 48.43%, and η = 1.64%. Interestingly, the alternate *n*(PbS/CdS) was prone to peel off from TiO_2 electrodes and only a maximum 3 SILAR cycles could be reproducibly obtained on TiO_2, which resulted in an even lower power conversion efficiency as listed in Table 6.1. The performance of these TiO_2 cells are notably lower than those reported by Braga *et al.*, which could collectively be a result of different electrode structure and device fabrication procedure used in these two studies. For instance, no scattering and blocking layers were employed in the TiO_2 electrodes in the present study, in order for fair comparison with the SnO_2 electrodes. In addition, we have attempted to explore the roles of the two different sensitizer configurations and their correlations to the device performance by impedance spectroscopic measurements. Considering Cu_2S coated brass is not a stable counter electrode in S^{2-}/S_x^{2-} electrolyte,[61,79] platinized FTO was used as counter electrode. However, unlike the CdSe-sensitized devices, platinized counter electrode in PbS-sensitized cells suffers from extremely large interfacial charge transfer resistance for unknown reason, which makes the impedance spectroscopic study very difficult.

While encouraging, the quantum efficiency of PbS-sensitized SnO_2 solar cells is still much lower than unity compared with the CdSe-sensitized counterparts (Fig. 5.8(a) in Chapter 5). The maximum internal quantum efficiency is determined to be

only ~70% by considering the optical loss of the cell (Fig. 6.8). Insightful understanding of the loss mechanism would be of paramount importance for further improving the device performance and ultimately achieving charge carrier multiplication in sensitized mesoscopic solar cells considering the superb properties of SnO_2 observed herein.

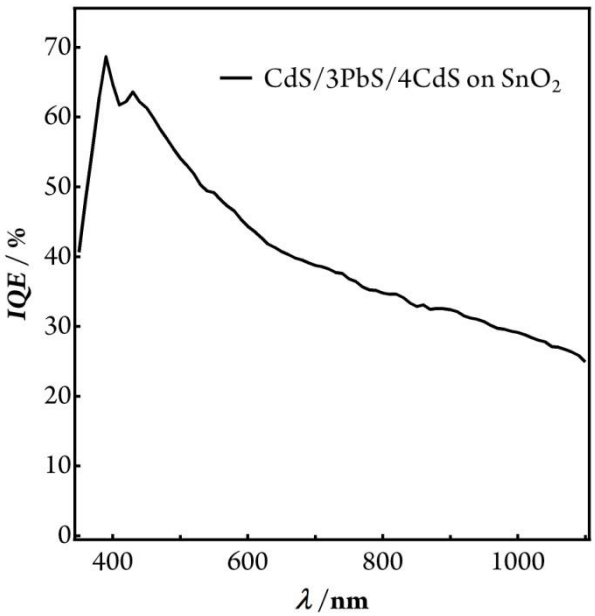

Figure 6. 8 Internal quantum efficiency (IQE) of a CdS/3PbS/4CdS-sensitized SnO_2 solar cell.

6.8 Summary

Mesoscopic SnO_2 electrodes were examined thoroughly as photoanodes for PbS-sensitized liquid junction solar cells. The lower CBM of SnO_2 was found to greatly promote carrier injection from PbS, which is especially pronounced for the harnessing of low energy photons. In addition, compared with TiO_2 the surface of SnO_2 has much higher affinity to the growth of PbS, leading much enhanced light harvesting. Rigorous interfacial engineering indicates that a CdS buffer layer sandwiched

between SnO_2 and PbS, and a ZnS passivation layer on the outmost surface of the electrode are beneficial to prevent the charge recombination and improve the photovoltaic performance of the cells. In an optimized cascaded structure, short circuit photocurrent density up to 17.38 mA cm^2 and power conversion efficiency of 2.23 % were attained with a PbS-sensitized SnO_2 solar cells under simulated AM 1.5, 100 mW cm^{-2} illumination, which is much superior to that of TiO_2 tested under similar conditions and represents one of the highest efficiencies reported for PbS-sensitized liquid junction solar cells.

7 Synthesis of SnO_2 Nanostructures by Electrochemical Anodization and their Application in SSCs

7.1 Introduction

As reviewed in Chapters 5 and 6, nanostructured SnO_2 has generated great scientific and technological interests because of its diverse optical, electrical and electrochemical properties.[115-121] It has been revealed that these intriguing properties are strongly affected by its size, shape, and crystal structure, *etc.*[199,200] Therefore, controlling these properties by revamping its morphology and topology has become crucial for its technological applications.[162,163] For instance, nanostructured SnO_2 is known to have unique characteristics such as oxygen deficient cites, varied cation valence states as well as increased geometrical surface area, *etc.*, making it an important sensing material for the detection of combustible and toxic gases (CO, CH_4, H_2S, *etc.*).[120,121,164] It has also shown great promise as an anodic material for lithium ion batteries owing to its high specific capacity of 781 mAh/g.[116,117] In addition, the high transparency of SnO_2 to the visible light as a result of the wide band gap makes it a suitable transparent electrode material for flat panel display and conducting substrates for solar cells.[114,115,121] Moreover, its superior charge transport properties and suitable band energetics relative to sensitizers is known to generate unprecedented photocurrent density in SSCs, which has been discussed in Chapters 5 and 6.

Various chemical and physical approaches have been developed to synthesize nanostructured SnO_2, including chemical methods such as sol-gel,[165,166] chemical

vapour deposition (CVD),[167] hydro/solvothermal methods,[168-170] spray pyrolysis,[171] *etc.*, and physical methods such as magnetron sputtering,[172] pulsed laser deposition (PLD),[173] thermal evaporation,[174] *etc.* Using these methods, a wide variety of SnO_2 nanostructures with interesting properties have been prepared, such as nanoparticles,[175] nanowires,[162,176] nanotubes,[163,177] nanospheres, [116] *etc.* While SnO_2 nanocrystals of different morphologies have been prepared successfully, they are limited to either high temperature chemical and physical methods or template-assisted approaches. Therefore, it is essential to develop a synthetic method where SnO_2 nanoparticles can be prepared facilely in a cost effective way.

Electrochemical anodization is a template-free method which can be performed under ambient conditions and used to synthesize various nanostructures, such as honeycomb structured anodized aluminium oxide (AAO),[178] oriented TiO_2 nanotube arrays,[179-182] Nb_2O_5 nanotubes,[183] *etc.* SnO_2 films with disordered pore structures were also prepared via electrochemical anodization of tin foil in acidic media by Liu *et al.*[184] However, little work has been reported thus far on the preparation of monodispersed SnO_2 nanocrystals and understanding their assemblies of different morphologies. Here we show a facile two-step method: tin oxide colloidal particles were firstly synthesized by electrochemical anodization of tin foil by controlling the composition of the electrolyte; the obtained tin oxide colloidal particles were then assembled into various super-structures such as nano/microspheres, cubes, octahedra, *etc.*, with mesoscopic pore structures by controlling the dispersion media (solvent) of as-prepared tin oxide colloidal particles in the aging step. As the anodization reactions are carried out under ambient conditions, the two-step method could feasibly produce nanostructured tin oxide in a continuous fashion, which is particularly important for making nanostructured materials on a large scale, in contrast with the more commonly

used hydrothermal and expensive physical deposition methods. Using this two-step synthesis method, the cumbersome post-treatment required in soft and hard template-based methods could be avoided.[178-180]

In solution-based nanoparticles synthesis, aggregation[185] and coarsening[186] are generally involved during the nucleation and growth processes. In addition, the size, shape of the primary nanoparticles, and the surface charges, *etc.* are important factors in controlling the assemblies of nanostructures, of which the surface chemistry of the primary nanoparticles may further depends on the temperature, composition, polarity and other properties of the dispersing medium.[187,188] In this study, by controlling these parameters, the as-prepared primary tin oxide nanoparticles obtained from 1 M water-containing and water-free electrolyte were found to assemble into mesoporous hollow and solid SnO or SnO_2 nano/micro-structures of various shapes depending on the final aging step. Among them the mesoporous SnO_2 solid spheres were employed as photoanodes for CdSe-sensitized solar cells. As shown later, the macroscopic morphology of the SnO_2 nanostructures ensures efficient light scattering, which greatly enhances light harvesting.

7.2 Synthesis of tin oxide primary nanoparticles by electrochemical anodization of tin foil

Electrochemical anodization is a very facile method for tin oxide colloidal particle preparation. It is based on the anodic oxidation of tin metal (Sn) in alkaline medium where Sn is oxidized and reacts with OH^- in the electrolyte to form tin oxide. In this way, tin oxide nanocrystals can be synthesized in a continuous process and the

size of the obtained nanocrystallites can be controlled by adjusting the anodization parameters such as applied voltage, currents, electrolyte composition, *etc*.

7.2.1 Electrochemical anodization of tin foil

In a typical electrochemical anodization experiment, tin foil (trace metal basis, Alfa Aesar, 99.8%) of thickness 0.5 mm was used as the anode and a glassy carbon plate as the cathode in a two-electrode cell configuration as illustrated in Figure 7.1. Prior to anodization, tin foil with an area of 50 mm × 50 mm was cleaned ultrasonically in ethanol and deionized water each for 15 minutes followed by drying in an air stream. A glassy carbon plate (3 mm thick) cathode with the same area was placed 2 cm from the tin foil during anodization. Although the anodization products are dependent on the anodization parameters, as a few groups reported for the synthesis of TiO_2 nanotube arrays,[182,189] an anodizing electrolyte with a fixed composition of 0.1 M NaOH (reagent grade, Sigma-Aldrich, 98%), 0.05 M NH_4F (trace metal basis, Sigma-Aldrich, 99.99%), ethylene glycol solvent (anhydrous, Sigma-Aldrich, 99.8%,) and with or without 1 M, 1.5 M deionized water was used to anodize the tin foil at room temperature. Anodization of tin foil was performed without stirring the anodizing electrolyte.

The anodization experiment can be accomplished by either a potentiostatic method (controlling the potential applied to anode while current is measured) or galvanostatic method (controlling the current passed through the anode and corresponding potential is measured). In this study, the potentiostatic method with an optimum fixed voltage of 4 V was applied in the electrolytic cell for 10–20 hours by a digital source meter (Keithley 2612A). Under the applied voltage, the tin foil was

oxidized to Sn^{2+} and hydroxyl ions (OH^-) in the anodizing electrolyte reacted with Sn^{2+} where it could form unstable $Sn(OH)_3^-$ ions which in turn precipitates as a white powder $Sn_6O_4(OH)_4$, by the following reactions:

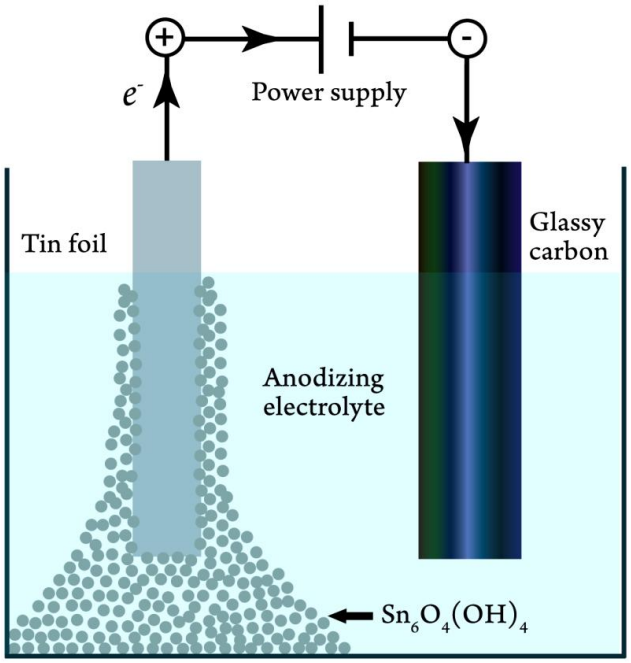

Figure 7. 1 A schematic diagram illustrating the working principle of electrochemical anodization of tin foil in an electrolytic cell with a two-electrode configuration.

$$Sn^{2+} + 3(OH)^- \rightarrow Sn\,(OH)_3^-$$

$$6Sn\,(OH)_3^- \rightarrow Sn_6O_4(OH)_4 + 4H_2O + 6(OH)^-$$

The white powder was then collected for further post-treatment to tailor its morphology. At higher applied voltages *i.e.* 10–30 V, a small amount of gray nanoparticles were found to precipitate out near the cathode as a result of the reduction of Sn^{2+} at the glassy carbon electrode forming Sn metal, and gas bubbles were also observed at the surface of tin foil.

7.2.2 Current transients during anodization

When the electrochemical anodization of tin foil begins, an oxide layer is formed at first. In the presence of fluoride ions (F^-), the growth of nanoparticles takes place at the tin/oxide and oxide/electrolyte interfaces by outward motion of Sn^{2+} and inward motion of OH^- in the presence of an electric field. Figure 7.2 shows a current transient during a potentiostatic anodization of tin foil. The current decreases drastically just after the start of anodization because of the formation of oxide which passivates the tin foil initially. However, in the presence of F^-, small pits may presumably form due to chemical dissolution of the initially formed tin oxide. Hence, the anodic current increases because of the exposed tin foil to electrolyte through these small pits. With time, the anodic current decreases slowly with the depletion of electrolyte species.

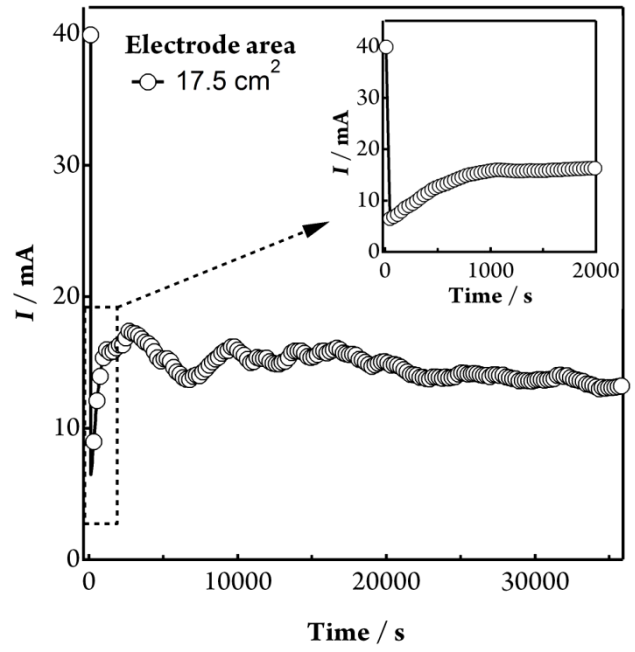

Figure 7. 2 A typical current transient for anodization of tin foil at 4 V for 10 hours in an electrolyte comprised of 0.1 M NaOH, 0.05 M NH_4F, and 1 M deionized water in ethylene glycol solvent. Inset figure shows the zoomed in plot from the start to 2000 seconds.

The F^- ions play an important role for continuous formation and precipitation of the tin oxide colloidal particles from tin foil. When an anodizing electrolyte without F^- ions (containing only 0.1 M NaOH and 1 M water in ethylene glycol) was used, a thin film of tin oxide (~5 μm) with disordered pore structure was found on the surface of the tin foil as shown in Figure 7.3 (a). However, when 0.1 M NH_4F was added as F^- source in the electrolyte, the formed nanoparticles were delaminated and precipitated out in the electrolyte at the bottom of the container. Figure 7.3 (b) shows the surface of a tin foil after anodization in F^--containing electrolyte at 5 V for 1 hour. A dendrite-like surface morphology was observed after anodization, which has an open surface structure, facilitating the continuous generation of tin oxide colloidal particles which was also observed by Chen *et al.*[175]

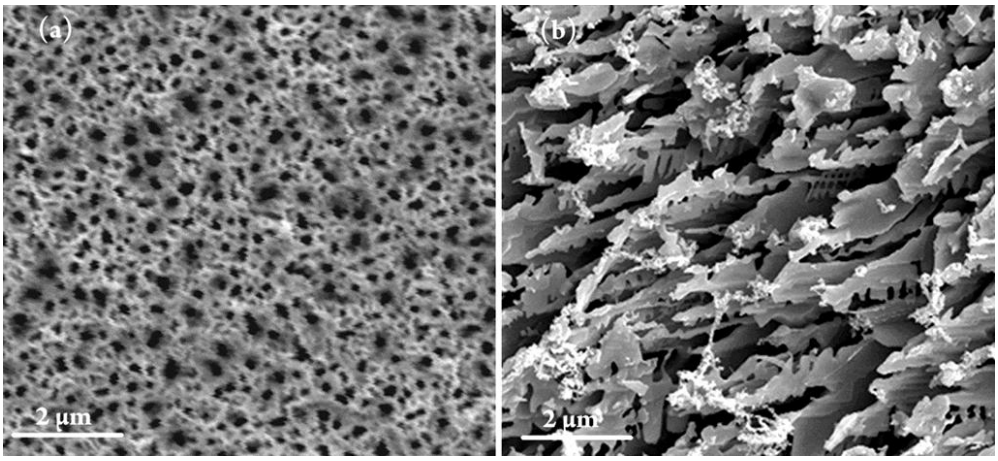

Figure 7. 3 Surface of anodized tin foil (at 5 V for 1 hour) after cleaning with ethanol. Anodization was carried out in (a) F^--free electrolyte containing 0.1 M NaOH and 1 M deionized water in ethylene glycol, and (b) F^--containing electrolyte comprised of 0.1 M NH_4F, 0.1 M NaOH and 1 M deionized water in ethylene glycol.

7.2.3 As-prepared tin oxide primary nanoparticles

The white precipitate was collected from the anodization bath and thoroughly dispersed in absolute ethanol in order to remove residual electrolyte by centrifuge for several times. Then the clean nanoparticles was dispersed in an ultrasonic bath for 3 minutes to make a homogeneous colloidal solution, which was collected to investigate the morphology with FESEM and TEM. The TEM sample was prepared by taking a drop of the colloidal suspension on carbon-coated copper mesh followed by drying in an electric oven at 55 °C.

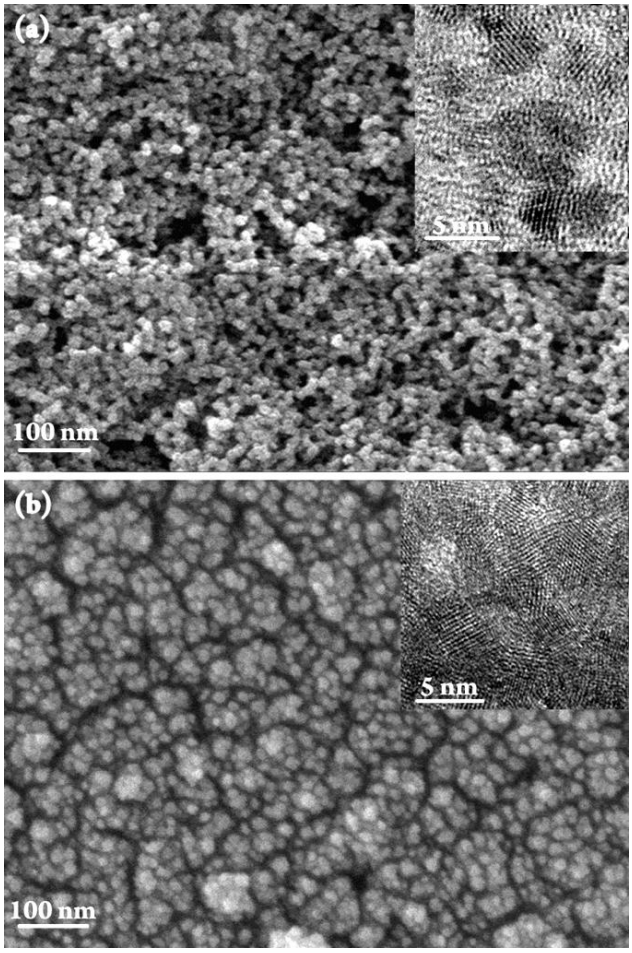

Figure 7. 4 As-prepared tin oxide primary nanoparticles obtained from anodization of tin foil, (a) in 1 M water-containing anodization electrolyte, and (b) in water-free anodization electrolyte. The inset of figures shows respective HRTEM images.

As the SEM images shown in Figure 7.4, the as-prepared tin oxide colloidal particles have a size of *ca.* 20–40 nm. HRTEM measurements suggest that the nanoparticles obtained from 1 M water and water-free anodization electrolyte consist of crystal grains of ~4 nm (inset Fig. 7.4(a)) and 5–6 nm (inset Fig. 7.4(b)), respectively. The crystal structure of these as-prepared nanoparticles was further confirmed by XRD measurement (Fig. 7.5). These coalesced and aggregated tin oxide nanocrystal grains were used as the building block for the assembly of various nano/micro-structures.

7.2.4 Structural examination of tin oxide nanoparticles

After cleaning and drying (at 55 °C to get rid of ethanol), the as-prepared tin oxide primary nanoparticles were characterized by XRD with a Bruker D8 using Cu Kα1 radiation (λ = 0.154059 nm). As shown in Figure 7.5, the XRD pattern reveals that the as-prepared sample is polycrystalline and consists of tetragonal tin (II) oxy-hydroxide ($Sn_6O_4(OH)_4$) (JCPDS No. 84-2157), which represents the major crystalline phase in the as-prepared sample. This reveals that the tin metal was oxidized to Sn^{2+} during the anodization process. The XRD peaks of $Sn_6O_4(OH)_4$ nanoparticles obtained from anodization in 1 M water-containing anodizing electrolyte shows lower peak intensity and noisier spectra than that of a water-free sample, suggesting that the former $Sn_6O_4(OH)_4$ nanoparticles is less crystallized (crystal grain size is smaller) which is also confirmed by the HRTEM images (inset of Fig. 7.4).

The colour of the $Sn_6O_4(OH)_4$ nanoparticles obtained from 1 M and 1.5 M water containing anodizing electrolyte was slightly brighter than that obtained from water-free electrolyte, suggesting that they might be different in shape, size, stoichiometry

etc. The presence of water may change the polarity of the electrolyte and its [OH^-] might be different from the water-free electrolyte if water is reduced at the counter electrode. As a consequence, the nucleation and growth of the colloidal particles would be influenced. However, a systematic study is required to elaborate the role of water in the anodization process.

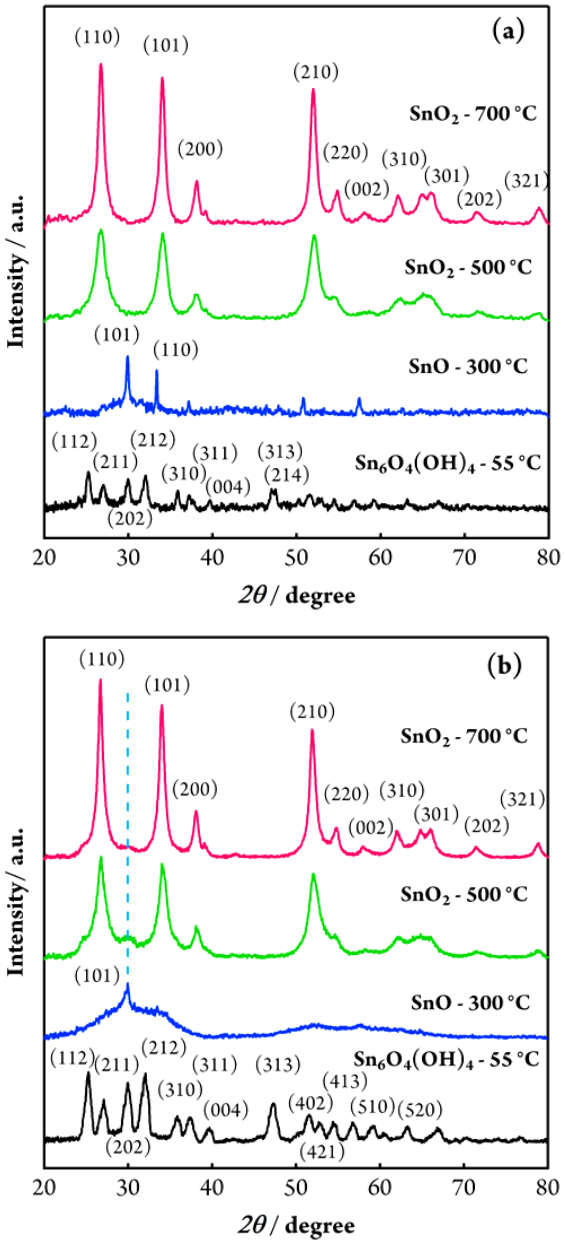

Figure 7. 5 XRD patterns of as-prepared clean and dried (at 55 °C) primary nanoparticles before and after heat-treatment at 300 °C, 500 °C, and 700 °C for 3 hours in air. (a) Nanoparticles are obtained from the anodization of tin foil in 1 M water-containing electrolyte, and (b) from water-free electrolyte; dashed vertical line in figure (b) represents the XRD peak corresponding to tin monoxide (SnO).

As shown in Figure 7.5, the as-prepared $Sn_6O_4(OH)_4$ was thermally dehydrated to tin (II) monoxide (SnO, JCPDS No. 06-0395) when heat-treated at 300 °C for 3 hours at ramping rate of 5 °C per minute. The diffraction peaks of SnO vanish upon further heat-treatment (nanoparticles obtained from 1 M water containing anodizing electrolyte) in air at 500 °C and 700 °C for 3 hours and exhibits XRD pattern being indicative of the (110), (101), (200), (210), (310), (301) and (201) planes of the tetragonal rutile structure of SnO_2 (JCPDS No. 72-1147). However, the nanoparticles obtained from water-free electrolyte show an XRD peak at 29.87^o even after heat-treatment at 500 and 700 °C, implying that it contains small amount of SnO. The diffraction peaks of SnO_2 become much sharper after annealing at 700 °C for 3 hours, indicating a larger grain size (~9 nm) and improved crystallinity.

7.3 Post-treatment of $Sn_6O_4(OH)_4$ primary nanoparticles

The as-prepared $Sn_6O_4(OH)_4$ colloidal particles were assembled into larger super-structures of various morphologies, depending on the post-treatment conditions, which are discussed in the following subsections.

7.3.1 Synthesis of mesoscopic solid spheres

In a typical synthesis of tin oxide solid spheres, the as-prepared $Sn_6O_4(OH)_4$ primary nanoparticles obtained from water-free anodizing electrolyte were collected and dispersed in ethanol with a concentration of ~25 g/L so that the nanocrystals can move freely inside a sealed vial while they were aged in an electric oven at 55 °C for different durations. Following the aging process, white sediment was observed at the bottom of the container. As shown in Figure 7.6, the sediment was found to be almost

monodisperse spherical particles, which is distinct from the as-prepared primary nanoparticles (Fig. 7.4(b)). The magnified images (inset of Fig. 7.6) reveal that the spheres have a rough and granular surface, implying they are built up by agglomeration of small colloidal particles.

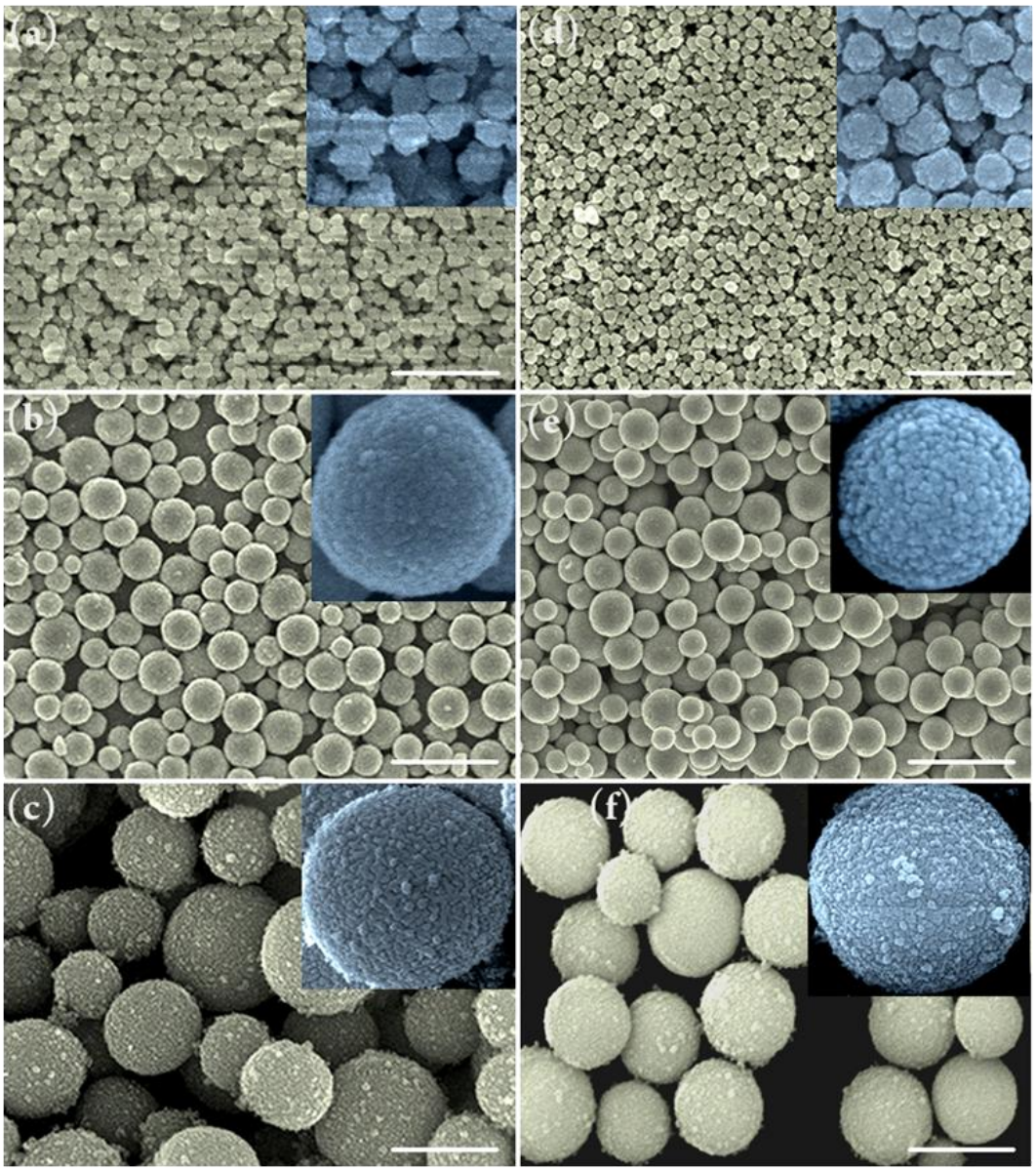

Figure 7. 6 SEM images of tin oxide spheres obtained by aging (at 55 °C) the as-prepared tin oxide primary nanoaperticles obtained from water-free electrolyte for different durations: (a, d) 1 hour, (b, e) 3 hours, and (c, f) 10 hours. The samples shown in figures (a-c) were as-prepared while those in figures (d-f) were sintered in air at 500 °C for 3 hours prior to SEM measurement. The scale bar is 1 micron. The insets show enlarged images of corresponding spherical particles.

The as-prepared samples (Fig. 7.6(a-c)) retain nearly identical spherical morphology after sintering at 500 °C as shown in Figure 7.6(d-e). The size of the spheres is found to be in the range of ~100 nm to ~1 μm, dependent on the aging time from 1 to 10 hours, respectively. This time-dependent particle size strongly suggests that the spherical particles are grown up by a continuous collection of $Sn_6O_4(OH)_4$ nanocrystals during the solution-based aging step.

As the TEM images show in Figure 7.7, the annealed SnO_2 spherical particles are solid and the SAED patterns (insets of Fig. 7.7) indicate that they are polycrystalline in nature, consistent with the XRD measurements. Closer investigation by HRTEM (insets of Fig. 7.7) reveals that regardless of aging time, the size of small particulates on the surface of heat-treated (at 500 °C) solid spheres is ~5-6 nm, which is almost the same as the as-anodized nanocrystals (at 55 °C) shown in Figure 7.4(b), suggesting that the SnO_2 spherical particles of time-dependent particle size are formed by agglomeration of these nanocrystals.

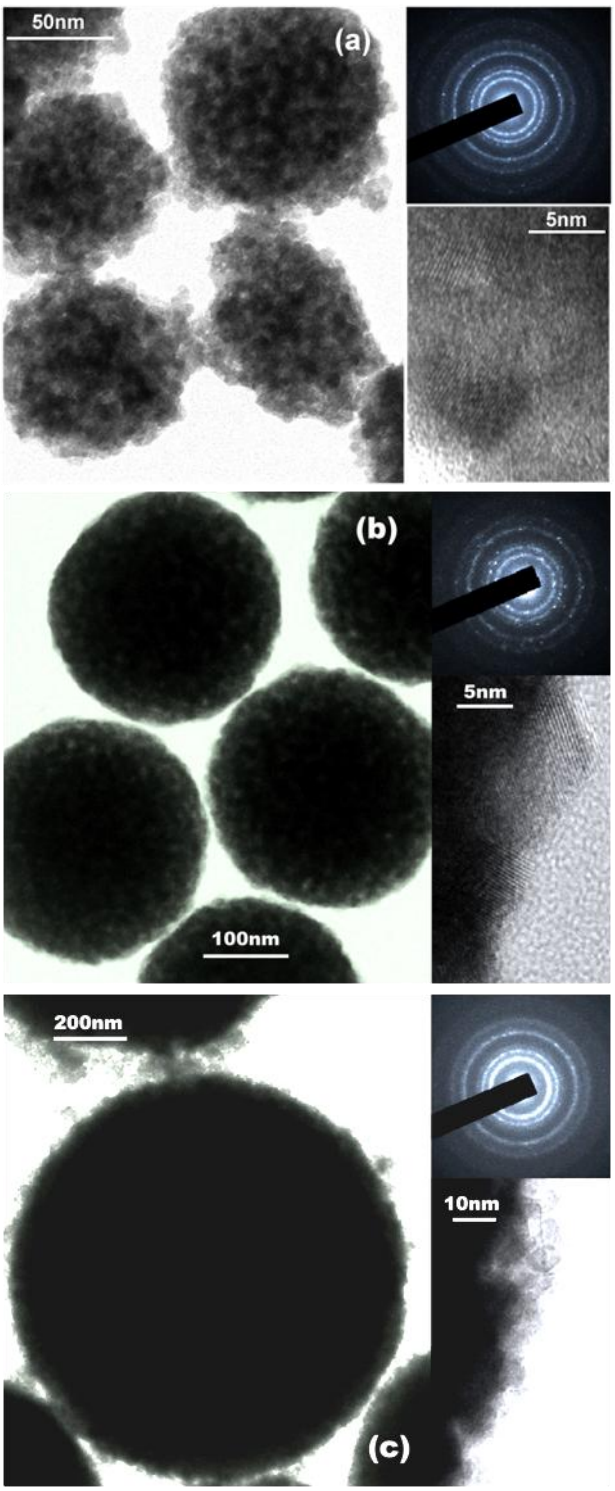

Figure 7. 7 TEM images of sintered (at 500 °C for 3 hours) SnO_2 spheres shown in Figure 7.6 (d-f); (a) 1 hour, (b) 3 hours, and (c) 10 hours. The insets show the SAED patterns of respective solid spheres and their HRTEM images.

7.3.2 Synthesis of mesoscopic hollow spheres

In contrast to the solid spheres synthesized by aging colloidal particles obtained from water-free anodizing electrolyte, it was observed that hollow spheres were formed when aging $Sn_6O_4(OH)_4$ colloidal nanoparticles obtained from 1 M water-containing electrolyte. Similar to the solid sphere, in a typical aging process the as-prepared $Sn_6O_4(OH)_4$ nanoparticles were dispersed in ethanol with a concentration of ~25 g/L sealed in a vial and aged in an electric oven at 55 °C. As shown in Figure 7.8(a, b), the as-prepared spheres of sizes 200–500 nm were found with hollow interior and grainy surfaces. The HRTEM images in Fig. 7.8(c) show that these hollow spheres have almost the same grain size as that of the primary nanaocrystals being ~4 nm, implying they were also built up by agglomeration of small colloidal particles.

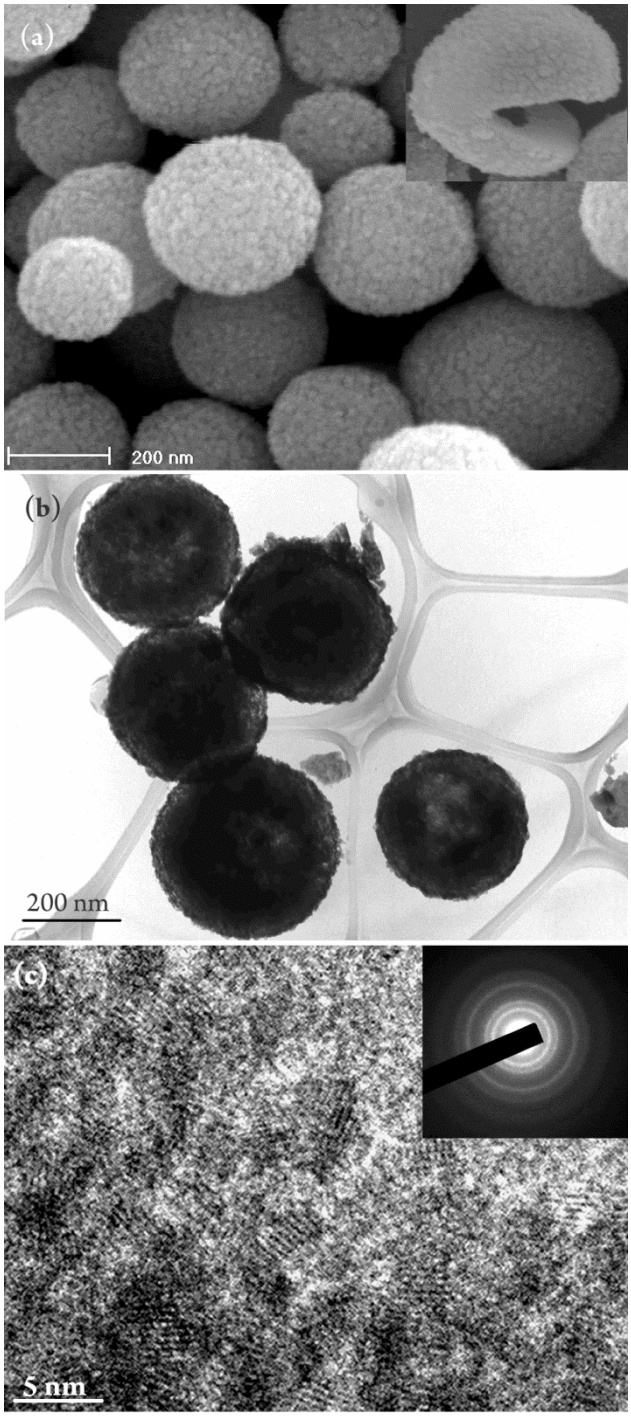

Figure 7. 8 (a) SEM image of as-prepared hollow spheres synthesized by aging (at 55 °C) the clean colloidal $Sn_6O_4(OH)_4$ nanoparticles in ethanol obtained from 1 M water-containing anodizing electrolyte, (b) corresponding TEM, and (c) HRTEM image of $Sn_6O_4(OH)_4$ hollow spheres.

7.3.3 Growth mechanism of the nano/micro-spheres

Morphological evolution has been extensively investigated for various nanomaterials, where several approaches such as Ostwald ripening,[190,191] oriented attachment,[192] differential diffusion by Kirkendall effect,[193] and template-assisted method,[194] *etc*., have been reported. Considering the actual material synthesis conditions and their final morphology, it is however, challenging to demonstrate an exact mechanism, as the aforementioned processes may occur simultaneously. Generally in the solution-based materials synthesis, crystal growth processes are mainly controlled by two competitive mechanisms — Ostwald ripening[191] and oriented attachment.[192]

Thermodynamically, the shape of particles is dominated by the crystal planes with lowest surface energy as suggested by the Wulff construction which provides a geometrical route and effectively maps the expected shape of a crystal (Fig. 7.9).[195,196] If there is no preferred orientation for the growth, the shape of the particle is usually spherical. However, if the orientation of one crystal plane is preferred than other orientations according to the Wulff construction, the equilibrium crystal shape would be non-spherical.[196,197]

The Ostwald ripening process provides a general guide for the preparation of nanocrystals where a simple mass transport process of the constituents is required from small particles to the large ones driven by a chemical potential gradient between solid-liquid interfaces as well as non-uniformity of crystallites under experimental conditions.[198] In practice, the crystal growth largely depends on the structural properties of materials and ability to activate or deactivate a crystal plane in a synthetic architecture, and interactions among crystallites such as surface hydrophilic

and hydrophobic forces, van der Waals attraction potential, hydrogen bonding, electrostatic attraction and repulsion based on the dielectric constant of solvent and dipolar attraction potentials, *etc*.[199]

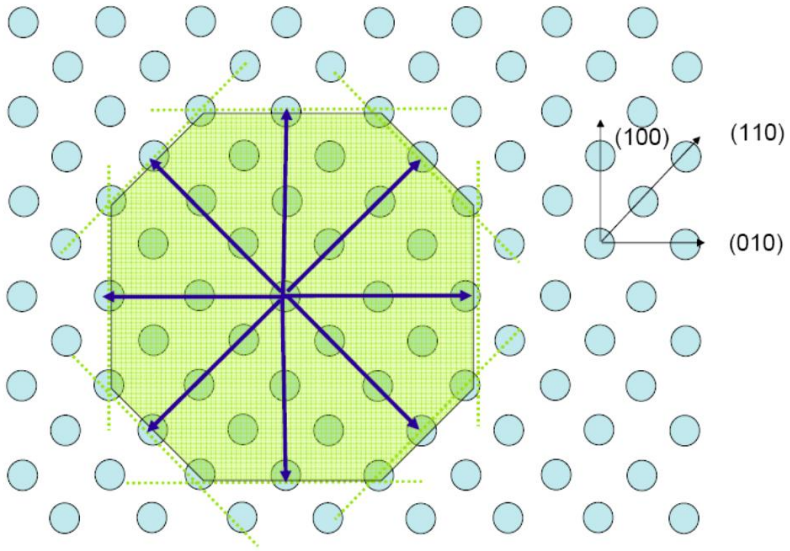

Figure 7. 9 Wulff construction enclosed by crystal plane of the lowest surface energy gives an equilibrium shape of nanocrystal.[200,201]

Oriented attachment (OA) represents a special kind of aggregation of nanocrystals that provides an important route to form new single crystals, twins and intergrowth by crystallographic alignment and coalescence between tiny particles. Generally, OA involves spontaneous self-organization of adjacent particles so that they share a common crystallographic orientation, followed by joining these particles at a planar interface. In liquid environment, the degree of freedom of particles is high and the coalescence occurs between the particles having the same crystallographic orientations; coalescence does not occur in different crystallographic orientations.[202] Penn and Banfield have shown that inorganic nanocrystals are made up of hundreds or even thousands of atoms which can be the basic building blocks for the fabrication

of highly ordered extended solids but the dimension of the attaching particles must be similar.[203] OA may also occur via side-by-side nucleation of particles on a substrate that coalesce during growth. Higher initial ion concentration and super-saturation of liquid medium enhance growth and consequently larger nanoparticles are obtained.

From the nearly unchanged crystal grains of $Sn_6O_4(OH)_4$ in solid (Fig. 7.7) and hollow spheres (Fig. 7.8) compared to the corresponding as-prepared primary $Sn_6O_4(OH)_4$ nanoparticles (Fig. 7.4), it seems unlikely that the growth of spherical particles is via coalescence of two or more identical particles. In addition, while preferential interactions between crystallographically oriented crystal grains in the diluted homogeneous colloidal solution may take place at the initial aging stage and form larger colloidal particles, it is very unlikely that the subsequent growth occurs by the same mechanism because of restricted rotational and translational motion in the sediment.

From the above observation, it is proposed that the growth of spheres undergoes an Ostwald ripening process because of the chemical potential gradient between the small and large nanoparticles. As the $Sn_6O_4(OH)_4$ nanocrystals are not soluble in ethanol under ambient conditions, these small crystal grains presumably detach from smaller particles to homogenize the concentration gradients which leads to complete dissolution of smaller particles, and become mobilized.[190,204] These small crystal grains migrate and re-deposit on the surface of larger particles (Fig. 7.10(a)) to minimize their surface energies to build a thermodynamically stable structure via an inter-particle assembly route, which was confirmed from the rough surface of spheres composed of a large number of loosely packed smaller primary nanocrystallites (Fig. 7.6 and Fig. 7.8). As the deposition of small crystal grains may proceed in all

directions, spherical particles with rough surfaces are eventually formed (Fig. 7.6). In overall, the above growth mode leads to a mesoporous structure of the final solid spherical particles, as a result of randomly packed nanocrystal grains.

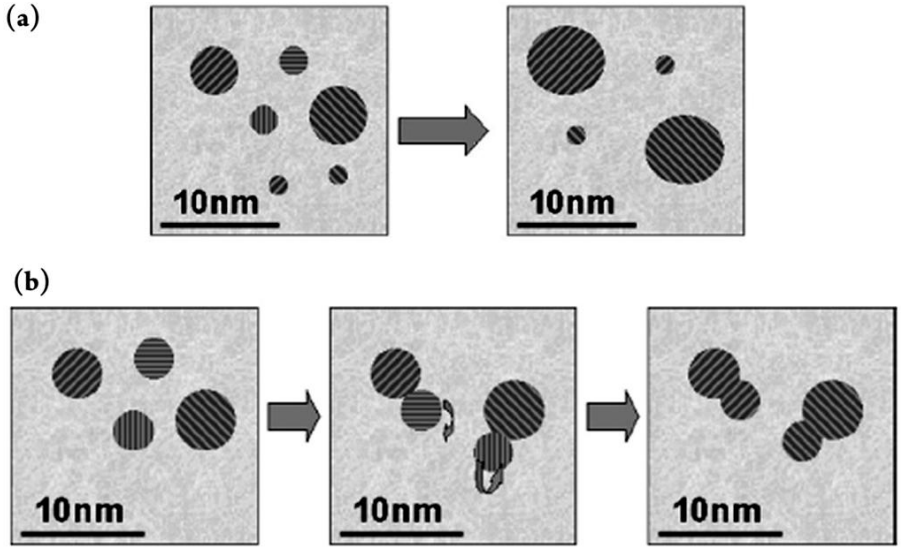

Figure 7. 10 Schematic representation of (a) Ostwald ripening, and (b) oriented attachment mechanisms of crystal growth.[191]

As frequently observed by others,[116,205,206] the hollowing process for the formation of hollow spheres (Fig. 7.8) can also be explained by Ostwald ripening. Apparently, the smaller and less crystallized $Sn_6O_4(OH)_4$ primary nanoparticles derived from 1 M water-containing electrolyte play critical roles in the hollowing process. Because of high curvature in the centre of the sphere, the nanocrystallites inside the sphere normally bear higher surface energy. Provided they are mobile enough, these high-energy nanocrystallites at the core of the sphere may detach and migrate towards outer sphere to reduce the total energy of the system. The diffusion of these high-energy crystallites may go through the cavities between nanoparticles to the surface to form mesoporous hollow structures.

7.4 Synthesis of hollow cubes

To synthesize cubic nano/micro-structures, ~250 g/L of the as-prepared clean $Sn_6O_4(OH)_4$ colloidal particles obtained from anodization of tin foil in 1 M water-containing anodizing electrolyte were dispersed ultrasonically in absolute ethanol for 3 minutes and kept in a sealed vial followed by aging at 55 °C in an electric oven for 3 hours. Because of the high concentration of $Sn_6O_4(OH)_4$ nanoparticles, they were easily sedimented, which were then collected for morphological investigation. As shown in Figure 7.11, the obtained particles are cubes, distinct from the spherical $Sn_6O_4(OH)_4$ nano/micro-structure shown in the previous section. These cubes are hollow with edge length ~500 nm and wall thickness 50–150 nm consisting of 10–15 nm crystal grains, which suggests that the pristine ~4 nm sized $Sn_6O_4(OH)_4$ crystal grains were coalesced by oriented attachment (schematically shown in Fig 7.10(b)) to form bigger crystal grains. These bigger crystal grains with enhanced crystallinity were further confirmed by the intense diffraction dots on the SAED pattern (inset of Fig. 7.11(d)).

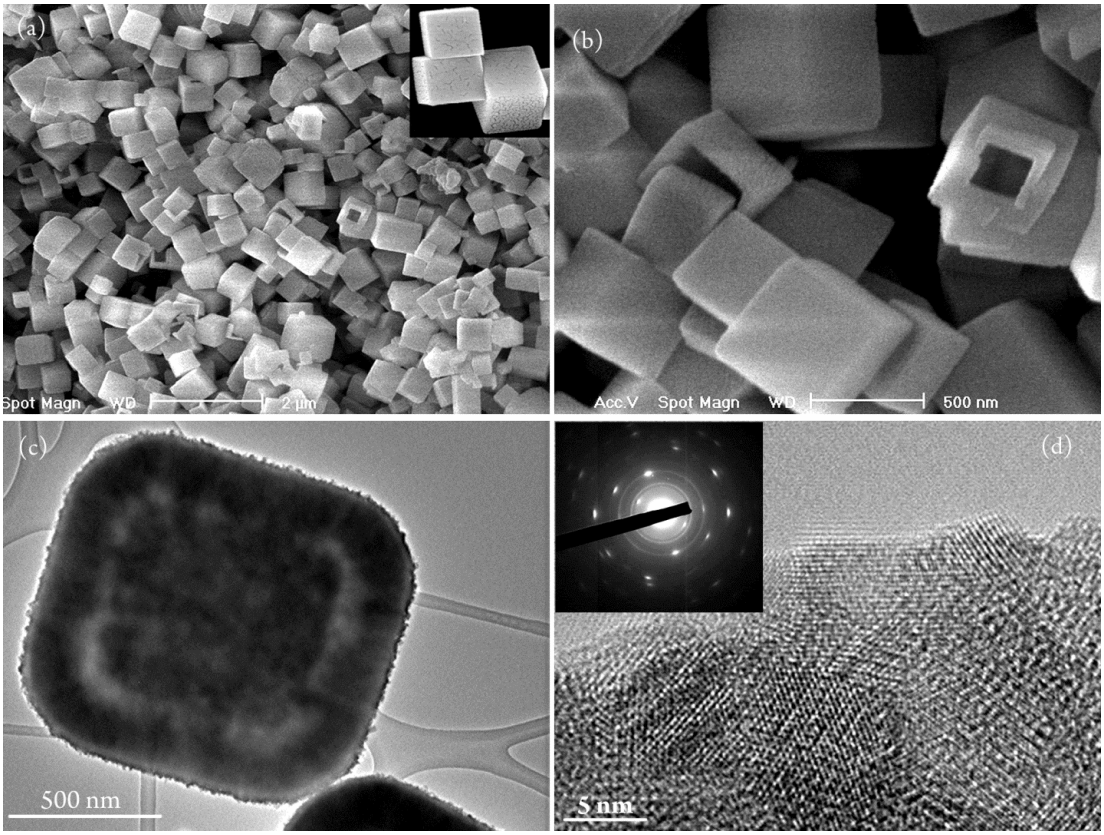

Figure 7. 11 (a-b) SEM image of as-prepared $Sn_6O_4(OH)_4$ hollow cubes synthesized from the primary nanoparticles obtained from anodization of tin foil in 1 M water-containing electrolyte, (c) corresponding TEM image shows the hollow feature, and (d) HRTEM image at the edge of cube shows bigger crystal grains (coalesced) and corresponding lattice fringes and SAED patterns.

In addition, the as-prepared $Sn_6O_4(OH)_4$ primary nanoparticles obtained in 1.5 M water-containing anodizing electrolyte were treated in the same way. Comparatively, larger hollow cubes of size 1–2 µm were observed. The SEM and TEM images in Fig. 7.12(a) confirm that the wall thickness of these polydispersed hollow cubes is ~200 nm. Although the walls are too thick for transmission of electrons in TEM measurement, the hollow features can be seen from some broken cubes (Fig. 7.12(b)). The HRTEM image clearly reveals that a few crystal grains coalesced by crystallographic orientation resulting in large crystal grains, which is consistent with

the intense diffraction dots and weak diffraction ring in the SAED pattern (Fig. 7.12(c)).

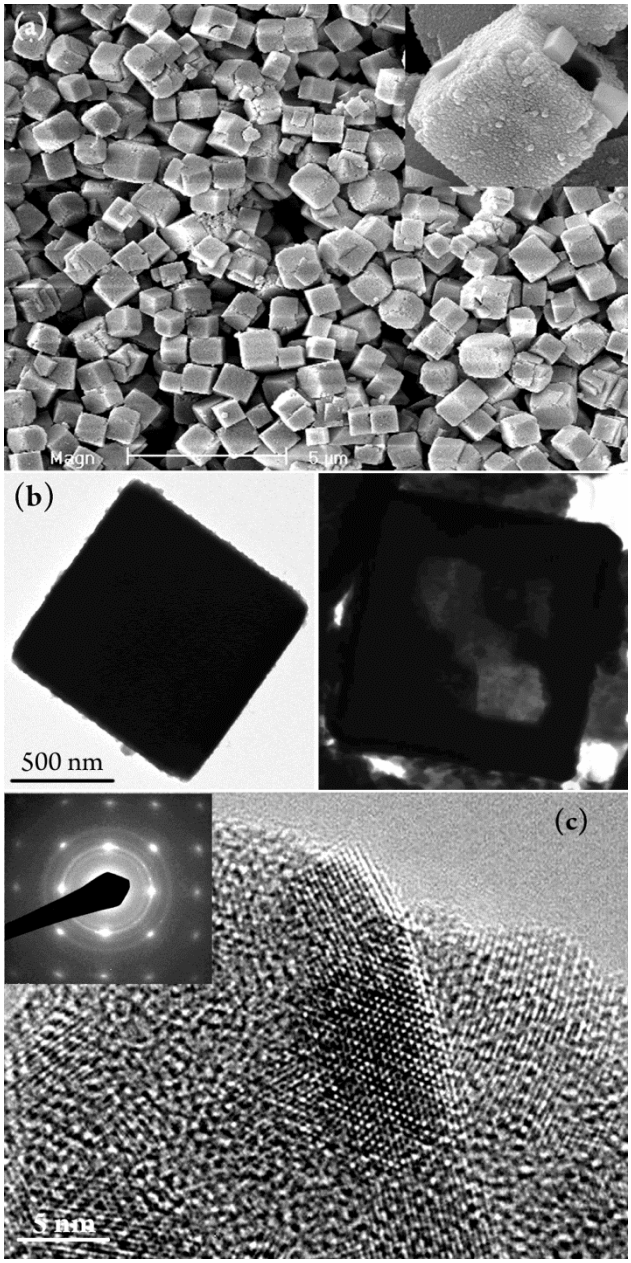

Figure 7. 12 Large cubes were prepared by post-treatment of as-prepared $Sn_6O_4(OH)_4$ primary nanoparticles obtained from 1.5 M water-containing anodizing electrolyte, (a) SEM, and (b) TEM image showing the hollow features, and (c) HRTEM at the edge of a cube wall showing local single crystal behaviour.

While Ostwald ripening was found to be responsible for the growth of hollow $Sn_6O_4(OH)_4$ spheres, it is believed that oriented attachment dominated the growth of cubic $Sn_6O_4(OH)_4$ nano/micro-structures when primary particles of ~9 times higher concentration were aged in the same ethanolic medium. It is anticipated that the frequency of collision of the same crystallographic orientation would increase significantly with the concentration of primary nanoparticles, which results in coalescence of the primary nanoparticles by sharing their common facets as illustrated in Figure 7.10(b).[202] While the exact reason for the formation of cube-like morphology is not clear, it is believed that the hollowing process of the cubes is similar to the spheres, a process dominated by Ostwald ripening.

7.5 Influence of ethylene glycol on shape evolution of $Sn_6O_4(OH)_4$ structures

As solvents of different dielectric constants affect the inter-particle interactions of nanoparticles, ethylene glycol (EG) of higher hydrophobicity was mixed with ethanol as directing agent during the aging step of $Sn_6O_4(OH)_4$ nanoparticles obtained from the anodization of tin foil in 1 M water-containing anodizing electrolyte. The synthesis procedure was the same as the aforementioned hollow cube synthesis but EG with a few volume percentage was added and kept in a sealed vial during aging at 55 °C for 3 hours. It was observed that with increasing volume percentage of EG, the cubes were turned into a family of polymorphic mesocrystals. While the hollow cubes with sharp edges and corners are formed in ethanol solvent (Fig. 6.13(a)), the addition of 2 volume percent (V%) EG in ethanol leads to cubes with rounded edges and corners (Fig. 6.13(b)). With more EG addition in ethanol, the cubic structures show even more facets than that of rounded cubes. Hollow cubes with chamfered edges with sixteen or more facets were observed at 20 V% EG in ethanol which are called

rhombicuboctahedron (Fig. 6.13(c)). A mixture of octahedron and larger polyhedrons with joint octahedrons (Fig. 6.13(d)), and durian-like superstructure of size ~5 μm (Fig. 6.13(e)) were observed in presence of 50 V% and 80 V% EG, respectively.

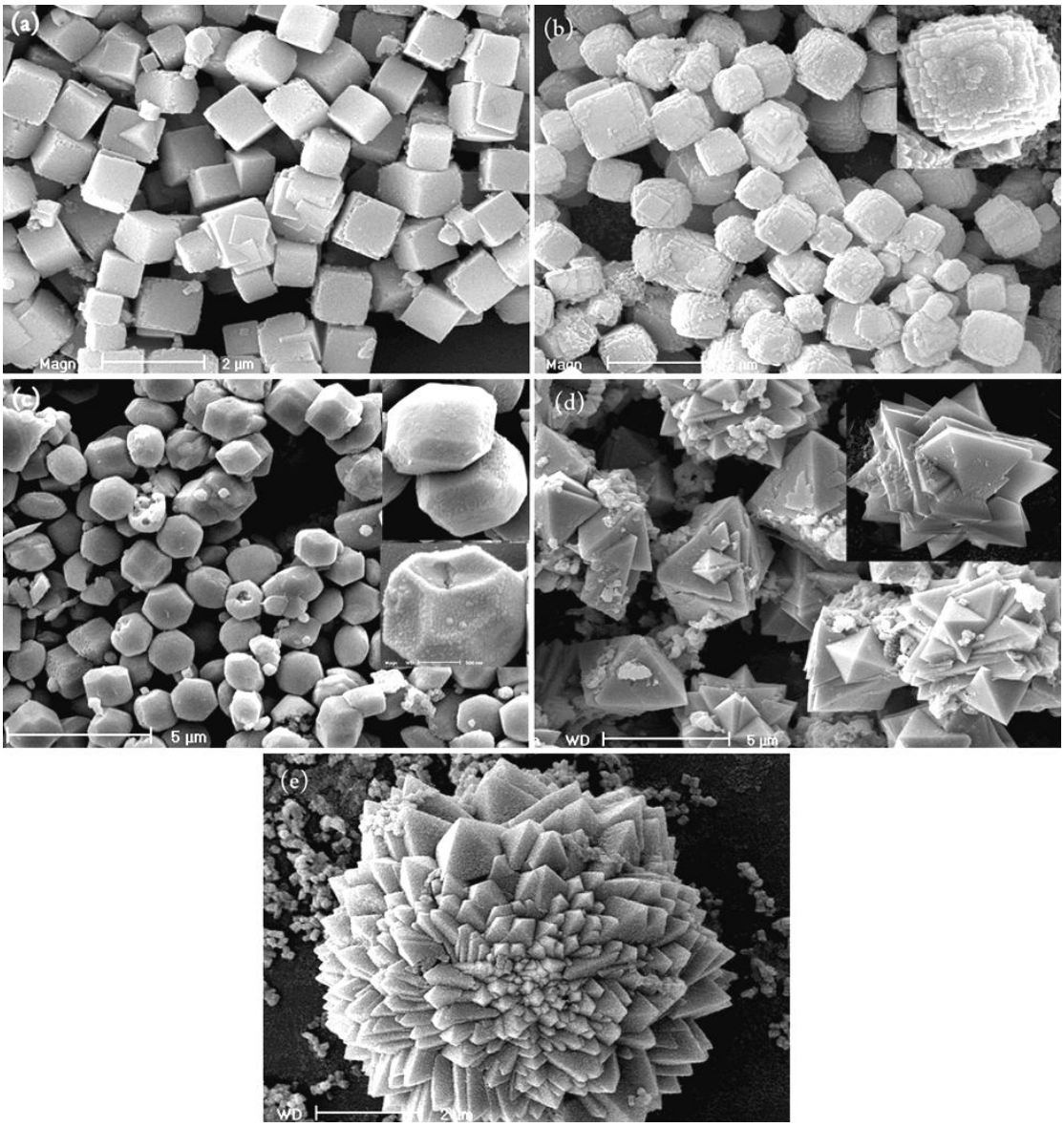

Figure 7. 13 SEM images of as-prepared $Sn_6O_4(OH)_4$ sample obtained in 1 M water-containing anodizing electrolyte aged at 55 °C with different volume ratio of ethylene glycol in ethanol, (a) 0%, (b) 2%, (c) 20%, (d) 50%, and (e) 80% EG.

From the above observation, EG acts as a crystal growth modifier which is believed to stabilize the high-energy facets of $Sn_6O_4(OH)_4$ primary nanoparticles

while they are coalesced into complex super-structures. In addition, since the viscosity of EG is much higher than ethanol, the kinetics of OA may be slowed down, which further enables the assembly of nanoparticles in the mesoscale through a preferential growth mode. Thus, the high-energy but least stable facets in the normal synthesis conditions may appear in the final nanostructures, when the surface energy of these high-energy facets becomes significantly lower in the presence of EG. It is believed that both the oriented attachment and Ostwald ripening are involved in determining the shape of these polymorphs. However, the directional growth in the presence of EG is yet to be clarified and a systematic study is required to understand the detailed mechanism.

The schematic illustration in Figure 7.14 summarizes the topological evolution of the superstructures formed from nucleation and subsequent growth of nanoparticles through Ostwald ripening or oriented attachment. With low concentration of $Sn_6O_4(OH)_4$ primary nanoparticles in ethanol, solid and hollow spheres were assembled through Ostwald ripening upon aging, in which the nanoparticles obtained from 1 M water-containing anodizing electrolyte undergo hollowing process. While at a high concentration of $Sn_6O_4(OH)_4$ primary nanoparticles in ethanol, hollow cubes with sharp edges and corners were preferably fabricated via oriented attachment. When adding EG into the colloidal solution, the edges and corners of the cubes become rounded at low percentage of EG and they turn into rhombcubioctahedron, and then a mixture of octahedron and joint octahedron, and finally durian-like microstructure with increasing amount of EG in the solution as shown in the schematic diagram in Figure 7.14.

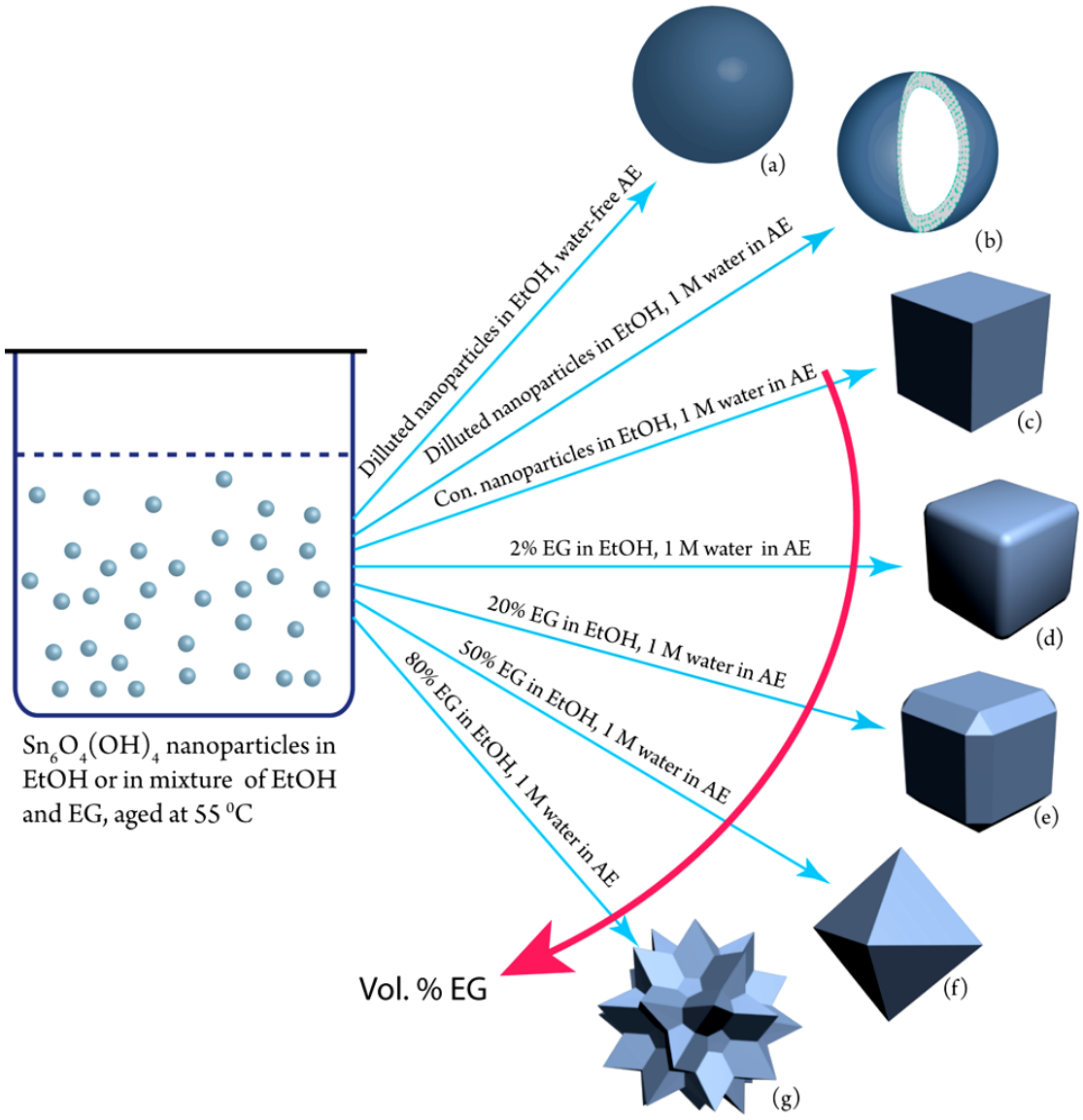

Figure 7. 14 Schematic presentation of solid/hollow spheres and transformation of multi-facet polymorphs from hollow cubes in the presence of increasing volume percentage of EG in ethanol (EtOH). (a) Solid sphere, (b) hollow sphere, (c) hollow cube with sharp edges and corners, (d) hollow cube with rounded edges and corners, (e) hollow cube with chamfered edges and corners, (f) hollow octahedrons, and (g) multifaceted polyhedrons. The abbreviated word, AE refers to anodizing electrolyte.

7.6 Reduction of Sn^{2+} at counter electrode:

A thin layer in gray colour was observed at a glassy carbon cathode after anodization for 10 hours. This is presumably the migrated Sn^{2+} at the carbon electrode under the applied electric field, which was reduced to tin metal (Sn) and

deposited on the carbon electrode. The morphology of the gray product was found to be dendrite–like, which is typical for many electrodeposited metals (Fig. 7.15).

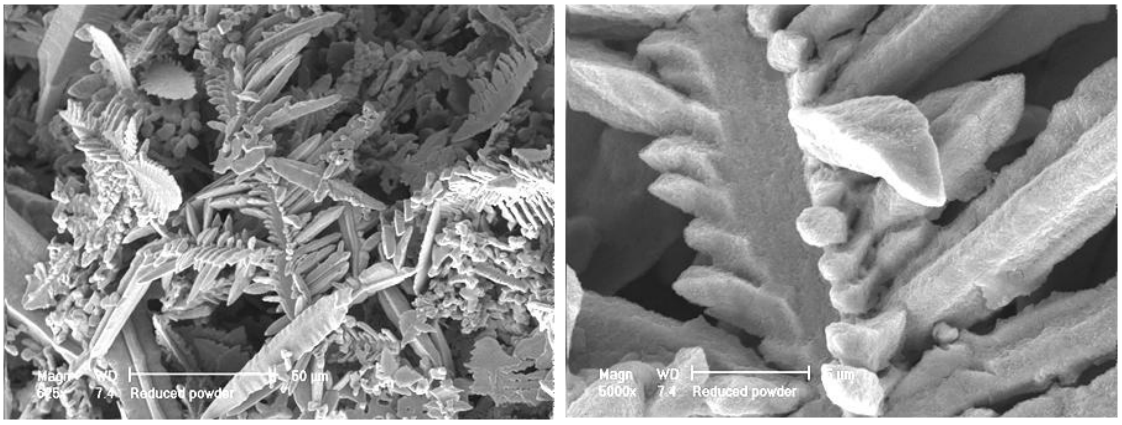

Figure 7. 15 Dendritic morphology of tin metal reduced from Sn^{2+} at the cathode under applied potential.

7.7 X-ray photoelectron spectroscopy (XPS) study of tin oxide samples

To elucidate the oxidation state of tin (Sn) in the as-prepared and annealed samples, surface compositional analysis was carried out by XPS measurement (AXIS Ultra). The wide scan survey XPS spectrum in Figure 7.16 reveals that there is an appreciable amount of fluoride ions (F^-) in the as-prepared sample obtained from 1 M water-containing anodizing electrolyte. A small F1s peak in the as-prepared sample was observed by high-resolution XPS spectroscopy (Fig. 7.17(d)). FTO glass was used as a reference to compare the as-prepared and annealed tin oxide samples, where differences in intensity and peak position were observed. From the quantification of elements of tin oxide (Table 7.1), it was observed that the annealed tin oxide sample has almost identical composition to the annealed FTO glass.

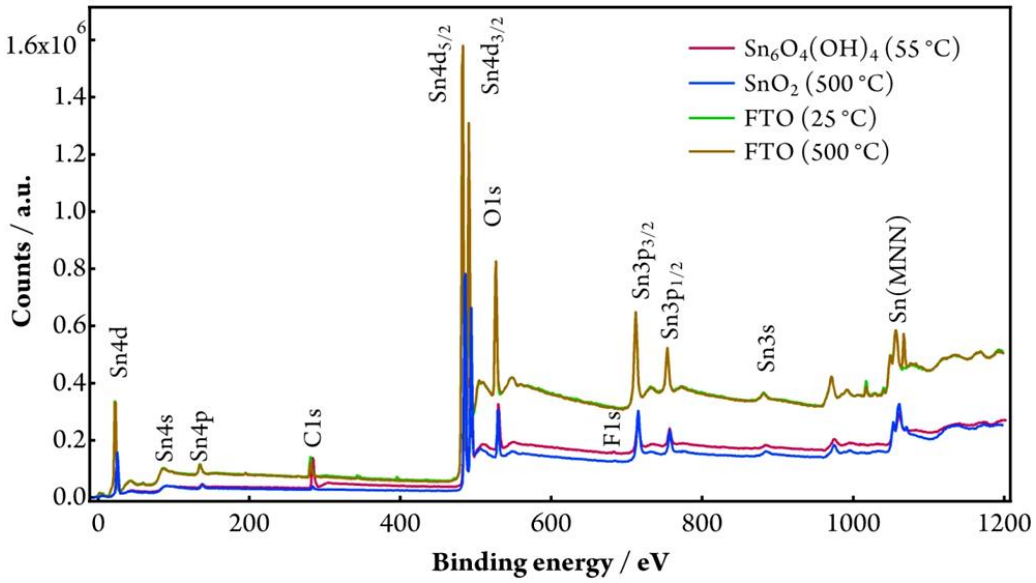

Figure 7. 16 XPS survey scans of tin oxide samples and FTO glass before and after heat treatment at 500 °C.

Table 7. 1 Elemental analysis of annealed tin oxide and FTO glass samples by quantifying the XPS spectra.

Annealed samples (at 500 °C)	Atomic %			O/Sn ratio
	Sn	O	F	
SnO_2	34.4	64.7	0.9	1.89
FTO glass	33.75	65	1.25	1.92

To elucidate the oxidation state of Sn in the as-prepared samples, the high-resolution XPS spectra were analyzed by fitting the XPS peaks (XPS Peak 4.1). As revealed in Figure 7.17(a), the high-resolution XPS spectra of the as-prepared sample show the spin orbit separation of $Sn3d_{5/2}$ and $Sn3d_{3/2}$ to be 8.4 eV which agrees well with the reported value.[207] Among these, the $Sn3d_{5/2}$ peak was deconvoluted by considering an inelastic Shirley-type background during spectral fitting. The relative

peak shifts were corrected by fixing the peak position of contaminant carbon at 284.5 eV and comparing with the database.

The deconvoluted $Sn3d_{5/2}$ peak was fitted with a peak binding energy of 486.65 eV corresponding to Sn^{2+} (Fig. 7.17(c)), and the major O1s peak was fitted with a binding energy of 530.1 eV (Fig. 7.17(b)) being related to the lattice oxygen, both of which are well consistent with the literature data,[208,209] indicating that the oxygen atoms are bonded with Sn^{2+}, as in $Sn_6O_4(OH)_4$. The smaller shoulder observed from the deconvolution of asymmetric O1s spectrum was believed to be the adsorbed O^- species or those making bonds with H *etc.* As shown in Figure 7.17 (d), the F1s peak was observed at a binding energy of ~684.5 eV, implying the presence of F^- species in the as-prepared $Sn_6O_4(OH)_4$ nanoparticles.

The same analysis was carried out to investigate the heat-treated (500 °C) samples. As shown in Figure 7.18, the deconvolution of $Sn3d_{5/2}$ spectra for the annealed SnO_2 (obtained from 1 M water-containing anodizing electrolyte) fitted well with a peak binding energy of 486.45 eV identical to Sn^{4+} (Fig. 7.18(b)), indicating the relevant bonding structure is SnO_2. It implies that after heat treatment at 500 °C, Sn^{2+} is oxidized to Sn^{4+} completely, being in good agreement with the literature data,[209] and with the XRD result (Fig. 7.5(a)) at 500 °C and 700 °C.

In comparison, the deconvoluted spectrum of the heat-treated sample obtained from water-free anodizing electrolyte (Fig. 7.18(d)) shows the presence of both Sn^{4+} (binding energy 486.55 eV) and small Sn^{2+} peaks (binding energy 486.05 eV), which is entirely consistent with the XRD measurement (Fig. 7.5(b).[210] As shown in Figure 7.18(c), the asymmetric O1s spectrum was deconvoluted into two peaks. Of these, the main peak at binding energy of 530.3 eV was related to the lattice oxygen and the

smaller peak at the shoulder (binding energy 531.45 eV) was assigned to the adsorbed O^- species.[211]

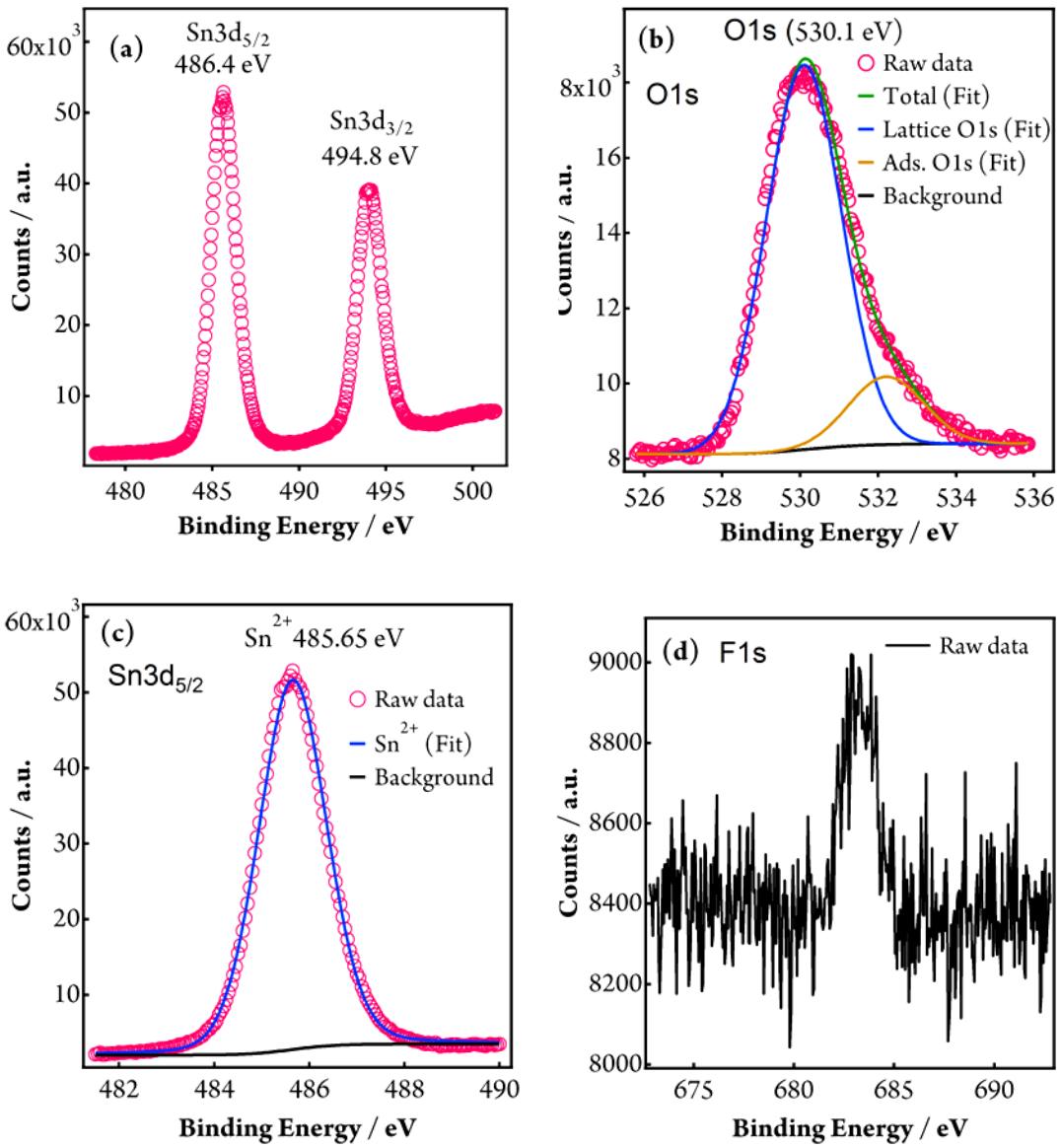

Figure 7. 17 High resolution XPS spectra of as-prepared $Sn_6O_4(OH)_4$ nanoparticles obtained from 1 M water-containing anodizing electrolyte, (a) raw Sn3d spectrum, (b) deconvoluted O1s, (c) deconvoluted $Sn3d_{5/2}$, and (d) raw F1s spectra.

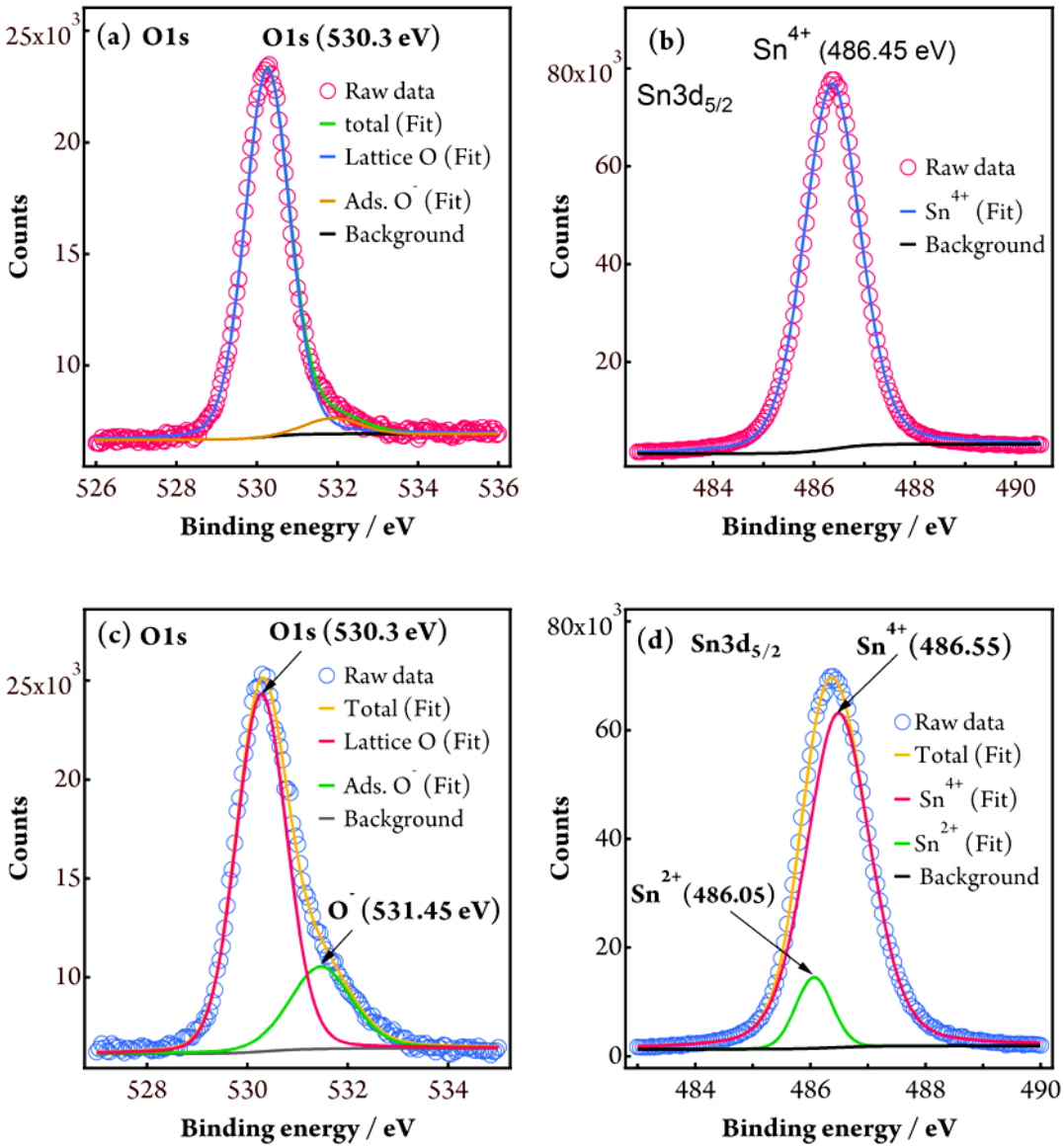

Figure 7. 18 Deconvoluted high-resolution XPS spectra of heat-treated (at 500 °C) tin oxide nanoparticles obtained from anodization of tin foil in (a, b) 1 M water-containing, and (c, d) water-free anodizing electrolyte.

7.8 Fourier transform infrared spectroscopy (FTIR)

The FTIR spectra of as-prepared and heat-treated nanoparticles were collected using a Varian 3100 FTIR setup. The spectra of $Sn_6O_4(OH)_4$ nanoparticles are shown in Figure 7.19. A strong signal is seen at around 3000-3700 cm^{-1}, which is typical for the stretching vibration mode of O-H groups in the Sn-OH bond.[212,213] In addition, the

O–H bending band appearing at 1622 cm^{-1}, is associated with the residual water and hydroxyl groups in the as prepared samples.[214]

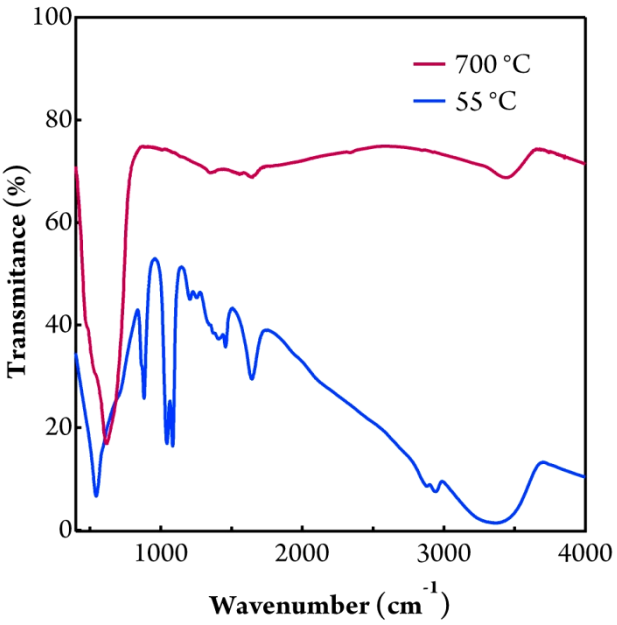

Figure 7. 19 FTIR spectra of the as-prepared $Sn_6O_4(OH)_4$ and heat-treated SnO_2 samples obtained from anodization of tin foil in 1 M water-containing anodizing electrolyte.

After annealing at 700 °C, the sample shows much a cleaner spectrum with significantly diminished peaks. The attenuation of the peak at around 1622 cm^{-1} indicates most -OH groups were removed after heat-treatment at high temperature,[215] which is consistent with the formation of SnO_2 from the $Sn_6O_4(OH)_4$ at 700 °C. The signals observed in the range 400–850 cm^{-1} could be assigned to vibrations of the O–Sn–O bridging, further confirming that the annealed sample is SnO_2.[214]

7.9 Optical properties of synthesized tin oxides

Tauc plots in Figure 7.20 show that the annealed (at 500 °C) sample has an absorption edge at 3.50 eV which is comparable to the bulk optical band gap of SnO_2,[216] consistent with the XRD and XPS results that SnO_2 was formed after annealing at 500 °C.

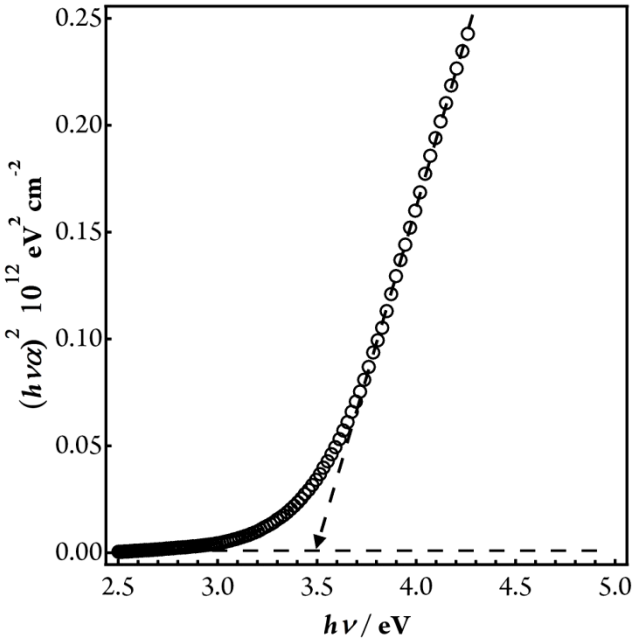

Figure 7. 20 Tauc plot of UV-vis spectra of the annealed (at 500 °C) tin oxide (SnO_2) sample.

7.10 Mesoporous solid SnO_2 as a photoanode in SSCs

Utilizing mesoporous SnO_2 solid spheres of size *ca.* 250 nm - 1 μm, a paste was prepared following the procedures described in Section 2.1 in Chapter 2. The screen-printed mesoporous SnO_2 electrodes were found to have an opaque white appearance, implying strong light scattering because of the macroscopic dimension of the SnO_2 spheres, which is anticipated to enhance light harvesting as photoanode in SSCs. The thickness of the SnO_2 electrodes was determined to be ~2 μm. They were sensitized

with CdSe by SILAR as discussed in Section 2.3.1 and a ZnS layer was also deposited onto the CdSe-sensitized SnO_2 electrodes following the SILAR method described in Section 2.4 in Chapter 2.

7.11 Optical properties of CdSe-sensitized SnO_2 mesoporous spheres electrodes

The monochromic photoresponse,[228] and ultrafast carrier dynamics[229] of CdSe-sensitized SnO_2 have been investigated by a few groups. Steady–state photoluminescence (PL) measurements were carried out to study the charge injection from CdSe to the two metal oxides upon illumination. If there is a favorable band alignment between light absorber (*i.e.*, CdSe) and underlying SnO_2 or TiO_2, the excited electrons mostly will be separated at their interface; thus the PL will be quenched which is evidence of charge separation. On the contrary, if the CBM of an oxide semiconductor (ZrO_2, Al_2O_3 *etc.*) is above the excited states of electrons, these excited electrons cannot be injected to the conduction band of Al_2O_3; thus the electrons will recombine with holes in the valence band and will give an emission. In this study, the PL spectroscopy was used to monitor a possible electron injection from CdSe into SnO_2, by comparing the obtained spectra with those of higher band gap Al_2O_3. PL spectra were collected with a spectrofluorophotometer (Shimadzu-RF5301).

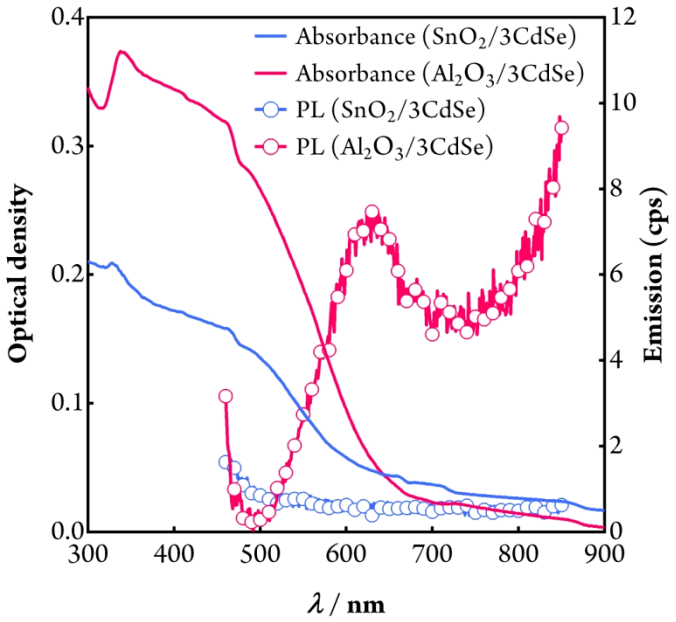

Figure 7. 21 Optical density, and PL spectra of 3CdSe-sensitized SnO_2 and Al_2O_3 electrodes. The excitation wavelength was 450 nm for PL measurement.

As shown in Figure 7.21, the absorption onset of 3CdSe-coated SnO_2 occurs at ~700 nm, implying quantum confinement of charges in CdSe. For comparison, a mesoporous Al_2O_3 electrode was also coated with 3CdSe, where an absorption onset of ~750 nm was observed, indicating slightly larger CdSe particles grown on Al_2O_3 electrode. As indicated in Figure 7.21, CdSe-coated Al_2O_3 gave emission at ~640 nm in the visible light region when it was excited at 450 nm. In comparison, no appreciable emission was observed from the CdSe-coated SnO_2 electrode. It is not surprising that the CdSe-sensitized Al_2O_3 electrode presents a clear radiative signal upon illumination, since Al_2O_3 has a very wide band gap and charge injection from the excited state of CdSe to the conduction band of Al_2O_3 is not favorable. As a consequence, excited electrons recombine radiatively with holes in the HOMO levels of the CdSe particle. It is known that SnO_2 has a much lower CBM than TiO_2 in the same media. Charge injection from excited CdSe to the conduction band of SnO_2 is

deemed to be much more efficient. The complete quenching of PL from the CdSe-sensitized SnO_2 electrode upon excitation suggests efficient charge injection, which is critical for charge separation and consequently the performance of the solar cell.

7.12 Photoelectrochemical properties of CdSe-sensitized mesoscopic SnO_2 spheres solar cells

To study the photovoltaic performance of CdSe-sensitized mesoscopic SnO_2 electrodes (~2 μm thick), cells were fabricated with platinized FTO cathode and a S^{2-}/S_x^{2-} electrolyte comprised of 0.125 M S, 0.5 M $Na_2S{\cdot}9H_2O$ and 0.2 M KCl in deionized water/methanol (7:3, v/v) as the hole transporter. To prevent recombination at the SnO_2/CdSe/electrolyte interface, SnO_2 electrodes were treated with $TiCl_4$ aqueous solution prior to CdSe deposition, and a thin passivation layer of ZnS was deposited onto the above-sensitized electrode as well by two SILAR deposition cycles.

As shown in Figure 7.22(a), electrodes without $TiCl_4$ pre-treatment or ZnS post-treatment exhibit very poor IPCE, with the peak quantum efficiency <10%. In contrast, concurrent surface treatment of $TiCl_4$ and ZnS greatly improves the IPCE of the CdSe-sensitized SnO_2 solar cells, which show strong photo-response in the visible light range with photon wavelengths even extending to ~800 nm. This higher IPCE at long wavelength implies that the CdSe layers used in complete solar cells probably ought to be considered as bulk CdSe. The highest IPCE was achieved with 10 SILAR cycles of CdSe deposition on SnO_2 electrodes comprised of mesoscopic spheres, being above 50% between 400 and 700 nm. The best device was obtained with 9CdSe-sensitized SnO_2 electrodes (Fig. 7.22(b)), with j_{sc} = 9.00 mA cm^{-2}, V_{oc} = 0.443

V, fill factor = 47.2%, and η = 1.91% under simulated AM 1.5, 100 mW/cm^{-2} illumination.

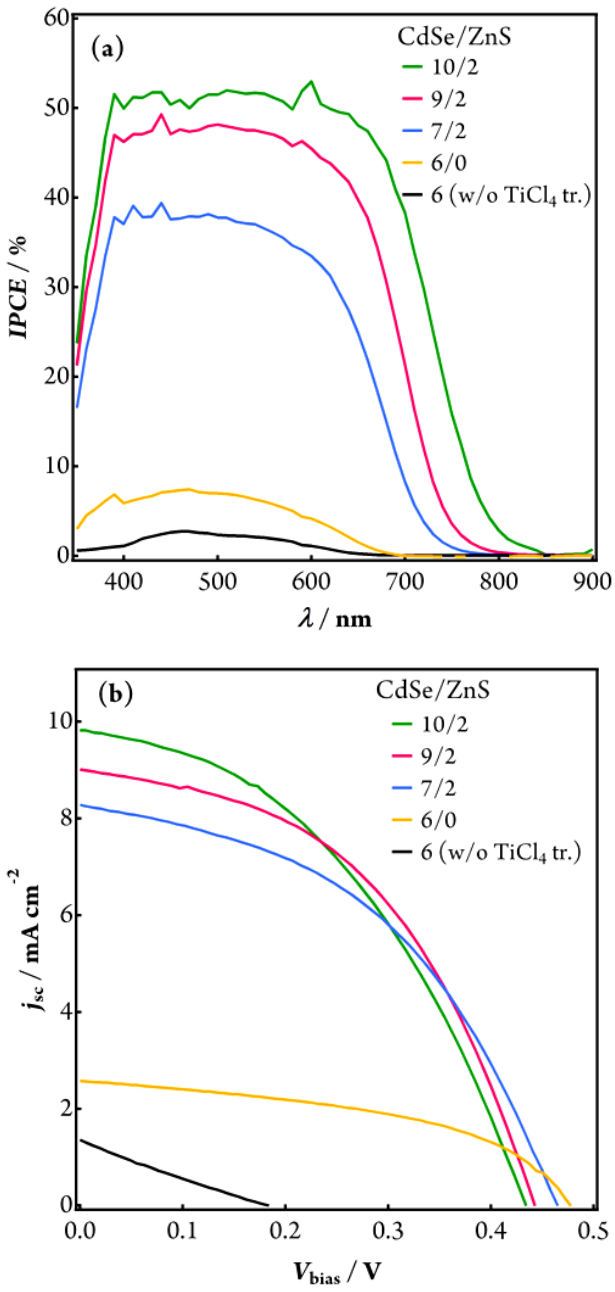

Figure 7. 22 (a) IPCE, and (b) *j-V* characteristics of *n*CdSe-sensitized SnO_2 cells under various treatment conditions.

Table 7. 2 *j-V* characteristics of *n*CdSe-sensitized SnO_2 (~2 μm thick) solar cells with various treatment conditions under simulated AM 1.5, 100 $mWcm^{-2}$ illumination.

Photoanode	V_{oc} *(V)*	j_{sc} *(mA* cm^{-2}*)*	*ff (%)*	*η (%)*
SnO_2/6CdSe/2 ZnS	0.183	1.36	23.0	0.06
SnO_2/$TiCl_4$+ 6CdSe	0.477	2.57	47.6	0.60
SnO_2/$TiCl_4$+ 7CdSe/2ZnS	0.465	8.27	45.3	1.80
SnO_2/$TiCl_4$+ 9CdSe/2ZnS	0.443	9.00	47.2	1.91
SnO_2/$TiCl_4$+ 10CdSe/2ZnS	0.434	9.80	42.4	1.81

It was reported that surface passivation of SnO_2 by a thin layer of Al_2O_3 could significantly improve the photovoltaic performance of dye-sensitized SnO_2 solar cells as a result of inhibited recombination.[118] It is believed that $TiCl_4$ treatment effectively passivates the surface of SnO_2. In addition, SILAR deposition forms a conformal coating of CdSe on SnO_2, which acts as a barrier layer (in a similar way to Al_2O_3), preventing injected electrons in SnO_2 from recombining with holes in the electrolyte. Moreover, the ZnS passivation layer on top of CdSe further hinders the backward reaction at the interface. A cell without a ZnS layer gives j_{sc} = 2.57 $mAcm^{-2}$, V_{oc} = 0.477 V, fill factor = 47.6%, and η = 0.60% under simulated solar irradiance, being much lower than that found for the above devices (Table 7.2).

However, the performance of these cells, especially the photocurrent was much lower than the CdSe-sensitized SnO_2 (commercial nanoparticles) cells as discussed in Chapter 5. Plausible reasons for the low photocurrent of CdSe-sensitized SnO_2 (macroscopic spheres) cell: much more thinner electrode (~2 μm) accommodates insufficient amount of CdSe sensitizers; because of much smaller crystal grains the

mesopores in SnO_2 spherical particles may not be fully accessible for CdSe and ZnS deposition, which may give rise to severe recombination if the bare SnO_2 surface is exposed to the electrolyte. As a result, lower photocurrent, hence the inefficient photoelectrochemical performance of cells is not surprising. In addition, the F^- in SnO_2 spheres may introduce more surface states, which may affect the separation of charge carriers for collection to the external circuit. It is expected that the photovoltaic performance of CdSe-sensitized SnO_2 could be greatly improved by rigorously optimizing the SnO_2 mesoporous film and the interfaces.

7.13 Summary

Mesoporous $Sn_6O_4(OH)_4$ spheres, cubes and polyhedrons of different sizes were successfully synthesized by a simple post-treatment of as-prepared primary nanoparticles obtained from the electrochemical anodization of tin foil. The mechanism of forming solid and hollow spherical particles is proposed to be Ostwald ripening where an extra hollowing process was undergone based on the surface energy difference of loosely-packed interior nanoparticles (obtained from anodization of tin foil in 1 M water-containing electrolyte) from those on the outer spheres. The oriented attachment and simultaneous Ostwald ripening-assisted hollowing process were proposed as the growth mechanism for the formation of hollow cube and multi-facets $Sn_6O_4(OH)_4$ polymorphs in a mixture of hydrophobic ethylene glycol and ethanol as directional agent. As the anodization reaction proceeds non-intermittently under ambient conditions, it provides a facile and economic way of making nanostructured SnO and SnO_2 on a large scale. The annealed, mesoporous SnO_2 spheres were tested as a photoanode material for SSCs and demonstrated promising photovoltaic performance when CdSe was used as light absorber. Recombination is

greatly suppressed by the conformal coating of light absorbing and passivation layers. This comprehensive study could open up the opportunities to build new types of superstructures from building block primary nanoparticles.

8 Conclusions and Recommendations

8.1 Conclusions

The objective of this work was to improve the performance of SSCs using various semiconductor sensitizers which have very high extinction coefficients, tunable optical and electronic properties, and generally cheaper than dye molecules owing to their inexpensive method of preparation. In addition to the sensitizers, much attention has also been paid to the wide band gap metal oxide semiconductors which possess excellent electronic and electrical properties.

In this work, at first, we studied the well-known cascaded CdS/CdSe-sensitized TiO_2 cells and achieved the best performance using CdSe-sensitized TiO_2 electrodes with practically identical optical density. Considering the energetics and kinetics of the CdSe and CdS/CdSe sensitized cells, it has been revealed that while CdS can greatly promote the subsequent growth of CdSe in the cascade electrodes and hence light harvesting, the presence of a CdS buffer layer impedes the injection of electrons from CdSe to TiO_2 and accelerates charge recombination at TiO_2/sensitizer interface. The noticeably slower charge recombination at the TiO_2/CdSe interface, and much enhanced light harvesting of long wavelength photons gave a better overall device performance compared with the cascaded CdS/CdSe cells. The obtained results from this comprehensive study provide several new findings that allow for a better understanding on the role of CdS in cascaded CdS/CdSe-based cells. In particular, these results are very important for the design of semiconductor sensitizers for efficient charge separation, thus further improvement of SSCs.

From Chapter 3, we learnt that the energy level matching at the interface of semiconductor sensitizer and metal oxide (a type-II band alignment) is crucial for efficient charge separation. To achieve this favorable band alignment, the band gap of a semiconductor sensitizer could be engineered either by tuning the size of QDs, the most commonly used method, or by following a compositional synthesis approach. Among these, the compositional synthesis approach was attempted to effectively tune the optical properties of semiconductor-sensitized metal oxides for using as photoanode for SSCs. As an example, the ternary solid solution of CdS_xSe_{1-x} was successfully synthesized by alternate deposition of CdS and CdSe by SILAR under ambient conditions and used as photoanode in photoelectrochemical cells for the first time. By controlling the deposition parameters, the optical band gap and consequently the band energy levels of CdS_xSe_{1-x} can feasibly be adjusted between the energy levels of CdSe and CdS of similar dimensions. The as-prepared amorphous CdS_xSe_{1-x} on TiO_2 as photoanode exhibits excellent photovoltaic performance when used as a light absorber for SSCs, which is comparable to the more commonly studied cascaded CdS/CdSe electrodes. This finding provides a viable alternative approach to tune the energetics of semiconductor sensitizers with the metal oxide at their interfaces. This method could be extended to other suitable semiconductor sensitizer systems. As a result, the efficient light absorption and charge separation, especially the issues of charge separation in narrow band gap semiconductor sensitizers-based cells could be adequately solved.

Although the CdSe-sensitized TiO_2 cells show promising performance, some very important semiconductor sensitizers cannot be used with TiO_2 because of its high CBM. Therefore, commercially available SnO_2 nanoparticles of size 10-40 nm was used here to make mesoporous electrode which has a lower CBM and superior

electron mobility than the TiO_2. The low CBM of SnO_2 facilitates the electron injection from sensitizer to the electrode, and the ~100 times higher electron mobility in SnO_2 makes the charge collection very efficient. As a result, the charge recombination in SnO_2-based cells was significantly suppressed and unprecedented photocurrent densities of 17.40 mA cm^{-2} and 18.37 mA cm^{-2} were observed using CdS/CdSe and CdSe-sensitized SnO_2 mesoscopic electrodes as photoanode, respectively, for SSCs. The IPCE of close to 80% over almost the entire visible spectral region suggests highly efficient charge separation and collection. In addition, the suppressed recombination of the injected charge at the interfaces of SnO_2 and sensitizers leads to the V_{oc} of the SnO_2-based cells not far from that obtained by TiO_2-based SSCs, despite the much lower CBM of SnO_2. While the use of SnO_2 is very successful from the aspect of photocurrent (j_{sc}), its efficiency still lags behind that of TiO_2 cells due to relatively low V_{oc}, presumably by the low CBM of SnO_2. Alternative hole-transporting materials with more positive potential are highly desired in this regard.

As the charge separation in the CdSe-sensitized SnO_2 cells (discussed in Chapter 5) was very efficient, the inherent excellent properties of SnO_2 could be utilized for efficient charge separation in narrow band gap PbS sensitizer-based cells. Because of the lower CBM and larger optical band gap of SnO_2 as compared to TiO_2, charge injection from PbS QDs with much smaller band gap energies could be favoured and the spectral response could be shifted to infrared region. In addition, these features make SnO_2 an ideal material for multiple exciton generation and collection in device, in which quantum yield greater than 100% could possibly be achieved, thus we could go beyond the Shockley-Queisser limit. In this work, using SILAR deposited PbS, caped with CdS, pronounced charge separation of the infrared photons was observed

beyond 1100 nm. In addition, utilizing the inherent much higher affinity for the growth of PbS on SnO_2 surface and following a rigorous interfacial engineering using a CdS buffer layer sandwiched between SnO_2 and PbS, and a ZnS passivation layer on the outmost surface of the electrode, photocurrent densities up to 17.38 mA cm^{-2} and power conversion efficiency of 2.23% were attained, which is much superior to that of TiO_2 tested under similar conditions and represents one of the highest efficiencies reported for PbS-sensitized liquid junction solar cells. However, the quantum efficiency of PbS-sensitized SnO_2 solar cells is still much lower than unity compared with the CdSe-sensitized counterparts and the maximum internal quantum yield is determined to be only ~70%. Therefore, an insightful understanding of the loss mechanism, especially the interface of SnO_2 and PbS would be of great importance for further improving the device performance, and ultimately achieving charge carrier multiplication and collection in narrow band gap semiconductor-sensitized mesoscopic solar cells considering the superb properties of SnO_2 observed herein.

Motivated by the promising performance of the SnO_2-based cells, a simple facile method, the electrochemical anodization was devised to make tin oxide nanoparticles. Using the as-prepared $Sn_6O_4(OH)_4$ primary nanoparticles as building block, various nanostructures of SnO and SnO_2 with tunable shape and sizes, such as solid/hollow spheres and hollow cubes/polyhedrons were successfully synthesized by a low-temperature aging step. Among these, the solid and hollow spheres were synthesized by self-assembly of the as-prepared $Sn_6O_4(OH)_4$ crystallites of grain size of 5-6 nm and ~4 nm, respectively, in a dilute ethanolic colloidal solution by Ostwald ripening. However, it is believed the oriented attachment and simultaneous Ostwald ripening-assisted hollowing process determines the growth of the hollow cubes and

polyhedrons when concentrated $Sn_6O_4(OH)_4$ crystallites were used in ethanol or in a mixture of ethanol and ethylene glycol, respectively. The directional growth of the resulting polyhedrons in the presence of hydrophobic EG is yet to be clarified and a systematic study is required to understand the mechanism. As the anodization reaction proceeds non-intermittently under ambient conditions, and only a low-temperature post-treatment is required to synthesis different shapes and sizes, it provides a facile and economic way of making nanostructured tin oxide on a large scale. A sequence of phase transition from the as-prepared $Sn_6O_4(OH)_4$ to SnO could be observed in a thermal dehydration process at 300 °C in the annealing step, followed by the conversion of these nanostructures into to SnO_2 at relatively high temperature. Among these, the mesoporous SnO_2 solid spheres were tested as a photoanode material for SSCs, which demonstrated promising photovoltaic performance when CdSe was used as sensitizer to harvest photons in the solar spectrum.

In 2010, the best efficiency of SSCs was around 4% (using S^{2-}/S_x^{2-} electrolyte and CdS, CdSe sensitizers). With the exploration of novel strategies for material synthesis both for the semiconductor sensitizers and semiconducting metal oxides, and the implementation of the best available device structures, the efficiency of SSCs has been rapidly increased to 5.42% by the year 2012. It is expected that a deeper understanding of factors dictating the operation of SSCs, such as alternative redox mediators with high redox potential, charge separation at PbS/SnO_2 interface, *etc*., would expedite the further rise of power conversion efficiency of SSCs. With the aforementioned advancement, we believe that SSCs will be developed into a credible alternative to the widely studied and commercialized photovoltaic technologies.

8.2 Recommendations

While remarkable progress has been made on the performance of SSCs in past few years, some important issues are still to be resolved, especially for the SnO_2-based cells which have low fill factor and V_{oc}. Therefore, in order to further improve the performance of SSCs, much effort is needed to optimize different cell constituents along with insightful understanding of their photoelectrochemical and photophysical properties. For instance, based on this study, the following routes can be pursued in future study.

8.2.1 Surface treatment of SnO_2 and preparation of SnO_2 blocking layer

The mesoporous SnO_2 electrodes is known to have higher surface states than that of the TiO_2 counterpart.[26,118] Therefore, it requires a systematic study, especially on the modification of its mesoporous surfaces to understand the reasons for hindered performance as photoanode in SSCs. Chaiya *et al.* have exploited that ultrathin layer of Al_2O_3 deposited via atomic layer deposition (ALD) on SnO_2 photoanodes in DSCs increases the lifetimes of injected electrons by more than 2 orders of magnitude and the overall energy conversion efficiency increases by approximately 5-fold.[118] The increase of device performance was appeared to arise primarily from passivation of reactive, low-energy tin-oxide surface states, with band edge shifts and tunnelling-based blocking behaviour. Hence, SnO_2 electrodes treated with higher band gap semiconductors than that of TiO_2 such as Al_2O_3. ZrO_2, *etc.* could be used for further improvement of SSCs. Utilizing these treated SnO_2 electrodes, the narrow band gap PbS could be used for further improvement of infrared light harvesting and the desired MEG might be a real possibility in SSCs.

In addition, a SnO_2 blocking layer will be beneficial, especially for exploring the hole transporting materials with faster charge transfer kinetics, including cobalt bipyridyl complex ($Co(bpy)_3^{2+/3+}$) in SSCs; thus the photovoltage of the cells might be greatly improved.

8.2.2 Influence of solvent on the growth of $Sn_6O_4(OH)_4$ nanostructores

From Chapter 7, it was learnt that the post-treatment is a very important means for tuning the final shape and size of nanostructures. However, a good understanding on the interactions between the solvated small nanocrystallites is essential for the understanding of growth mechanism and for the design of novel nanostructured assemblies. As an example, the role of ethylene glycol on the morphology from rounded cubes of $Sn_6O_4(OH)_4$ to durian like large nanostructures is yet elucidated. An investigation should be carried out to explore the function of the solvents on nanocrystallites, especially on the interparticle interactions of nanocrystallites when solvent of different dielectric constants are used.

8.2.3 Role of Cu_2S in SSCs

It is frequently observed that cells made with Cu_2S cathodes show an enhancement of IPCE towards the long wavelength of photons, while the respective light absorption spectrum suggests that the long wavelength photons cannot be harvested by the photoanode itself. As reported by Gary Hodes and Flaisher,[61,217] the Cu_2S cathode is not stable, especially, mechanically they gradually fall off from the zinc matrix in brass. The Cu_2S is prepared by instantaneous reaction of exposed copper on brass sheet with polysulfide solution. It is suspected that the polysulfide

species can be reduced by the non-reacted copper in brass to form soluble Cu^{+} compounds in the electrolyte, which may migrate and adsorb onto the photoanode to ultimately form an unexpected deposition of Cu_2S. In speculation, a staggered type II band alignment between CdSe and Cu_2S may either give rise to an effective band gap as reported by Ning *et al.*[83] or the tiny amount Cu_2S adsorbed on photoanode under bias may harvest long wavelength photons defined by its band gap of ~1.20 eV. Hence, unambiguous understanding the role of Cu_2S on the photoanode would be an intriguing topic to design non-toxic and low cost light absorbers for the enhancement of long wavelength photons harvesting for SSCs.

9 References

1. U. S. Department of energy, Basic research needs for solar energy utilization. Report on the basic energy sciences workshop on solar energy utilization. 2005, Aprill 18- 25.

2. Energy outlook 2030, 2011, British Petroleum.

3. Green, M. A.; Emery, K.; Hishikawa, Y.; Warta, W.; Dunlop, E. D., Solar cell efficiency tables (version 39). *Prog. Photovol: Res. Appl.* 2012, 20, 12-20.

4. Shockley, W.; Queisser, H. J., Detailed balance limit of efficiency of p-n junction solar cells. *J. Appl. Phys.* 1961, 32, 510-519.

5. Hanna, M. C.; Nozik, A. J., Solar conversion efficiency of photovoltaic and photoelectrolysis cells with carrier multiplication absorbers. *J. Appl. Phys.* 2006, 100, 074510-8.

6. Guter, W.; Schone, J.; Philipps, S. P.; Steiner, M.; Siefer, G.; Wekkeli, A.; Welser, E.; Oliva, E.; Bett, A. W.; Dimroth, F., Current-matched triple-junction solar cell reaching 41.1% conversion efficiency under concentrated sunlight. *Appl. Phys. Lett.* 2009, 94, 223504-3.

7. U.S. Geological Survey, 2012, Mineral commodity summaries 2012: U.S. Geological Survey, 198p

8. Brown, G. F.; Wu, J., Third generation photovoltaics. *Laser & Photon. Rev.* 2009, 3, 394-405.

9. Luque, A.; Martí, A.; Bett, A.; Andreev, V. M.; Jaussaud, C.; Van Roosmalen, J. A. M.; et, a., Fullspectrum: a new PV wave making more efficient use of the solar spectrum. *Sol. Energy Mater. Sol. Cells* 2005, 87, 467-479.

10. O'Regan, B.; Grätzel, M., A low-cost, high-efficiency solar cell based on dye-sensitized colloidal TiO_2 films. *Nature* 1991, 353, 737-740.

11. Yella, A.; Lee, H.-W.; Tsao, H. N.; Yi, C.; Chandiran, A. K.; Nazeeruddin, M. K.; Diau, E. W.-G.; Yeh, C.-Y.; Zakeeruddin, S. M.; Grätzel, M., Porphyrin-sensitized solar cells with cobalt (II/III)–based redox electrolyte exceed 12% efficiency. *Science* 2011, 334, 629-634.

12. Pan, Z.; Zhang, H.; Cheng, K.; Hou, Y.; Hua, J.; Zhong, X., Highly efficient inverted type-I CdS/CdSe core/shell structure QD-sensitized solar cells. *ACS Nano* 2012, 6, 3982-3991.

13. Santra, P. K.; Kamat, P. V., Mn-doped quantum dot sensitized solar cells: A strategy to boost efficiency over 5%. *J. Am. Chem. Soci.* 2012, 134, 2508-2511.

14. Zhang, H.; Cheng, K.; Hou, Y. M.; Fang, Z.; Pan, Z. X.; Wu, W. J.; Hua, J. L.; Zhong, X. H., Efficient CdSe quantum dot-sensitized solar cells prepared by a postsynthesis assembly approach. *Chem. Commun.* 2012, 48, 11235-11237.

15. Sambur, J. B.; Novet, T.; Parkinson, B. A., Multiple exciton collection in a sensitized photovoltaic system. *Science* 2010, 330, 63-66.

16. Semonin, O. E.; Luther, J. M.; Choi, S.; Chen, H.-Y.; Gao, J.; Nozik, A. J.; Beard, M. C., Peak external photocurrent quantum efficiency exceeding 100% via MEG in a quantum dot solar cell. *Science* 2011, 334, 1530-1533.

17. Hodes, G., Comparison of dye- and semiconductor-sensitized porous nanocrystalline liquid junction solar cells. *J. Phys. Chem. C* 2008, 112, 17778-17787.

18. Lee, Y. L.; Lo, Y. S., Highly efficient quantum-dot-sensitized solar cell based on co-sensitization of CdS/CdSe. *Adv. Funct. Mater.* 2009, 19, 604-609.

19. Chi, C.-F.; Cho, H.-W.; Teng, H.; Chuang, C.-Y.; Chang, Y.-M.; Hsu, Y.-J.; Lee, Y.-L., Energy level alignment, electron injection, and charge recombination characteristics in CdS/CdSe cosensitized TiO_2 photoelectrode. *Appl. Phys. Lett.* 2011, 98, 012101-3.

20. Leventis, H. C.; O'Mahony, F.; Akhtar, J.; Afzaal, M.; O'Brien, P.; Haque, S. A., Transient optical studies of interfacial charge transfer at nanostructured metal oxide/PbS quantum dot/organic hole conductor heterojunctions. *J. Am. Chem. Soc.* 2010, 132, 2743-2750.

21. Forro, L.; Chauvet, O.; Emin, D.; Zuppiroli, L.; Berger, H.; Levy, F., High mobility n-type charge carriers in large single crystals of anatase (TiO_2). *J. Appl. Phys.* 1994, 75, 633-635.

22. Jarzebski, Z. M.; Marton, J. P., Physical properties of SnO_2 materials. *J. Electrochem. Soc.* 1976, 123, 299C-310C.

23. Hossain, M. A.; Yang, G.; Parameswaran, M.; Jennings, J. R.; Wang, Q., Mesoporous SnO_2 spheres synthesized by electrochemical anodization and their application in CdSe-sensitized aolar cells. *J. Phys. Chem. C* 2010, 114, 21878-21884.

24. Ito, S.; Murakami, T. N.; Comte, P.; Liska, P.; Grätzel, C.; Nazeeruddin, M. K.; Grätzel, M., Fabrication of thin film dye sensitized solar cells with solar to electric power conversion efficiency over 10%. *Thin Solid Films* 2008, 516, 4613-4619.

25. Ito, S.; Liska, P.; Comte, P.; Charvet, R.; Pechy, P.; Bach, U.; Schmidt-Mende, L.; Zakeeruddin, S. M.; Kay, A.; Nazeeruddin, M. K.; Gratzel, M., Control of dark current in photoelectrochemical ($TiO_2/I^-/I_3^-$) and dye-sensitized solar cells. *Chem. Commun.* 2005, 4351-4353.

26. Snaith, H. J.; Ducati, C., SnO_2-based dye-sensitized hybrid solar cells exhibiting near unity absorbed photon-to-electron conversion efficiency. *Nano Lett.* 2010, 10, 1259-1265.

27. Gopidas, K. R.; Bohorquez, M.; Kamat, P. V., Photophysical and photochemical aspects of coupled semiconductors: charge-transfer processes in colloidal cadmium sulfide-titania and cadmium sulfide-silver(I) iodide systems. *J. Phys. Chem.* 1990, 94, 6435-6440.

28. Lee, H.; Wang, M.; Chen, P.; Gamelin, D. R.; Zakeeruddin, S. M.; Grätzel, M.; Nazeeruddin, M. K., Efficient CdSe quantum dot-sensitized solar cells prepared by an improved successive ionic layer adsorption and reaction process. *Nano Lett.* 2009, 9, 4221-4227.

29. Chang, J.-Y.; Su, L.-F.; Li, C.-H.; Chang, C.-C.; Lin, J.-M., Efficient "green" quantum dot-sensitized solar cells based on Cu_2S-$CuInS_2$-ZnSe architecture. *Chem. Commun.* 2012, 48, 4848-4850.

30. Chang, J. A.; Rhee, J. H.; Im, S. H.; Lee, Y. H.; Kim, H.-j.; Seok, S. I.; Nazeeruddin, M. K.; Gratzel, M., High-performance nanostructured Inorganic−organic heterojunction solar cells. *Nano Lett.* 2010, 10, 2609-2612.

31. Wang, Y.; Meng, G.; Zhang, L.; Liang, C.; Zhang, J., Catalytic growth of large-scale single-crystal CdS nanowires by physical evaporation and their photoluminescence. *Chem. Mater.* 2002, 14, 1773-1777.

32. Liu, L.; Peng, Q.; Li, Y., An effective oxidation route to blue emission CdSe quantum dots. *Inorg. Chem.* 2008, 47, 3182-3187.

33. Peterson, J. J.; Krauss, T. D., Fluorescence spectroscopy of single lead sulfide quantum dots. *Nano Lett.* 2006, 6, 510-514.

34. Kamat, P. V., Quantum dot solar cells. Semiconductor nanocrystals as light harvesters. *J. Phys. Chem. C* 2008, 112, 18737-18753.

35. Niitsoo, O.; Sarkar, S. K.; Pejoux, C.; Rühle, S.; Cahen, D.; Hodes, G., Chemical bath deposited CdS/CdSe-sensitized porous TiO_2 solar cells. *J. Photoch. Photobio. A* 2006, 181, 306-313.

36. Diguna, L. J.; Shen, Q.; Kobayashi, J.; Toyoda, T., High efficiency of CdSe quantum-dot-sensitized TiO_2 inverse opal solar cells. *Appl. Phys. Lett.* 2007, 91, 023116-3.

37. Shen, Q.; Kobayashi, J.; Diguna, L. J.; Toyoda, T., Effect of ZnS coating on the photovoltaic properties of CdSe quantum dot-sensitized solar cells. *J. Appl. Phys.* 2008, 103.

38. Gorer, S.; Hodes, G., Quantum size effects in the study of chemical solution deposition mechanisms of semiconductor films. *J. Phys. Chem.* 1994, 98, 5338-5346.

39. Shen, Q.; Arae, D.; Toyoda, T., Photosensitization of nanostructured TiO_2 with CdSe quantum dots: effects of microstructure and electron transport in TiO_2 substrates. *J. Photoch. Photobio. A* 2004, 164, 75-80.

40. Lee, H.; Leventis, H. C.; Moon, S.-J.; Chen, P.; Ito, S.; Haque, S. A.; Torres, T.; Nüesch, F.; Geiger, T.; Zakeeruddin, S. M.; Grätzel, M.; Nazeeruddin, M. K., PbS and CdS quantum dot-sensitized solid-state solar cells: "Old concepts, new results". *Adv. Funct. Mater.* 2009, 19, 2735-2742.

41. Ristov, M.; Sinadinovski, G.; Grozdanov, I., Chemical deposition of Cu_2O thin films. *Thin Solid Films* 1985, 123, 63-67.

42. Nicolau, Y. F., Solution deposition of thin solid compound films by a successive ionic-layer adsorption and reaction process. *Appl. Surf. Sci.* 1985, 22-23, 1061-1074.

43. Nicolau, Y. F.; Menard, J. C., Solution growth of ZnS, CdS and $Zn_{1-x}Cd_xS$ thin films by the successive ionic-layer adsorption and reaction process; growth mechanism. *J. Crystal Growth* 1988, 92, 128-142.

44. Lee, Y.-L.; Huang, B.-M.; Chien, H.-T., Highly efficient CdSe-sensitized TiO_2 photoelectrode for quantum-dot-sensitized solar cell applications. *Chem. Mater.* 2008, 20, 6903-6905.

45. González-Pedro, V.; Xu, X.; Mora-Seró, I.; Bisquert, J., Modeling high-efficiency quantum dot sensitized solar cells. *ACS Nano* 2010, 4, 5783-5790.

46. Yang, S.-M.; Huang, C.-H.; Zhai, J.; Wang, Z.-S.; Jiang, L., High photostability and quantum yield of nanoporous TiO_2 thin film electrodes co-sensitized with capped sulfides. *J. Mater. Chem.* 2002, 12, 1459-1464.

47. Mora-Seró, I.; Giménez, S.; Fabregat-Santiago, F.; Gómez, R.; Shen, Q.; Toyoda, T.; Bisquert, J., Recombination in quantum dot sensitized solar cells. *Acc. Chem. Res.* 2009, 42, 1848-1857.

48. Hossain, M. A.; Jennings, J. R.; Koh, Z. Y.; Wang, Q., Carrier generation and collection in CdS/CdSe-sensitized SnO_2 solar cells exhibiting unprecedented photocurrent densities. *ACS Nano* 2011, 5, 3172-3181.

49. Guijarro, N.; Campina, J. M.; Shen, Q.; Toyoda, T.; Lana-Villarreal, T.; Gomez, R., Uncovering the role of the ZnS treatment in the performance of quantum dot sensitized solar cells. *Phys. Chem. Chem. Phys.* 2011, 13, 12024-12032.

50. Giménez, S.; Mora-Seró, I.; MacOr, L.; Guijarro, N.; Lana-Villarreal, T.; Gómez, R.; Diguna, L. J.; Shen, Q.; Toyoda, T.; Bisquert, J., Improving the performance of colloidal quantum-dot-sensitized solar cells. *Nanotechnology* 2009, 20, 295204.

51. Chang, C.-H.; Lee, Y.-L., Chemical bath deposition of CdS quantum dots onto mesoscopic TiO_2 films for application in quantum-dot-sensitized solar cells. *Appl. Phys. Lett.* 2007, 91, 053503-3.

52. Lee, Y. L.; Chang, C. H., Efficient polysulfide electrolyte for CdS quantum dot-sensitized solar cells. *J. Power Sources* 2008, 185, 584-588.

53. Tachibana, Y.; Akiyama, H. Y.; Ohtsuka, Y.; Torimoto, T.; Kuwabata, S., CdS quantum dots sensitized TiO_2 sandwich type photoelectrochemical solar cells. *Chem. Lett.* 2007, 36, 88-89.

54. Lee, H. J.; Chen, P.; Moon, S.-J.; Sauvage, F. d. r.; Sivula, K.; Bessho, T.; Gamelin, D. R.; Comte, P.; Zakeeruddin, S. M.; Seok, S. I.; Grätzel, M.; Nazeeruddin, M. K., Regenerative PbS and CdS quantum dot sensitized solar cells with a cobalt complex as hole mediator. *Langmuir* 2009, 25, 7602-7608.

55. Hodes, G.; Albu-Yaron, A.; Decker, F.; Motisuke, P., Three-dimensional quantum-size effect in chemically deposited cadmium selenide films. *Phys. Rev. B* 1987, 36, 4215-4221.

56. Plass, R.; Pelet, S.; Krueger, J.; Grätzel, M.; Bach, U., Quantum dot sensitization of organic-inorganic hybrid solar cells. *J. Phys. Chem. B* 2002, 106, 7578-7580.

57. Chakrapani, V.; Baker, D.; Kamat, P. V., Understanding the role of the sulfide redox couple (S^{2-}/S_n^{2-}) in quantumdot-sensitized solar sells. *J. Am. Chem. Soc.* 2011, 133, 9607-9615.

58. Li, L.; Yang, X.; Gao, J.; Tian, H.; Zhao, J.; Hagfeldt, A.; Sun, L., Highly efficient CdS quantum dot-sensitized solar cells based on a modified polysulfide electrolyte. *J. Am. Chem. Soc.* 2011, 133, 8458-8460.

59. Jovanovski, V.; González-Pedro, V.; Giménez, S.; Azaceta, E.; Cabañero, G.; Grande, H.; Tena-Zaera, R.; Mora-Seró, I.; Bisquert, J., A sulfide/polysulfide-based ionic liquid electrolyte for quantum dot-sensitized solar cells. *J. Am. Chem. Soci.* 2011, 133, 20156-20159.

60. Yang, Z.; Chen, C.-Y.; Liu, C.-W.; Li, C.-L.; Chang, H.-T., Quantum dot–sensitized solar cells featuring CuS/CoS electrodes provide 4.1% efficiency. *Adv. Energy Mater.* 2011, 1, 259-264.

61. Hodes, G.; Manassen, J.; Cahen, D., Electrocatalytic electrodes for the polysulfide redox system. *J. Electrochem. Soc.* 1980, 127, 544-549.

62. Tachan, Z.; Shalom, M.; Hod, I.; Rühle, S.; Tirosh, S.; Zaban, A., PbS as a highly catalytic counter electrode for polysulfide-based quantum dot solar cells. *J. Phys. Chem. C* 2011, 115, 6162-6166.

63. Zhang, Q.; Guo, X.; Huang, X.; Huang, S.; Li, D.; Luo, Y.; Shen, Q.; Toyoda, T.; Meng, Q., Highly efficient CdS/CdSe-sensitized solar cells controlled by the structural properties of compact porous TiO_2 photoelectrodes. *Phys. Chem. Chem. Phys.* 2011, 13, 4659-4667.

64. Fan, S.-Q.; Fang, B.; Kim, J. H.; Kim, J.-J.; Yu, J.-S.; Ko, J., Hierarchical nanostructured spherical carbon with hollow core/mesoporous shell as a highly efficient counter electrode in CdSe quantum-dot-sensitized solar cells. *Appl. Phys. Lett.* 2010, 96, 063501-3.

65. Hossain, M. A.; Jennings, J. R.; Mathews, N.; Wang, Q., Band engineered ternary solid solution CdS_xSe_{1-x}-sensitized mesoscopic TiO_2 solar cells. *Phys. Chem. Chem. Phys.* 2012, 14, 7154-7161.

66. Hossain, M. A.; Koh, Z. Y.; Wang, Q., PbS/CdS-sensitized mesoscopic SnO_2 solar cells for enhanced infrared light harnessing. *Phys. Chem. Chem. Phys.* 2012, 14, 7367-7374.

67. Tauc, J.; Menth, A.; Wood, D. L., Optical and magnetic investigations of the localized states in semiconducting glasses. *Phys. Rev. Lett.* 1970, 25, 749-752.

68. Fabregat-Santiago, F.; Garcia-Belmonte, G.; Mora-Seró, I.; Bisquert, J., Characterization of nanostructured hybrid and organic solar cells by impedance spectroscopy. *Phys. Chem. Chem. Phys.* 2011, 13, 9083-9118.

69. Vogel, R.; Hoyer, P.; Weller, H., Quantum-sized PbS, CdS, Ag_2S, Sb_2S_3, and Bi_2S_3 particles as sensitizers for various nanoporous wide-bandgap semiconductors. *J. Phys. Chem.* 1994, 98, 3183-3188.

70. Nozik, A. J., Quantum dot solar cells. *Physica E* 2002, 14, 115-120.

71. Yu, W. W.; Qu, L.; Guo, W.; Peng, X., Experimental determination of the extinction coefficient of CdTe, CdSe, and CdS nanocrystals. *Chem. Mater.* 2003, 15, 2854-2860.

72. Deng, M.; Huang, S.; Zhang, Q.; Li, D.; Luo, Y.; Shen, Q.; Toyoda, T.; Meng, Q., Screen-printed Cu_2S-based counter electrode for quantum-dot-sensitized solar cell. *Chem. Lett.* 2010, 39, 1168-1170.

73. Xu, J.; Yang, X.; Wang, H.; Chen, X.; Luan, C.; Xu, Z.; Lu, Z.; Roy, V. A. L.; Zhang, W.; Lee, C.-S., Arrays of $ZnO/Zn_xCd_{1-x}Se$ nanocables: Band gap engineering and photovoltaic applications. *Nano Lett.* 2011, 11, 4138-4143.

74. Huang, X.; Huang, S.; Zhang, Q.; Guo, X.; Li, D.; Luo, Y.; Shen, Q.; Toyoda, T.; Meng, Q., A flexible photoelectrode for CdS/CdSe quantum dot-sensitized solar cells (QDSSCs). *Chem. Commun.* 2011, 47, 2664-2666.

75. Peter, L. M.; Riley, D. J.; Tull, E. J.; Wijayantha, K. G. U., Photosensitization of nanocrystalline TiO_2 by self-assembled layers of CdS quantum dots. *Chem. Commun.* 2002, 1030-1031.

76. Robel, I.; Subramanian, V.; Kuno, M.; Kamat, P. V., Quantum dot solar cells. Harvesting light energy with CdSe nanocrystals molecularly linked to mesoscopic TiO_2 films. *J. Am. Chem. Soc.* 2006, 128, 2385-2393.

77. Guijarro, N.; Lana-Villarreal, T.; Shen, Q.; Toyoda, T.; Gómez, R., Sensitization of titanium dioxide photoanodes with cadmium selenide quantum dots prepared by SILAR: Photoelectrochemical and carrier dynamics studies. *J. Phys. Chem. C* 2010, 114, 21928-21937.

78. Lee, H. J.; Bang, J.; Park, J.; Kim, S.; Park, S.-M., Multilayered semiconductor (CdS/CdSe/ZnS)-sensitized TiO_2 mesoporous solar sells: All prepared by successive ionic layer adsorption and reaction processes. *Chem. Mater.* 2010, 22, 5636-5643.

79. Radich, J. G.; Dwyer, R.; Kamat, P. V., Cu_2S reduced graphene oxide composite for high-efficiency quantum dot solar cells. Overcoming the redox limitations of S^{2-}/S_n^{2-} at the counter electrode. *J. Phys. Chem. Lett.* 2011, 2, 2453-2460.

80. Zhu, G.; Pan, L.; Xu, T.; Sun, Z., CdS/CdSe-cosensitized TiO_2 photoanode for quantum-dot-sensitized solar cells by a microwave-assisted chemical bath deposition method. *Appl. Mater. Interfaces* 2011, 3, 3146-3151.

81. Zewdu, T.; Clifford, J. N.; Hernandez, J. P.; Palomares, E., Photo-induced charge transfer dynamics in efficient TiO_2/CdS/CdSe sensitized solar cells. *Energy Environ. Sci.* 2011, 4, 4633-4638.

82. Lin, K.-H.; Chuang, C.-Y.; Lee, Y.-Y.; Li, F.-C.; Chang, Y.-M.; Liu, I. P.; Chou, S.-C.; Lee, Y.-L., Charge transfer in the heterointerfaces of CdS/CdSe co-sensitized TiO_2 photoelectrode. *J. Phys. Chem. C* 2011, 116, 1550-1555.

83. Ning, Z.; Tian, H.; Yuan, C.; Fu, Y.; Qin, H.; Sun, L.; Ågren, H., Solar cells sensitized with type-II ZnSe-CdS core/shell colloidal quantum dots. *Chem. Commun.* 2011, 47, 1536-1538.

84. Bisquert, J., Theory of the impedance of electron diffusion and recombination in a thin layer. *J. Phys. Chem. B* 2002, 106, 325-333.

85. Wang, Q.; Ito, S.; Grätzel, M.; Fabregat-Santiago, F.; Mora-Seró, I.; Bisquert, J.; Bessho, T.; Imai, H., Characteristics of high efficiency dye-sensitized solar cells. *J. Phys. Chem. B* 2006, 110, 25210-25221.

86. Hod, I.; González-Pedro, V.; Tachan, Z.; Fabregat-Santiago, F.; Mora-Seró, I.; Bisquert, J.; Zaban, A., Dye versus quantum dots in sensitized solar cells: Participation of quantum dot Absorber in the recombination process. *J. Phys. Chem. Lett.* 2011, 3032-3035.

87. Goebl, J. A.; Black, R. W.; Puthussery, J.; Giblin, J.; Kosel, T. H.; Kuno, M., Solution-based II−VI core/shell nanowire heterostructures. *J. Am. Chem. Soc.* 2008, 130, 14822-14833.

88. Wei, S. H.; Zhang, S. B.; Zunger, A., First-principles calculation of band offsets, optical bowings, and defects in CdS, CdSe, CdTe, and their alloys. *J. Appl. Phys.* 2000, 87, 1304-1311.

89. Li, J.; Wang, L.-W., First principle study of core/shell structure quantum dots. *Appl. Phys. Lett.* 2004, 84, 3648-3650.

90. Tvrdy, K.; Frantsuzov, P. A.; Kamat, P. V., Photoinduced electron transfer from semiconductor quantum dots to metal oxide nanoparticles. *P Natl. Acad. Sci. USA* 2011, 108, 29-34.

91. Chirilă, A.; Buecheler, S.; Pianezzi, F.; Bloesch, P.; Gretener, C.; Uhl, A. R.; et, a., Highly efficient Cu(In,Ga)Se_2 solar cells grown on flexible polymer films. *Nat Mater* 2011, 10, 857-861.

92. Jackson, P.; Hariskos, D.; Lotter, E.; Paetel, S.; Wuerz, R.; Menner, R.; Wischmann, W.; Powalla, M., New world record efficiency for Cu(In,Ga)Se_2 thin-film solar cells beyond 20%. *Prog. Photovolt. Res. Appl.* 2011, 19, 894-897.

93. Kongkanand, A.; Tvrdy, K.; Takechi, K.; Kuno, M.; Kamat, P. V., Quantum dot solar cells. Tuning photoresponse through size and shape control of CdSe−TiO_2 architecture. *J. Am. Chem. Soc.* 2008, 130, 4007-4015.

94. Sung, T. K.; Kang, J. H.; Jang, D. M.; Myung, Y.; Jung, G. B.; Kim, H. S.; Jung, C. S.; Cho, Y. J.; Park, J.; Lee, C.-L., CdSSe layer-sensitized TiO_2 nanowire arrays as efficient photoelectrodes. *J. Mater. Chem.* 2011, 21, 4553-4561.

95. Mane, R. S.; Lokhande, C. D.; Todkar, V. V.; Chung, H.; Yoon, M.-Y.; Han, S.-H., Photosensitization of nanocrystalline TiO_2 film electrode with cadmium sulphoselenide. *Appl. Surf. Sci.* 2007, 253, 3922-3926.

96. Shu, T.; Zhou, Z.; Wang, H.; Liu, G.; Xiang, P.; Rong, Y.; Han, H.; Zhao, Y., Efficient quantum dot-sensitized solar cell with tunable energy band $CdSe_xS_{1-x}$ quantum dots. *J. Mater. Chem.* 2012, 22, 10525-10529.

97. Xu, F.; Ma, X.; Kauzlarich, S. M.; Navrotsky, A., Enthalpies of formation of CdS_xSe_{1-x} solid solutions. *J. Mater. Res.* 2009, 24, 1368-1374.

98. Pan, A.; Liu, R.; Wang, F.; Xie, S.; Zou, B.; Zacharias, M.; Wang, Z. L., High-quality alloyed CdS_xSe_{1-x} whiskers as waveguides with tunable stimulated emission. *J. Phys. Chem. B* 2006, 110, 22313-22317.

99. Gu, F.; Yang, Z.; Yu, H.; Xu, J.; Wang, P.; Tong, L.; Pan, A., Spatial bandgap engineering along single alloy nanowires. *J. Am. Chem. Soc.* 2011, 133, 2037-2039.

100. Swafford, L. A.; Weigand, L. A.; Bowers Ii, M. J.; McBride, J. R.; Rapaport, J. L.; Watt, T. L.; Dixit, S. K.; Feldman, L. C.; Rosenthal, S. J., Homogeneously alloyed CdS_xSe_{1-x} nanocrystals: Synthesis, characterization, and composition/size-dependent band gap. *J. Am. Chem. Soc.* 2006, 128, 12299-12306.

101. Myung, Y.; Jang, D. M.; Sung, T. K.; Sohn, Y. J.; Jung, G. B.; Cho, Y. J.; Kim, H. S.; Park, J., Composition-tuned ZnO-CdSSe core-shell nanowire arrays. *ACS Nano* 2010, 4, 3789-3800.

102. Jang, E.; Jun, S.; Pu, L., High quality CdSeS nanocrystals synthesized by facile single injection process and their electroluminescence. *Chem. Commun.* 2003, 9, 2964-2965.

103. Ouyang, J.; Vincent, M.; Kingston, D.; Descours, P.; Boivineau, T.; Zaman, M. B.; Wu, X.; Yu, K., Noninjection, one-pot synthesis of photoluminescent colloidal homogeneously aloyed CdSeS quantum dots. *J. Phys. Chem. C* 2009, 113, 5193-5200.

104. Pan, A. L.; Yao, L.; Qin, Y.; Yang, Y.; Kim, D. S.; Yu, R.; Zou, B.; Werner, P.; Zacharias, M.; Gösele, U., Si-CdSSe core/shell nanowires with continuously tunable light emission. *Nano Lett.* 2008, 8, 3413-3417.

105. Ruberu, T. P. A.; Vela, J., Expanding the one-dimensional CdS–CdSe composition landscape: Axially anisotropic $CdS_{1-x}Se_x$ nanorods. *ACS Nano* 2011, 5, 5775-5784.

106. Pan, A.; Yang, H.; Liu, R.; Yu, R.; Zou, B.; Wang, Z., Color-tunable photoluminescence of alloyed CdS_xSe_{1-x} nanobelts. *J. Am. Chem. Soc.* 2005, 127, 15692-15693.

107. Junpeng, L.; Cheng, S.; Minrui, Z.; Mathews, N.; Hongwei, L.; Gin Seng, C.; Xinhai, Z.; Mhaisalkar, S. G.; Chorng Haur, S., Facile one-step synthesis of CdS_xSe_{1-x} nanobelts with uniform and controllable stoichiometry. *J. Phys. Chem. C* 2011, 115, 19538-19545.

108. Li, G.; Jiang, Y.; Wang, Y.; Wang, C.; Sheng, Y.; Jie, J.; Zapien, J. A.; Zhang, W.; Lee, S.-T., Synthesis of CdS_XSe_{1-X} nanoribbons with uniform and controllable compositions via sulfurization: Optical and electronic properties studies. *J. Phys. Chem. C* 2009, 113, 17183-17188.

109. Al-Salim, N.; Young, A. G.; Tilley, R. D.; McQuillan, A. J.; Xia, J., Synthesis of CdSeS nanocrystals in coordinating and noncoordinating solvents: solvent's role

in evolution of the optical and structural properties. *Chem. Mater.* 2007, 19, 5185-5193.

110. Garrett, M. D.; Dukes Iii, A. D.; McBride, J. R.; Smith, N. J.; Pennycook, S. J.; Rosenthal, S. J., Band edge recombination in CdSe, CdS and CdS_xSe_{1-x} alloy nanocrystals observed by ultrafast fluorescence upconversion: The effect of surface trap states. *J. Phys. Chem. C* 2008, 112, 12736-12746.

111. Ma, W.; Luther, J. M.; Zheng, H.; Wu, Y.; Alivisatos, A. P., Photovoltaic devices employing ternary PbS_xSe_{1-x} nanocrystals. *Nano Lett.* 2009, 9, 1699-1703.

112. Kang, J. H.; Myung, Y.; Choi, J. W.; Jang, D. M.; Lee, C. W.; Park, J.; Cha, E. H., Nb_2O_5 nanowire photoanode sensitized by a composition-tuned CdS_xSe_{1-x} shell. *J. Mater. Chem.* 2012, 22, 8413-8419.

113. Toyoda, T.; Oshikane, K.; Li, D.; Luo, Y.; Meng, Q.; Shen, Q., Photoacoustic and photoelectrochemical current spectra of combined CdS/CdSe quantum dots adsorbed on nanostructured TiO_2 electrodes, together with photovoltaic characteristics. *J. Appl. Phys.* 2010, 108, 114304-7.

114. Laverty, S. J.; Maguire, P. D., Low resistance transparent electrodes for large area flat display devices. *J. Vac. Sci. Technol. B* 2001, 19, 1-6.

115. Minami, T., Transparent conducting oxide semiconductors for transparent electrodes. *Semicond. Sci. Technol.* 2005, 20, S35-S44.

116. Lou, X. W.; Wang, Y.; Yuan, C.; Lee, J. Y.; Archer, L. A., Template-free synthesis of SnO_2 hollow nanostructures with high lithium storage capacity. *Adv. Mater.* 2006, 18, 2325-2329.

117. Wang, Y.; Zeng, H. C.; Lee, J. Y., Highly reversible lithium storage in porous SnO_2 nanotubes with coaxially grown carbon nanotube overlayers. *Adv. Mater.* 2006, 18, 645-649.

118. Prasittichai, C.; Hupp, J. T., Surface modification of SnO_2 photoelectrodes in dye-sensitized solar cells: Significant improvements in photovoltage via Al_2O_3 atomic layer deposition. *J. Phys. Chem. Lett.* 2010, 1, 1611-1615.

119. Liu, J.; Luo, T.; Mouli T, S.; Meng, F.; Sun, B.; Li, M., A novel coral-like porous SnO_2 hollow architecture: Biomimetic swallowing growth mechanism and enhanced photovoltaic property for dye-sensitized solar cell application. *Chem. Commun.* 2010, 46, 472-474.

120. Chiu, H. C.; Yeh, C. S., Hydrothermal synthesis of SnO_2 nanoparticles and their gas-sensing of alcohol. *J. Phys. Chem. C* 2007, 111, 7256-7259.

121. Han, X.; Jin, M.; Xie, S.; Kuang, Q.; Jiang, Z.; Jiang, Y.; Xie, Z.; Zheng, L., Synthesis of tin dioxide octahedral nanoparticles with exposed high-energy {221} facets and enhanced gas-sensing properties. *Angew. Chem. Int. Ed.* 2009, 48, 9180-9183.

122. Yu, C.; Yu, J. C.; Wang, F.; Wen, H.; Tang, Y., Growth of single-crystalline SnO_2 nanocubes via a hydrothermal route. *CrystEngComm* 2010, 12, 341-343.

123. Tiwana, P.; Docampo, P.; Johnston, M. B.; Snaith, H. J.; Herz, L. M., Electron mobility and injection dynamics in mesoporous ZnO, SnO_2, and TiO_2 films used in Dye-sensitized solar cells. *ACS Nano* 2011, 5, 5158-5166.

124. Gratzel, M., Photoelectrochemical cells. *Nature* 2001, 414, 338-344.

125. Hyun, B.-R.; Zhong, Y.-W.; Bartnik, A. C.; Sun, L.; Abruña, H. D.; Wise, F. W.; Goodreau, J. D.; Matthews, J. R.; Leslie, T. M.; Borrelli, N. F., Electron injection from colloidal PbS quantum dots into Titanium dioxide nanoparticles. *ACS Nano* 2008, 2, 2206-2212.

126. Li, G. S.; Zhang, D. Q.; Yu, J. C., A new visible-light photocatalyst: CdS quantum dots embedded mesoporous TiO_2. *Environ. Sci. Technol.* 2009, 43, 7079-7085.

127. Leschkies, K. S.; Beatty, T. J.; Kang, M. S.; Norris, D. J.; Aydil, E. S., Solar cells based on junctions between colloidal Pbse nanocrystals and thin ZnO films. *ACS Nano* 2009, 3, 3638-3648.

128. Castro, S. L.; Bailey, S. G.; Raffaelle, R. P.; Banger, K. K.; Hepp, A. F., Nanocrystalline chalcopyrite materials ($CuInS_2$ and $CuInSe_2$) via low-temperature pyrolysis of molecular single-source precursors. *Chem. Mater.* 2003, 15, 3142-3147.

129. Sudhagar, P.; Jung, J. H.; Park, S.; Lee, Y.-G.; Sathyamoorthy, R.; Kang, Y. S.; Ahn, H., The performance of coupled (CdS:CdSe) quantum dot-sensitized TiO_2 nanofibrous solar cells. *Electrochem. Commun.* 2009, 11, 2220-2224.

130. Zhai, T.; Fang, X.; Bando, Y.; Liao, Q.; Xu, X.; Zeng, H.; Ma, Y.; Yao, J.; Golberg, D., Morphology-dependent stimulated emission and field emission of ordered CdS nanostructure arrays. *ACS Nano* 2009, 3, 949-959.

131. Lee, Y.-L.; Chi, C.-F.; Liau, S.-Y., CdS/CdSe co-sensitized TiO_2 photoelectrode for efficient hydrogen generation in a photoelectrochemical cell. *Chem. Mater.* 2009, 22, 922-927.

132. Pijpers, J. J. H.; Koole, R.; Evers, W. H.; Houtepen, A. J.; Boehme, S.; de Mello Donegá, C.; Vanmaekelbergh, D.; Bonn, M., Spectroscopic studies of electron injection in quantum dot sensitized mesoporous oxide films. *J. Phys. Chem. C* 2010, 114, 18866-18873.

133. Yang, S. M.; Huang, C. H.; Zhai, J.; Wang, Z. S.; Jiang, L., High photostability and quantum yield of nanoporous TiO_2 thin film electrodes co-sensitized with capped sulfides. *J. Mater. Chem.* 2002, 12, 1459-1464.

134. Barea, E. M.; Shalom, M.; Giménez, S.; Hod, I.; Mora-Seró, I.; Zaban, A.; Bisquert, J., Design of injection and recombination in quantum dot sensitized solar cells. *J. Am. Chem. Soc.* 2010, 132, 6834-6839.

135. Halme, J.; Boschloo, G.; Hagfeldt, A.; Lund, P., Spectral characteristics of light harvesting, electron injection, and steady-state charge collection in pressed TiO_2 dye solar cells. *J. Phys. Chem. C* 2008, 112, 5623-5637.

136. Lobato, K.; Peter, L. M.; Würfel, U., Direct measurement of the internal electron quasi-Fermi level in dye sensitized solar cells using a titanium secondary electrode. *J. Phys. Chem. B* 2006, 110, 16201-16204.

137. Peter, L. M., Dye-sensitized nanocrystalline solar cells. *Phys. Chem. Chem. Phys.* 2007, 9, 2630-2642.

138. Jennings, J. R.; Peter, L. M., A reappraisal of the electron diffusion length in solid-state dye-sensitized solar cells. *J. Phys. Chem. C* 2007, 111, 16100-16104.

139. Enright, B.; Fitzmaurice, D., Spectroscopic determination of electron and hole effective masses in a nanocrystalline semiconductor Film. *J. Phys. Chem.* 1996, 100, 1027-1035.

140. Button, K. J.; Fonstad, C. G.; Dreybrodt, W., Determination of the electron masses in stannic oxide by submillimeter cyclotron resonance. *Phys. Rev. B* 1971, 4, 4539-4542.

141. Pattantyus-Abraham, A. G.; Kramer, I. J.; Barkhouse, A. R.; Wang, X.; Konstantatos, G.; Debnath, R.; Levina, L.; Raabe, I.; Nazeeruddin, M. K.; Grätzel, M.; Sargent, E. H., Depleted-heterojunction colloidal quantum dot solar cells. *ACS Nano* 2010, 4, 3374-3380.

142. Tang, J.; Kemp, K. W.; Hoogland, S.; Jeong, K. S.; Liu, H.; Levina, L.; Furukawa, M.; Wang, X.; Debnath, R.; Cha, D.; Chou, K. W.; Fischer, A.; Amassian, A.; Asbury, J. B.; Sargent, E. H., Colloidal-quantum-dot photovoltaics using atomic-ligand passivation. *Nat. Mater.* 2011, 10, 765-771.

143. Barkhouse, D. A. R.; Debnath, R.; Kramer, I. J.; Zhitomirsky, D.; Pattantyus-Abraham, A. G.; Levina, L.; Etgar, L.; Grätzel, M.; Sargent, E. H., Depleted bulk heterojunction colloidal quantum dot photovoltaics. *Adv. Mater.* 2011, 23, 3134-3138.

144. Snaith, H. J.; Stavrinadis, A.; Docampo, P.; Watt, A. A. R., Lead-sulphide quantum-dot sensitization of tin oxide based hybrid solar cells. *Solar Energy* 2011, 85, 1283-1290.

145. Braga, A.; Giménez, S.; Concina, I.; Vomiero, A.; Mora-Seró, I., Panchromatic sensitized solar cells based on metal sulfide quantum dots grown directly on nanostructured TiO_2 electrodes. *J. Phys.Chem. Lett.* 2011, 2, 454-460.

146. Im, S. H.; Kim, H.-J.; Kim, S. W.; Kim, S.-W.; Seok, S. I., All solid state multiply layered PbS colloidal quantum-dot-sensitized photovoltaic cells. *Energy Environ. Sci.* 2011, 4, 4181-4186.

147. Wise, F. W., Lead salt quantum dots: the limit of strong quantum confinement. *Accounts Chem. Res.* 2000, 33, 773-780.

148. Smith, D. K.; Luther, J. M.; Semonin, O. E.; Nozik, A. J.; Beard, M. C., Tuning the synthesis of ternary lead chalcogenide quantum dots by balancing precursor reactivity. *ACS Nano* 2010, 5, 183-190.

149. Samadpour, M.; Boix, P. P.; Giménez, S.; Iraji Zad, A.; Taghavinia, N.; Mora-Seró, I.; Bisquert, J., Fluorine treatment of TiO_2 for enhancing quantum dot sensitized solar cell performance. *J. Phys. Chem. C* 2011, 115, 14400-14407.

150. Hu, X.; Zhang, Q.; Huang, X.; Li, D.; Luo, Y.; Meng, Q., Aqueous colloidal $CuInS_2$ for quantum dot sensitized solar cells. *J. Mater. Chem.* 2011, 21, 15903-15905.

151. Regulacio, M. D.; Han, M.-Y., Composition-tunable alloyed semiconductor nanocrystals. *Accounts Chem. Res.* 2010, 43, 621-630.

152. Abdelhamid, O.; Nadia, O., Chemically deposited heterojunction solar cells $Pb_{1-x}Cd_xS$(n)/Si(p). *Int. J. Nanosci.* 2010, 9, 599-604.

153. Markov, V. F.; Maskaeva, L. N.; Kitaev, G. A., Predicting the composition of $Cd_xPb_{1-x}S$ films deposited from aqueous solutions. *Inorg. Mater.* 2000, 36, 1194-1196.

154. Maskaeva, L. N.; Markov, V. F.; Gusev, A. I., Temperature range of decomposition and degradation of $Cd_xPb_{1-x}S$ supersaturated solid solutions. *Dokl. Phys. Chem.* 2003, 390, 147-151.

155. Rabinovich, E.; Wachtel, E.; Hodes, G., Chemical bath deposition of single-phase (Pb,Cd)S solid solutions. *Thin Solid Films* 2008, 517, 737-744.

156. Chan, W.-L.; Ligges, M.; Jailaubekov, A.; Kaake, L.; Miaja-Avila, L.; Zhu, X.-Y., Observing the multiexciton state in singlet fission and ensuing ultrafast multielectron transfer. *Science* 2011, 334, 1541-1545.

157. Nozik, A. J.; Beard, M. C.; Luther, J. M.; Law, M.; Ellingson, R. J.; Johnson, J. C., Semiconductor quantum dots and quantum dot arrays and applications of multiple exciton generation to third-generation photovoltaic solar cells. *Chem. Rev.* 2010, 110, 6873-6890.

158. Neo, M. S.; Venkatram, N.; Li, G. S.; Chin, W. S.; Ji, W., Synthesis of PbS/CdS core−shell QDs and their nonlinear optical properties. *J. Phys. Chem. C* 2010, 114, 18037-18044.

159. Thangavel, S.; Ganesan, S.; Chandramohan, S.; Sudhagar, P.; Kang, Y. S.; Hong, C. H., Band gap engineering in PbS nanostructured thin films from near-infrared down to visible range by in situ Cd-doping. *J. Alloy. Compd.* 2010, 495, 234-237.

160. Pentia, E.; Draghici, V.; Sarau, G.; Mereu, B.; Pintilie, L.; Sava, F.; Popescu, M., Structural, electrical, and photoelectrical properties of $Cd_xPb_{1-x}S$ thin films prepared by chemical bath deposition. *J. Electrochem. Soc.* 2004, 151, G729-G733.

161. Rühle, S.; Shalom, M.; Zaban, A., Quantum-dot-sensitized solar cells. *ChemPhysChem* 2010, 11, 2290-2304.

162. Dattoli, E. N.; Wan, Q.; Guo, W.; Chen, Y.; Pan, X.; Lu, W., Fully transparent thin-film transistor devices based on SnO_2 nanowires. *Nano Lett.* 2007, 7, 2463-2469.

163. Wang, Y.; Lee, J. Y.; Zeng, H. C., Polycrystalline SnO_2 nanotubes prepared via infiltration casting of nanocrystallites and their electrochemical application. *Chem. Mater.* 2005, 17, 3899-3903.

164. Dai, Z. R.; Gole, J. L.; Stout, J. D.; Wang, Z. L., Tin oxide nanowires, nanoribbons, and nanotubes. *J. Phys. Chem. B* 2002, 106, 1274-1279.

165. Acciarri, M., Nanocrystalline SnO_2 based thin films obtained by sol-gel route: A morphological and structural investigation. *Chem. Mater.* 2003, 15, 2646-2650.

166. Zhang, G.; Liu, M., Preparation of nanostructured tin oxide using a sol-gel process based on tin tetrachloride and ethylene glycol. *J. Mater. Sci.* 1999, 34, 3213-3219.

167. Qin, D.; Yan, P.; Li, G.; Xing, J.; An, Y., Self-construction of SnO_2 cubes based on aggration of nanorods. *Mater. Lett.* 2008, 62, 2411-2414.

168. Yang, H. G.; Zeng, H. C., Self-construction of hollow SnO_2 octahedra based on two-dimensional aggregation of nanocrystallites. *Angew. Chem. Int. Ed.* 2004, 43, 5930-5933.

169. Chen, H. T.; Wu, X. L.; Zhang, Y. Y.; Zhu, J.; Cheng, Y. C.; Chu, P. K., A novel hydrothermal route to synthesize solid SnO_2 nanospheres and their photoluminescence property. *Appl. Phys. A-Mater.* 2009, 1-5.

170. Das, S.; Chaudhui, S.; Maji, S., Ethanol-water mediated solvothermal synthesis of cube and pyramid shaped nanostructured tin oxide. *J. Phys. Chem. C* 2008, 112, 6213-6219.

171. Ayouchi, R.; Martin, F.; Ramos Barrado, J. R.; Martos, M.; Morales, J.; Sánchez, L., Use of amorphous tin-oxide films obtained by spray pyrolysis as electrodes in lithium batteries. *J. Power Sources* 2000, 87, 106-111.

172. Zhang, K.; Zhu, F.; Huan, C. H. A.; Wee, A. T. S., Indium tin oxide films prepared by radio frequency magnetron sputtering method at a low processing temperature. *Thin Solid Films* 2000, 376, 255-263.

173. Chen, Z.; Pan, D.; Zhao, B.; Ding, G.; Jiao, Z.; Wu, M.; Shek, C. H.; Wu, L. C. M.; Lai, J. K. L., Insight on fractal assessment strategies for tin dioxide thin films. *ACS Nano* 2010, 4, 1202-1208.

174. Kim, H. W.; Shim, S. H.; Lee, C., SnO_2 microparticles by thermal evaporation and their properties. *Ceram. Int.* 2006, 32, 943-946.

175. Chen, W.; Ghosh, D.; Chen, S., Large-scale electrochemical synthesis of SnO_2 nanoparticles. *J. Mater. Sci.* 2008, 43, 5291-5299.

176. Gubbala, S.; Russell, H. B.; Shah, H.; Deb, B.; Jasinski, J.; Rypkema, H.; Sunkara, M. K., Surface properties of SnO_2 nanowires for enhanced performance with dye-sensitized solar cells. *Energy Environ. Sci.* 2009, 2, 1302-1309.

177. Jia, Y.; He, L.; Guo, Z.; Chen, X.; Meng, F.; Luo, T.; Li, M.; Liu, J., Preparation of porous tin oxide nanotubes using carbon nanotubes as templates and their gas-sensing properties. *J. Phys. Chem. C* 2009, 113, 9581-9587.

178. Chen, W.; Wu, J. S.; Xia, X. H., Porous anodic alumina with continuously manipulated pore/cell size. *ACS Nano* 2008, 2, 959-965.

179. Wang, Q.; Zhu, K.; Neale, N. R.; Frank, A. J., Constructing ordered sensitized heterojunctions: Bottom-up electrochemical synthesis of p-type semiconductors in oriented n-TiO_2 nanotube arrays. *Nano Lett.* 2009, 9, 806-813.

180. Zhu, K.; Vinzant, T. B.; Neale, N. R.; Frank, A. J., Removing structural disorder from oriented TiO_2 nanotube arrays: Reducing the dimensionality of transport and recombination in dye-sensitized solar cells. *Nano Lett.* 2007, 7, 3739-3746.

181. Jennings, J. R.; Ghicov, A.; Peter, L. M.; Schmuki, P.; Walker, A. B., Dye-sensitized solar cells based on oriented TiO_2 nanotube arrays: transport, trapping, and transfer of electrons. *J. Am. Chem. Soc.* 2008, 130, 13364-13372.

182. Mor, G. K.; Varghese, O. K.; Paulose, M.; Shankar, K.; Grimes, C. A., A review on highly ordered, vertically oriented TiO_2 nanotube arrays: Fabrication, material properties, and solar energy applications. *Sol. Energ. Mat. Sol. C* 2006, 90, 2011-2075.

183. Wei, W.; Lee, K.; Shaw, S.; Schmuki, P., Anodic formation of high aspect ratio, self-ordered Nb_2O_5 nanotubes. *Chem. Commun.* 2012, 48, 4244-4246.

184. Shin, H. C.; Dong, J.; Liu, M., Porous tin oxides prepared using an anodic oxidation process. *Adv. Mater.* 2004, 16, 237-240.

185. Privman, V.; Goia, D. V.; Park, J.; Matijević, E., Mechanism of formation of monodispersed colloids by aggregation of nanosize precursors. *J. Colloid Interf. Sci.* 1999, 213, 36-45.

186. Norris, S. A.; Watson, S. J., Geometric simulation and surface statistics of coarsening faceted surfaces. *Acta Mater.* 2007, 55, 6444-6452.

187. Joo, J.; Kwon, S. G.; Yu, J. H.; Hyeon, T., Synthesis of ZnO nanocrystals with cone, hexagonal cone, and rod shapes via non-hydrolytic ester elimination sol–gel reactions. *Adv. Mater.* 2005, 17, 1873-1877.

188. Ghezelbash, A.; Sigman, M. B.; Korgel, B. A., Solventless synthesis of nickel sulfide nanorods and triangular nanoprisms. *Nano Lett.* 2004, 4, 537-542.

189. Ghicov, A.; Schmuki, P., Self-ordering electrochemistry: a review on growth and functionality of TiO_2 nanotubes and other self-aligned MO_x structures. *Chem. Commun.* 2009, 2791-2808.

190. Zeng, H. C., Ostwald ripening: A synthetic approach for hollow nanomaterials. *Curr. Nanosci.* 2007, 3, 177-181.

191. Leite, E. R.; Giraldi, T. R.; Pontes, F. M.; Longo, E.; Beltran, A.; Andres, J., Crystal growth in colloidal tin oxide nanocrystals induced by coalescence at room temperature. *Appl. Phys. Lett.* 2003, 83, 1566-1568.

192. Zhuang, Z.; Zhang, J.; Huang, F.; Wang, Y.; Lin, Z., Pure multistep oriented attachment growth kinetics of surfactant-free SnO_2 nanocrystals. *Phys. Chem. Chem. Phys.* 2009, 11, 8516-8521.

193. Yin, Y.; Rioux, R. M.; Erdonmez, C. K.; Hughes, S.; Somorjai, G. A.; Alivisatos, A. P., Formation of hollow nanocrystals through the nanoscale Kirkendall effect. *Science* 2004, 304, 711-714.

194. Liu, R.; Yang, S.; Wang, F.; Lu, X.; Yang, Z.; Ding, B., Sodium chloride template synthesis of cubic tin dioxide hollow particles for lithium ion battery applications. *Appl. Mater. Interfaces* 2012, 4, 1537-1542.

195. Herring, C., Some theorems on the free energies of crystal surfaces. *Phys. Rev.* 1951, 82, 87-93.

196. Rottman, C.; Wortis, M., Exact equilibrium crystal shapes at nonzero temperature in two dimensions. *Phys. Rev. B* 1981, 24, 6274-6277.

197. Seyed-Razavi, A.; Snook, I. K.; Barnard, A. S., Origin of nanomorphology: Does a complete theory of nanoparticle evolution exist? *J. Mater. Chem.* 2010, 20, 416-421.

198. Zhang, H.; Liu, Y.; Wang, C.; Zhang, J.; Sun, H.; Li, M.; Yang, B., Directing the growth of semiconductor nanocrystals in aqueous solution: Role of electrostatics. *ChemPhysChem* 2008, 9, 1309-1316.

199. Zeng, H. C., Synthetic architecture of interior space for inorganic nanostructures. *J. Mater. Chem.* 2006, 16, 649-662.

200. DeHoff, R. T., Thermodynamics in materials science. ISBN 0-07-112596-5, McGRAW-Hill International: 1993.

201. Thermodynamics of solid surfaces - crystal/particle shape, *http://www.mnp.leeds.ac.uk/sdevans/lectures/Lecture%203.pdf*.

202. Ribeiro, C.; Lee, E. J. H.; Giraldi, T. R.; Longo, E.; Varela, J. A.; Leite, E. R., Study of synthesis variables in the nanocrystal growth behavior of tin oxide processed by controlled hydrolysis. *J. Phys. Chem. B* 2004, 108, 15612-15617.

203. Penn, R. L.; Banfield, J. F., Imperfect oriented attachment: Dislocation generation in defect-free nanocrystals. *Science* 1998, 281, 969-971.

204. Beenakker, C. W. J.; Ross, J., Theory of Ostwald ripening for open systems. *J. Chem. Phys.* 1985, 83, 4710-4714.

205. Yang, H. G.; Zeng, H. C., Preparation of hollow anatase TiO_2 nanospheres via Ostwald ripening. *J. Phys. Chem. B* 2004, 108, 3492-3495.

206. Chen, J. S.; Li, C. M.; Zhou, W. W.; Yan, Q. Y.; Archer, L. A.; Lou, X. W., One-pot formation of SnO_2 hollow nanospheres and a-Fe_2O_3@SnO_2 nanorattles with large void space and their lithium storage properties. *Nanoscale* 2009, 1, 280-285.

207. Wang, Y.; Chen, T., Nonaqueous and template-free synthesis of Sb doped SnO_2 microspheres and their application to lithium-ion battery anode. *Electrochim. Acta* 2009, 54, 3510-3515.

208. Shuttleworth, D., Preparation of metal-polymer dispersions by plasma techniques. An ESCA investigation. *J. Phys. Chem.* 1980, 84, 1629-1634.

209. Ansell, R. O.; Dickinson, T.; Povey, A. F.; Sherwood, P. M. A., Quantitative use of the angular variation technique in studies of tin by X-ray photoelectron spectroscopy. *J. Electron Spectrosc. Relat. Phenom.* 1977, 11, 301-313.

210. Stefanov, P.; Atanasova, G.; Manolov, E.; Raicheva, Z.; Lazarova, V., Preparation and characterization of SnO_2 films for sensing applications. *J. Phys. Conf. Series* 2008, 100, 082046.

211. Nagasawa, Y.; Choso, T.; Karasuda, T.; Shimomura, S.; Ouyang, F.; Tabata, K.; Yamaguchi, Y., en. *Surf. Sci.* 1999, 433, 226-229.

212. Li, M.; Lu, Q.; Nuli, Y.; Qian, X., Core-shell and hollow microspheres composed of tin oxide nanocrystals as anode materials for lithium-ion batteries. *Electrochem. Solid ST.* 2007, 10, K33-K37.

213. Banerjee, A. N.; Kundoo, S.; Saha, P.; Chattopadhyay, K. K., Synthesis and characterization of nano-crystalline fluorine-doped tin oxide thin films by Sol-Gel method. *J. Sol-Gel Sci. Techn.* 2003, 28, 105-110.

214. Velásquez, C.; Rojas, F.; Ojeda, M. L.; Ortiz, A.; Campero, A., Structure and texture of self-assembled nanoporous SnO_2. *Nanotechnology* 2005, 16, 1278-1284.

215. Gu, Z.; Liang, P.; Liu, X.; Zhang, W.; Le, Y., Characteristics of sol-gel SnO_2 films treated by ammonia. *J. Sol-Gel Sci. Techn.* 2000, 18, 159-166.

216. Domashevskaya, E. P.; Chuvenkova, O. A.; Kashkarov, V. M.; Kushev, S. B.; Ryabtsev, S. V.; Turishchev, S. Y.; Yurakov, Y. A., TEM and XANES investigations and optical properties of SnO nanolayers. *Surf. Interface Analysis* 2006, 38, 514-517.

217. Flaisher, H.; Tenne, R.; Hodes, G., Improved performance of cadmium chalcogenide photoelectrochemical cells: surface modification using copper sulphide. *J. Phys. D: Appl. Phys.* 1984, 17, 1055.